**The Dissertation Committee for Aaron Patrick Moon Certifies that this is the approved version of the following Dissertation:**

# Studying the Density of States of Buried Interfaces in Organic Semiconductor Thin Films Using Electronic Sum Frequency Generation

**Committee:**

Sean T. Roberts, Supervisor

Carlos R. Baiz

David A. Vanden Bout

Michael Rose

Xiaoqin Li

# Studying the Density of States of Buried Interfaces in Organic Semiconductor Thin Films Using Electronic Sum Frequency Generation

**by**

**Aaron Patrick Moon**

**Dissertation**

Presented to the Faculty of the Graduate School of

The University of Texas at Austin

in Partial Fulfillment

of the Requirements

for the Degree of

**Doctor of Philosophy**

**The University of Texas at Austin**

**May 2019**

# Dedication

For Jamie, without whom none of this would be possible.

# Acknowledgements

First, I would like to thank my wife Jamie for all her help in this long process. Graduate school has been difficult, and I appreciate the unending love and support she has given me through-out. Next, I thank my family for their help and support. My father, who instilled in me a love of science from himself, my mother for her encouragement in any of my pursuits academic or otherwise, my step-father for our many discussions of science (among other things) over early morning coffee, and my sisters, both for their help raising me when I was young and their support during graduate school (mostly listening to me vent about the latest scientific hiccup).

I had the privilege of a wonderful PI in grad school with Sean, and his patience as I learned the intricacies of the SFG set-up as well as the time it took to improve (usually months instead of the expected week) is a large portion of how I finished the work below, and likely wouldn't have with anyone else guiding me. I also appreciate the two graduate students that began this group with me, Mike Azzaro and Aaron Le, for the many, many hours we spent in the laser lab, struggling to get the beam to do what we wanted. Dr. Ravindra Pandey was a huge help in getting the ESFG project off the ground and running, from the first time we saw ESFG signal to the first HD-ESFG roughly a year later. I thank Jon Bender for his help learning about film creation and characterization, as well as the insane amount of work that went into making the films for these experiments that he did. I should also acknowledge Danny Cotton as my successor on the SFG project and the help he gave me in its final parts. I look forward to the fantastic work he will be doing with Jon on the spectrometer I started, likely far surpassing anything I would have ever found possible. I also appreciate the many movie nights with Michelle Blemker, who gave me

something to look forward to across many weeks (what nerd doesn't love the ability to share classic 80's movies with friends) and Emily Raulerson for chatting and commiserating when the laser refused to work.

Aaron and Rachel Lammer have been wonderful friends and a support system throughout graduate school, putting up with living with Jamie and I for three years, a feat that was often not easy I can imagine. For that, your friendship, and your support, I am eternally grateful. I thank Michelle Dose for our time together both at Georgia Tech and UT, from the many dinners and boardgame nights to helping us find a place to live when we first moved to Texas. Jamie and I love that we were able to live close together as we moved completely independently and hope that we might again in the future. I had many friends that kept my sanity in check throughout grad school (more than can be named, as it was a lot of work), but a few include Dakota Lindsey, Jessica Banerjee, Michael Rice, and Zuzana Kocsis who were always willing to talk and listen even from states away.

# Abstract

## Studying the Density of States of Buried Interfaces in Organic Semiconductor Thin Films Using Electronic Sum Frequency Generation

Aaron Patrick Moon, PhD

The University of Texas at Austin, 2019

Supervisor: Sean T. Roberts

Abstract: New nanostructured semiconductor materials such as nanocrystals and organic semiconductors constitute an attractive platform for optoelectronics design due to the ease of their processability and highly tunable properties. Incorporating these new nanostructured materials into electrical circuits requires forming junctions between them and other layers in a device, yet the change in dielectric properties about these junctions can strongly perturb the electronic structure of the two layers. Specifically, the morphology of the interface between two materials greatly affect their ability to transfer charge and energy through the system, and the method through which this energy travels across a junction is poorly understood. To study these processes, an interfacial technique is required that measures the Density of States (Dos) at buried interfaces in working devices. In this thesis, we adapt an interface-selective optical technique, electronic sum frequency generation (ESFG), to study the dynamics of energy transfer across interfaces in these materials. We begin by developing "direct" detected ESFG to study the electronic states and morphology at the interface of thin films made from known organic semiconductor materials. Using direct ESFG, we examine the differences in the DoS at an interface in an

organic thin film relative to its bulk. Through polarization optics, we study morphological changes in the film caused at the junction of the OSC and substrate. To account for interference from multiple ESFG active interfaces present in a thin film, we use a modeling system to separate contributions to the measured ESFG signal from the air exposed and buried interface of interest. We then adapt the direct detected ESFG to "heterodyne" detected ESFG (HD-ESFG), which significantly increases the detection ability of the ESFG spectrometer. Additionally, HD-ESFG allows us to measure the phase of the materials response, which direct ESFG cannot. This phase information can give a better understanding of the morphology at the interface and additional inputs for thin film interference modeling to better deconvolute the signal from the buried interface.

# Table of Contents

# List of Figures

# Chapter 1: Introduction

## 1.1: The growth of new photovoltaic technology

Single crystal inorganic semiconductors (ISCs) are ubiquitous as the base for technology. Their high Earth abundance coupled with excellent device performance across a broad range of applications through careful control of production give ISCs the ability to provide for many technological needs. However, despite their wide range of application, new systems are needed to provide for advancement within the device market. Recently, nanostructured materials are being developed to either improve, surpass, or fill niche rolls in the device market relative to these ISC systems[1–7]. Nanocrystal technology, especially semi-conductor nanocrystals called quantum dots (QDs), allow for careful control of the absorption and fluorescence of a device by precise modification of nanocrystal size.[5] This shows promise for the display market with quantum dot TV's already being sold and potential use in the development of new detectors. Meanwhile, organic semiconductors (OSCs) are being developed for use as flexible electronics.[8,9] OSCs are also competing with quantum dots for the next display technology, having already been implemented in phones and TV's on the market.[10] Organics are also being considered as a method for improvement of silicon solar cells through processes such as photon up- and down-conversion.[11–13] These processes would increase silicon's efficiency in both the red and blue parts of the solar spectrum in a cheap and easily processible way. Dual quantum dot, OSC systems are additionally being studied to improve quantum dots' functionality.[7,14]

With the possible capabilities of the materials described above, you might expect them to be more fully developed and prevalent within the market, yet these are still an emerging technology. One of the major factors limiting widespread use of these devices is small, yet critical: energetic transfer across the junctions within these systems is poorly

understood, despite the intrinsic interfacial nature of nanostructured materials.[15–20] It is necessary to have a solid understanding of charge and energy transfer across many interfaces at many length scales, between multiple materials for the creation of high-performance devices. For example, quantum dots are inherently separated individual units trying to move excitations or charge across the relatively large gaps between dots. Organic dyes used to improve silicon solar cells must transfer energy into silicon, but this motion of carriers across that junction is poorly understood.[11,21,22] This lack of understanding limits the use of these new, inherently interfacial systems and must be solved to fully incorporate them into new, exciting technologies.

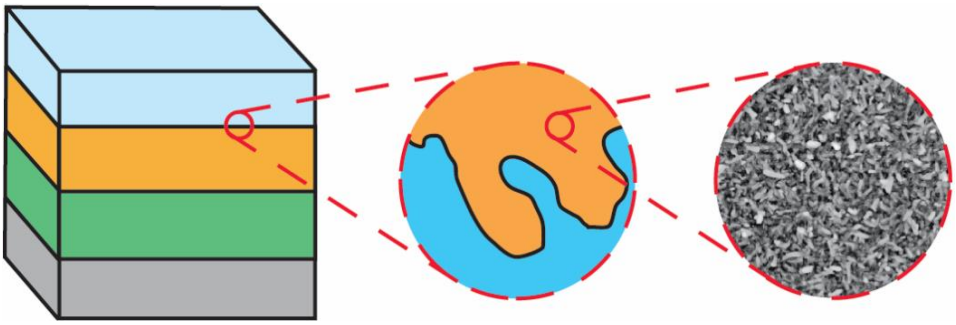

**Figure 1-1**: Cartoon of the interfacial length scales for organic thin films

There is a critically important yet poorly understood influence on the function of developing nanostructured technologies described above: the movement of charge and energy at an interface. In traditional ISCs, the generated exciton is a loosely bound Wannier-Mott exciton (with binding energies between the separated electron and hole of only a few tens of meV) that quickly separates and passes charge between layers for extraction. This picture is overly simplistic, or even wrong, when describing OSC or nanocrystal technology. Unlike their single crystal counterparts, inorganic nanocrystals are separated into individual units that must move any generated charge or excitons across tens of nanometers gaps due to the oily carbon alkyl chains used to stop growth in their

creation.[23] This picture only gets more complicated as we move to the discussion of larger crystal units of correlated particles that interface with each other, and further still when polycrystalline films must meet other similar films or single crystal ISC systems. For the mostly molecular OSC perspective, we lose the large separation gaps that plague transport in nanocrystal systems and instead must now transfer our excitations either between organic films or into an ISC to generate free carriers. The need for exciton transfer accompanies a much higher binding energy for the excitons (approximately 1 eV) in OSC films.[9,24,25] The excited carriers for OSC systems are Frenkel excitons which, due to their high binding energies in a low dielectric environment, will often undergo charge recombination across an interface instead of charge separation.[9,26,27] Both of these systems must also deal with the complication of moving energy within highly structured polycrystalline films.[28–30] At this greater length scale, the morphology between crystals within different films now controls how energy moves between two different materials. The picture that emerges from this description is inherently one where systems have a large number of interfaces—not just between individual layers but within many parts of the system and at many different length scales (Figure 1-1). Given the inherently interfacial nature of devices made with these materials, it comes as no surprise then that understanding how charge and energy moves across these junctions is incredibly important to understanding how these devices function. Unfortunately, the physical picture for how energy moves across these boundaries remains poorly understood. For the purposes of this dissertation, we will focus on the discussion of OSC materials.

### 1.2: A need for a new spectroscopy

Let's begin by thinking about molecular films as a whole and the differences we need to consider from those of individual molecules. When a molecule is taken from

solution (where molecules tend to act as monomers except at high concentration), the energetic landscape can shift drastically. The electronic transitions of the monomer go from lone dipoles to a system with a large amount of molecular interactions in the form of coupling between molecule's electronic states.[31,32] The individual molecular states are further perturbed by possible distortions to their molecular shape, no longer being free floating and capable of rotation, instead being forced to one orientation. These effects taken together greatly change what is measured if an electronic absorption spectrum is taken of the system. The sharp, individual peaks seen in solution are replaced with broad peaks that have multiple contributions from both the shifts caused to individual molecule's accessible states and the appearance of peaks from coupled transitions. These couplings are highly sensitive to molecular orientation and can lead to shifts in the location of absorption to higher or lower energies (and sometimes both) via H- and J- aggregation, and these can be convoluted with other effects such as the appearance of charge transfer states within the molecular system.[30–33] In addition, we begin to see peaks that aren't just from molecular interactions but also due to sets of molecules influencing one another such as non-equivalent sites within unit cells like Davydov splitting.[34,35] Thus, by moving from solution to a thin film, the picture becomes much more complicated, and this is before the addition of the many molecular layers needed for an OSC device (Figure 1-2).

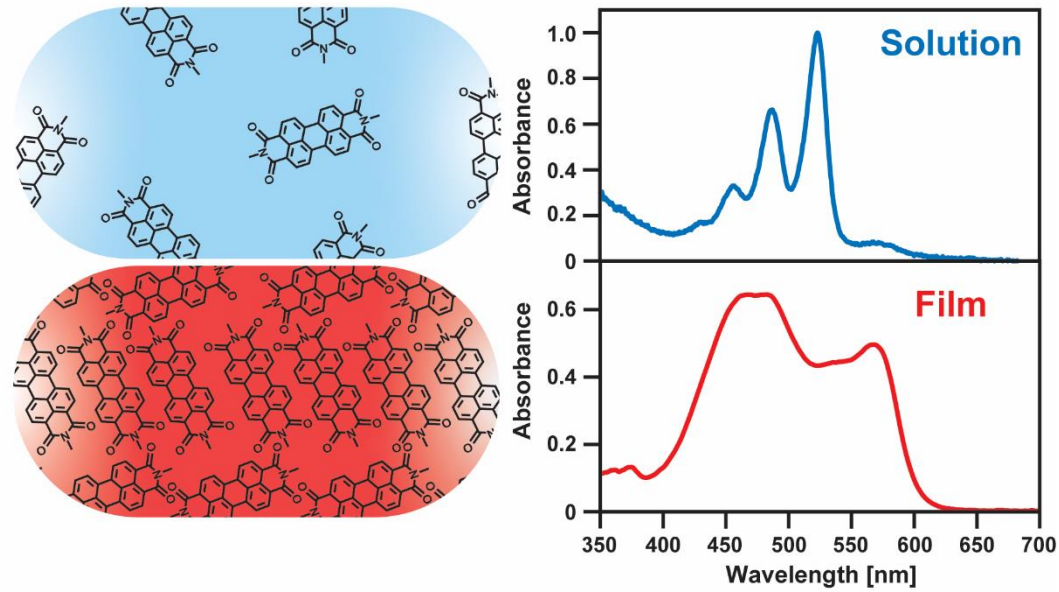


**Figure 1-2**: Cartoon of solution and solid-state molecular organization with representative absorption spectra for both using methyl substituted perylenediimide

Moving from the bulk to the interface leads to a similar increase in complexity. Not only are the previous interactions still present, but the system is perturbed further by a breakage in the symmetry that exists in the bulk.[28,36,37] Bringing together two disparate systems, each with their own complicated morphology and energetic states, leads to drastic changes for both at the interface. Interaction with each other at their junction leads to changes in the morphology of both species, and in turn the energetic Density of States (DoS) available for excitations at this interface. That said, these effects can be separated, studied, and understood (to a more or lesser degree depending on how complicated an individual system is) when described for a bulk system, and we can follow and understand energy movement and transitions within a film, so in principle this should be possible for an interface. This is because while these processes are complicated, we have tools well suited to their study in the bulk, but lack this ability for interfaces.

If we want to understand the new energetic transitions present within a bulk film from those of a monomer, the first and easiest experiments to perform are usually electronic absorption and emission spectroscopy. While these experiments perform their job excellently, they have a limitation for the study of interfacial states as they measure these properties for the whole film. The interfacial molecules that dominate the movement of charge within a system are typically within a few monolayers of the junction. This means that for a real, optically thick organic thin film of 50 - 100 nm, the signal from the very few interfacial molecules are overshadowed by that from the bulk of the film. If the morphology of the film is important, we might instead think to use x-ray diffraction (XRD) or atomic force microscopy (AFM). Both of these experiments report on the morphology of systems, however they aren't well suited for the study of buried interfaces. XRD is a bulk technique and therefore suffers the same limitations as absorption and emission spectroscopies. Conversely, though AFM is interface specific, it's important to note that it is only sensitive to the outermost interface within a system. The charge and energy transfer that controls device performance occurs at junctions buried beneath the layers that form the device.[7,24,38,39] This leaves only two options to study the buried junctions: make a device and rip it apart to study the interface we made (hoping we don't change the system in the process) or make the devices thin enough that we can see the desired interface while still only hoping the system is representative of the working device. Instead of AFM, which requires deliberately non-functioning devices, we need one that can study a device *in situ* to truly understand the transfer processes that dominate the function of a device. Additionally, if we can study the morphology and DoS for the interface simultaneously, the number of measurements we would need to do would not only be reduced, but we could also correlate the effect morphology has on the energetics of transfer. To achieve this goal,

we will use electronic sum frequency generation (ESFG) to probe both the DoS of a buried interface and simultaneously gain information about its morphology.[36,40–43]

### 1.3: Electronic sum frequency generation

Electronic absorption is a fantastic way to measure the electronic transitions available to a system of interest, especially for molecular solid-state systems, where the peak location and structure of the measured absorption are indicative of system morphology. However, absorption spectroscopy measures the energetic states of the entire film, hiding the interfacial signal we wish to measure under that of the much stronger signal from the bulk. By using electronic sum frequency generation (ESFG), the sensitivity to the intermingling of both morphology and energetics can be maintained but specified to the measurement of the interface.[41,44–47] As in an absorption measurement, an ESFG experiment begins by first generating a spectrally broad white light (WL) beam. This beam, which stretches from ~ 450 to 750 nm across the visible region, will serve as a resonant probe of the DoS in the same way that it does in a absorption experiment, with the exception that instead of directly measuring its attenuation as it passes through the material, we will simultaneously bring in a second beam (called the upconversion beam) that overlaps spatially and temporally with the WL field. The upconversion field is not electronically resonant with the film and is therefore not attenuated by it. Instead, it acts to scatter the resonant coherences created by the WL off of higher virtual states, similar to a Raman experiment.[48] The photons produced by this process have energy equal to the sum of our two input beams and constitute the ESFG signal measured. As such, by measuring the generated ESFG field with a known frequency for the upconversion field, we can back-calculate the resonant energies within the WL beam that lead to the generation of the ESFG signal (Figure 1-3).

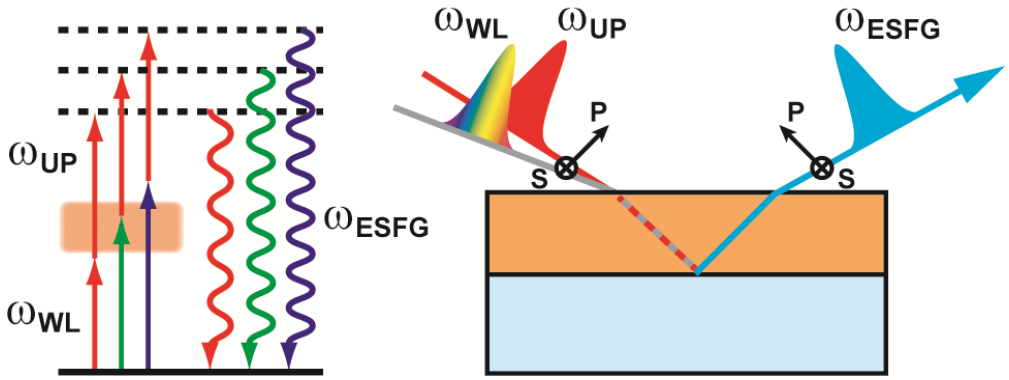


**Figure 1-3**: Simple cartoon of ESFG. $\omega_{WL}$, $\omega_{UP}$, and $\omega_{ESFG}$ represent the white light, upconversion, and ESFG fields respectively. P and S show polarization control of fields.

The obvious question is one of complexity: why move from a one beam electronic absorption experiment to a more complicated system in which we use two beams to generate a third? Thanks to the use of two fields for signal generation instead of one, we measure a non-linear, second-order interaction instead of a linear, first-order one. Due to the symmetry of this new generation scheme, no signal is generated within the bulk if it is centrosymmetric. However, at an interface between two materials, this symmetry is necessarily broken, and as such the interface is ESFG-active.[44,45] In this way, we have created an experiment that is effectively an interface specific absorption measurement, exactly as we needed. In addition to our new interfacial electronic absorption, we can independently control the polarization of our three fields. By comparing different polarization combinations, we can now map the measured signal onto the orientation of the molecular transition dipoles within our sample film and gain even greater insight into the morphology at the buried interfaces we wish to study.[41,49,50] ESFG is also a purely optical technique and can therefore probe any interface of a centrosymmetric medium that is accessible by light, including functioning photovoltaic devices *in situ*.

### 1.4: Thesis Outline

This thesis will serve as a description and vetting of ESFG and will show its development for use within thin film systems of interest to the OSC community. In Chapter 2, I will begin with a brief description of the theory that drives generation of ESFG signals and the assumptions made when measuring ESFG that are typical within the field. Chapter 3 will be a discussion of a complication that lurks within ESFG on thin films in the form of interference between multiple ESFG signals generated within a sample. This chapter will also include the description of a transfer matrix model that I use to separate the contributions of these two signals to the total measured field. Chapter 4 will detail the experimental layout used for the ESFG spectrometer that I built. Chapter 5 will feature ESFG data measured from a thin film of copper phthalocyanine on glass substrates, which served as the initial vetting system for the ESFG spectrometer. In Chapter 6 we shift to ESFG measurement of three selected perylenediimides (from the rylene class of dye molecules) deposited on fused quartz substrates. Perylenediimide films are studied within other projects of our group for their potential use as singlet fission sensitizers for photocurrent generation, and these experiments serve as the first step to a study of these molecules on silicon. Finally, Chapter 7 will show the further development of the ESFG spectrometer by changing from directly detecting the generated signal to a heterodyne detection scheme. This serves to improve the signal-to-noise ratio of the experiment while also giving additional insight into the measured ESFG spectra.

## 1.5: Chapter References


(1) Gabriel, M. M.; Kirschbrown, J. R.; Christesen, J. D.; Pinion, C. W.; Zigler, D. F.; Grumstrup, E. M.; Mehl, B. P.; Cating, E. E. M.; Cahoon, J. F.; Papanikolas, J. M. Direct Imaging of Free Carrier and Trap Carrier Motion in Silicon Nanowires by Spatially-Separated Femtosecond Pump–Probe Microscopy. *Nano Letters* **2013**, *13* (3), 1336–1340.

(2) Abbas, M. A.; Basit, M. A.; Yoon, S. J.; Lee, G. J.; Lee, M. D.; Park, T. J.; Kamat, P. V.; Bang, J. H. Revival of Solar Paint Concept: Air-Processable Solar Paints for the Fabrication of Quantum Dot-Sensitized Solar Cells. *The Journal of Physical Chemistry C* **2017**, *121* (33), 17658–17670.

(3) Alharbi, F. H.; Kais, S. Theoretical Limits of Photovoltaics Efficiency and Possible Improvements by Intuitive Approaches Learned from Photosynthesis and Quantum Coherence. *Renewable and Sustainable Energy Reviews* **2015**, *43*, 1073–1089.

(4) Briseno, A. L.; Mannsfeld, S. C. B.; Reese, C.; Hancock, J. M.; Xiong, Y.; Jenekhe, S. A.; Bao, Z.; Xia, Y. Perylenediimide Nanowires and Their Use in Fabricating Field-Effect Transistors and Complementary Inverters. *Nano Letters* **2007**, *7* (9), 2847–2853.

(5) Chistyakov, A. A.; Zvaigzne, M. A.; Nikitenko, V. R.; Tameev, A. R.; Martynov, I. L.; Prezhdo, O. V. Optoelectronic Properties of Semiconductor Quantum Dot Solids for Photovoltaic Applications. *The Journal of Physical Chemistry Letters* **2017**, *8* (17), 4129–4139.

(6) Song, L.; Guo, X.; Hu, Y.; Lv, Y.; Lin, J.; Liu, Z.; Fan, Y.; Liu, X. Efficient Inorganic Perovskite Light-Emitting Diodes with Polyethylene Glycol Passivated Ultrathin $CsPbBr_3$ Films. *The Journal of Physical Chemistry Letters* **2017**, *8* (17), 4148–4154.

(7) Schlesinger, R.; Bianchi, F.; Blumstengel, S.; Christodoulou, C.; Ovsyannikov, R.; Kobin, B.; Moudgil, K.; Barlow, S.; Hecht, S.; Marder, S. R.; et al. Efficient Light Emission from Inorganic and Organic Semiconductor Hybrid Structures by Energy-Level Tuning. *Nature Communications* **2015**, *6*, 6754.

(8) Sirringhaus, H. 25th Anniversary Article: Organic Field-Effect Transistors: The Path Beyond Amorphous Silicon. *Advanced Materials* **2014**, *26* (9), 1319–1335.

(9) Hedley, G. J.; Ruseckas, A.; Samuel, I. D. W. Light Harvesting for Organic Photovoltaics. *Chemical Reviews* **2017**, *117* (2), 796–837.

(10) Guo, F.; Karl, A.; Xue, Q.-F.; Tam, K. C.; Forberich, K.; Brabec, C. J. The Fabrication of Color-Tunable Organic Light-Emitting Diode Displays via Solution Processing. *Light: Science & Applications* **2017**, *6* (11), e17094.

(11) Futscher, M. H.; Rao, A.; Ehrler, B. The Potential of Singlet Fission Photon Multipliers as an Alternative to Silicon-Based Tandem Solar Cells. *ACS Energy Letters* **2018**, *3* (10), 2587–2592.

(12) Tabernig, S. W.; Daiber, B.; Wang, T.; Ehrler, B. Enhancing Silicon Solar Cells with Singlet Fission: The Case for Förster Resonant Energy Transfer Using a Quantum Dot Intermediate. *Journal of Photonics for Energy* **2018**, *8* (02), 1.

(13) Schwerin, A. F.; Johnson, J. C.; Smith, M. B.; Sreearunothai, P.; Popović, D.; Černý, J.; Havlas, Z.; Paci, I.; Akdag, A.; MacLeod, M. K.; et al. Toward Designed Singlet Fission: Electronic States and Photophysics of 1,3-Diphenylisobenzofuran †. *The Journal of Physical Chemistry A* **2010**, *114* (3), 1457–1473.

(14) Agranovich, V. M.; Gartstein, Y. N.; Litinskaya, M. Hybrid Resonant Organic–Inorganic Nanostructures for Optoelectronic Applications. *Chemical Reviews* **2011**, *111* (9), 5179–5214.

(15) Kymakis, E. Interfacial Engineering of Perovskite Solar Cells for Improved Performance and Stability. *Advanced Materials Interfaces* **2018**, *5* (22), 1801595.

(16) Rajagopal, A.; Yao, K.; Jen, A. K.-Y. Toward Perovskite Solar Cell Commercialization: A Perspective and Research Roadmap Based on Interfacial Engineering. *Advanced Materials* **2018**, *30* (32), 1800455.

(17) Wang, Y.; Duan, J.; Duan, Y.; Zhao, Y.; Pang, Z.; He, B.; Tang, Q. Interfacial Engineering of Hybridized Solar Cells for Simultaneously Harvesting Solar and Rain Energies. *Journal of Materials Chemistry A* **2017**, *5* (35), 18551–18560.

(18) Ju, H.; Knesting, K. M.; Zhang, W.; Pan, X.; Wang, C.-H.; Yang, Y.-W.; Ginger, D. S.; Zhu, J. Interplay between Interfacial Structures and Device Performance in Organic Solar Cells: A Case Study with the Low Work Function Metal, Calcium. *ACS Applied Materials & Interfaces* **2016**, *8* (3), 2125–2131.

(19) Samadi Khoshkhoo, M.; Peisert, H.; Chassé, T.; Scheele, M. The Role of the Density of Interface States in Interfacial Energy Level Alignment of PTCDA. *Organic Electronics* **2017**, *49*, 249–254.

(20) Zimmerman, J. D.; Xiao, X.; Renshaw, C. K.; Wang, S.; Diev, V. V.; Thompson, M. E.; Forrest, S. R. Independent Control of Bulk and Interfacial Morphologies of Small Molecular Weight Organic Heterojunction Solar Cells. *Nano Letters* **2012**, *12* (8), 4366–4371.

(21) MacQueen, R.; Liebhaber, M.; Niederhausen, J.; Mews, M.; Gersmann, C.; Jäckle, S.; Jäger, K.; Tayebjee, M. J. Y.; Schmidt, T. W.; Rech, B.; et al. Crystalline Silicon Solar Cells with Tetracene Interlayers: The Path to Silicon-Singlet Fission Heterojunction Devices. *Mater. Horiz.* **2018**.

(22) Burdett, J. J.; Bardeen, C. J. The Dynamics of Singlet Fission in Crystalline Tetracene and Covalent Analogs. *Accounts of Chemical Research* **2013**, *46* (6), 1312–1320.

(23) Brawand, N. P.; Goldey, M. B.; Vörös, M.; Galli, G. Defect States and Charge Transport in Quantum Dot Solids. *Chemistry of Materials* **2017**, *29* (3), 1255–1262.

(24) Amsalem, P.; Heimel, G.; Oehzelt, M.; Koch, N. The Interface Electronic Properties of Organic Photovoltaic Cells. *Journal of Electron Spectroscopy and Related Phenomena* **2015**, *204*, 177–185.

(25) Akaike, K.; Kumai, T.; Nakano, K.; Abdullah, S.; Ouchi, S.; Uemura, Y.; Ito, Y.; Onishi, A.; Yoshida, H.; Tajima, K.; et al. Effects of Molecular Orientation of Fullerene Derivative at Donor/Acceptor Interface on Device Performance of Organic Photovoltaics. *Chemistry of Materials* **2018**.

(26) Gregg, B. A.; Hanna, M. C. Comparing Organic to Inorganic Photovoltaic Cells: Theory, Experiment, and Simulation. *Journal of Applied Physics* **2003**, *93* (6), 3605–3614.

(27) Goldey, M. B.; Reid, D.; de Pablo, J.; Galli, G. Planarity and Multiple Components Promote Organic Photovoltaic Efficiency by Improving Electronic Transport. *Physical Chemistry Chemical Physics* **2016**, *18* (46), 31388–31399.

(28) Coropceanu, V.; Cornil, J.; da Silva Filho, D. A.; Olivier, Y.; Silbey, R.; Brédas, J.-L. Charge Transport in Organic Semiconductors. *Chemical Reviews* **2007**, *107* (4), 926–952.

(29) Delgado, M. C. R.; Kim, E.-G.; Filho, D. A. da S.; Bredas, J.-L. Tuning the Charge-Transport Parameters of Perylene Diimide Single Crystals via End and/or Core Functionalization: A Density Functional Theory Investigation. *Journal of the American Chemical Society* **2010**, *132* (10), 3375–3387.

(30) Hestand, N. J.; Tempelaar, R.; Knoester, J.; Jansen, T. L. C.; Spano, F. C. Exciton Mobility Control through Sub − Å Packing Modifications in Molecular Crystals. *Physical Review B* **2015**, *91* (19).

(31) Hestand, N. J.; Spano, F. C. Expanded Theory of H- and J-Molecular Aggregates: The Effects of Vibronic Coupling and Intermolecular Charge Transfer. *Chemical Reviews* **2018**.

(32) Hestand, N. J.; Spano, F. C. Molecular Aggregate Photophysics beyond the Kasha Model: Novel Design Principles for Organic Materials. *Accounts of Chemical Research* **2017**, *50* (2), 341–350.

(33) Spano, F. C. The Spectral Signatures of Frenkel Polarons in H- and J-Aggregates. *Accounts of Chemical Research* **2010**, *43* (3), 429–439.

(34) Beljonne, D.; Yamagata, H.; Brédas, J. L.; Spano, F. C.; Olivier, Y. Charge-Transfer Excitations Steer the Davydov Splitting and Mediate Singlet Exciton Fission in Pentacene. *Physical Review Letters* **2013**, *110* (22).

(35) Austin, A.; Hestand, N. J.; McKendry, I. G.; Zhong, C.; Zhu, X.; Zdilla, M. J.; Spano, F. C.; Szarko, J. M. Enhanced Davydov Splitting in Crystals of a Perylene Diimide Derivative. *The Journal of Physical Chemistry Letters* **2017**, *8* (6), 1118–1123.

(36) Li, Y.; Wang, J.; Xiong, W. Probing Electronic Structures of Organic Semiconductors at Buried Interfaces by Electronic Sum Frequency Generation Spectroscopy. *The Journal of Physical Chemistry C* **2015**, *119* (50), 28083–28089.

(37) Muntwiler, M.; Yang, Q.; Zhu, X.-Y. Exciton Dynamics at Interfaces of Organic Semiconductors. *Journal of Electron Spectroscopy and Related Phenomena* **2009**, *174* (1–3), 116–124.

(38) Chen, Y.; Tamblyn, I.; Quek, S. Y. Energy Level Alignment at Hybridized Organic?Metal Interfaces: The Role of Many-Electron Effects. *The Journal of Physical Chemistry C* **2017**.

(39) Galbraith, M. C. E.; Marks, M.; Tonner, R.; Höfer, U. Formation of an Organic/Metal Interface State from a Shockley Resonance. *The Journal of Physical Chemistry Letters* **2014**, *5* (1), 50–55.

(40) Moon, A. P.; Pandey, R.; Bender, J. A.; Cotton, D. E.; Renard, B. A.; Roberts, S. T. Using Heterodyne-Detected Electronic Sum Frequency Generation To Probe the Electronic Structure of Buried Interfaces. *The Journal of Physical Chemistry C* **2017**, *121* (34), 18653–18664.

(41) Pandey, R.; Moon, A. P.; Bender, J. A.; Roberts, S. T. Extracting the Density of States of Copper Phthalocyanine at the $SiO_2$ Interface with Electronic Sum Frequency Generation. *The Journal of Physical Chemistry Letters* **2016**, *7* (6), 1060–1066.=

(42) Humbert, C.; Dreesen, L.; Nihonyanagi, S.; Masuda, T.; Kondo, T.; Mani, A. A.; Uosaki, K.; Thiry, P. A.; Peremans, A. Probing a Molecular Electronic Transition by Two-Colour Sum-Frequency Generation Spectroscopy. *Applied Surface Science* **2003**, *212–213*, 797–803.

(43) Yamaguchi, S.; Tahara, T. Determining Electronic Spectra at Interfaces by Electronic Sum Frequency Generation: One- and Two-Photon Double Resonant Oxazine 750 at the Air/Water Interface. *The Journal of Chemical Physics* **2006**, *125* (19), 194711.

(44) Shen, Y. R. Basic Theory of Surface Sum-Frequency Generation. *The Journal of Physical Chemistry C* **2012**, *116* (29), 15505–15509.

(45) Yamaguchi, S.; Tahara, T. Development of Electronic Sum Frequency Generation Spectroscopies and Their Application to Liquid Interfaces. *The Journal of Physical Chemistry C* **2015**, *119* (27), 14815–14828.

(46) Aprile, A.; Ciuchi, F.; Pinalli, R.; Dalcanale, E.; Pagliusi, P. Probing Molecular Recognition at the Solid–Gas Interface by Sum-Frequency Vibrational Spectroscopy. *The Journal of Physical Chemistry Letters* **2016**, *7* (15), 3022–3026.

(47) Eisenthal, K. B. Liquid Interfaces Probed by Second-Harmonic and Sum-Frequency Spectroscopy. *Chemical Reviews* **1996**, *96* (4), 1343–1360.

(48) Matsuzaki, K.; Nihonyanagi, S.; Yamaguchi, S.; Nagata, T.; Tahara, T. Vibrational Sum Frequency Generation by the Quadrupolar Mechanism at the Nonpolar Benzene/Air Interface. *The Journal of Physical Chemistry Letters* **2013**, *4* (10), 1654–1658.

(49) Myalitsin, A.; Urashima, S.; Nihonyanagi, S.; Yamaguchi, S.; Tahara, T. Water Structure at the Buried Silica/Aqueous Interface Studied by Heterodyne-Detected Vibrational Sum-Frequency Generation. *The Journal of Physical Chemistry C* **2016**, *120* (17), 9357–9363.

(50) Yamaguchi, S.; Watanabe, H.; Mondal, S. K.; Kundu, A.; Tahara, T. "Up" versus "down" Alignment and Hydration Structures of Solutes at the Air/water Interface Revealed by Heterodyne-Detected Electronic Sum Frequency Generation with Classical Molecular Dynamics Simulation. *The Journal of Chemical Physics* **2011**, *135* (19), 194705.

# Chapter 2: Theory of Electronic Sum Frequency Generation

## 2.1: Introduction

Understanding the interfacial electronic structure of a system presents a unique challenge. While we are familiar with many techniques that allow the study of electronic properties of bulk systems, interfacial tools that can investigate *in situ* properties for a desired material system are lacking. Due to its inherent sensitivity to sample regions that lack inversion symmetry, such as interfaces, sum frequency generation (SFG) can serve this purpose nicely, yet interpreting signals generated in this manner can be tricky.[1–13] Largely, this is due to a lack of understanding of its relation to more familiar processes, such as absorption experiments. For electronic SFG (ESFG), electronic absorption presents a nice starting place to begin our description. Both measure light-matter interactions, with absorption serving as the linear description (meaning the material responds linearly to the impinging electromagnetic field), while ESFG seeks to obtain similar information by using a pair of short electric fields. The advantage of the latter is it gains interface specificity within certain symmetry constraints.[1,3,14] A potentially confusing point, however, is that for an absorption experiment we typically picture the attenuation of an electric field by a system and relate this attenuation to absorption by a sample at specific energies to produce specific excited electronic states within the sample. Alternatively, we can reach an equivalent description by describing how incident light *polarizes* a sample, producing a field by the sample that partially cancels the incident light via destructive interference. This physical picture is particularly powerful for describing ESFG. Therefore, we will slightly alter our understanding of the bulk spectroscopy first, and use this as a stepping stone for describing ESFG. The discussion for ESFG will begin with a basic theoretical description for linear absorption spectroscopy. Instead of describing the way the material alters the

electric field, the response of the *material* to an arbitrary number of applied electric fields will be considered as a *polarization* generated within the system (Figure 2-1).

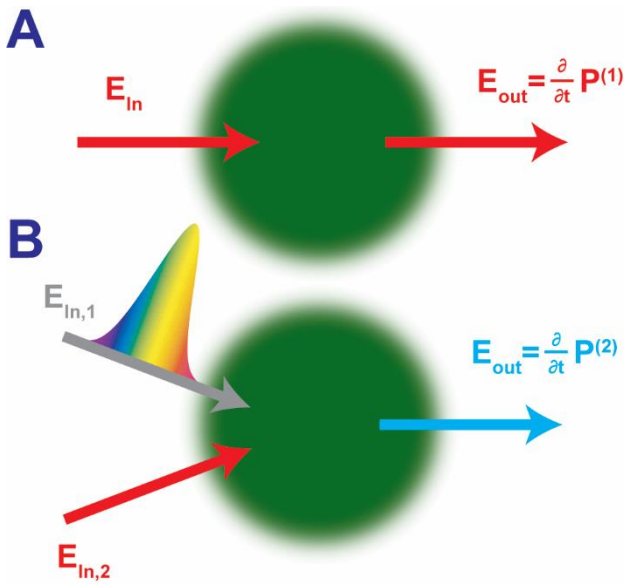


**Figure 2-1**: (A) Cartoon of electric field generated from linear polarization in a material (B) Cartoon of electric field generated form nonlinear polarization in a material

This change to the system will be described by a material response term, here the material susceptibility, $\chi$. The polarization generated in a system by an arbitrary number of fields can then be expanded as the sum of a power series to give a polarization generated by interaction with a number of fields at once. We can first use this method for interpreting absorption to develop a physical understanding, and then describe the higher order, nonlinear response. Chapter 2 will also provide a physical picture for the nature of interface specificity and the interpretation of the nonlinear response of materials through the use of symmetry rules for media that is centrosymmetric in its bulk.

## 2.2: Linear Light/Matter Interactions

We start with a description for linear light-matter interactions and use this as a basis to expand into nonlinear cases. As our goal is to use ESFG and describe it through a generated polarization within a system, we can define how an electric field will interact with a material to generate a polarization within the system. When an electric field impinges on a material, the sample will generate a polarization in response through a dipolar interaction that drives it from the ground state to an excited state. The polarization generated in the material can be described as the convolution of the electric field used to generate the polarization by a term that relates how the material interacts with the field, known as the response function $\mathbf{R}^{(1)}$:

$$\boldsymbol{P}^{(1)}(\mathrm{t}) = \int_{-\infty}^{\infty} \boldsymbol{R}^{(1)}(t-t') \cdot \boldsymbol{E}(t')dt' \tag{2.1}$$

Equation 2.1 represents the linear polarization ($\mathbf{P}^{(1)}$) generated within a material when interacting with a given electric field; the collection of induced dipole moments created in the material in response to the applied electric field can be thought to produce a net transient polarization. $\mathbf{R}^{(1)}$ relates to the susceptibility, $\boldsymbol{\chi}^{(1)}$, of the system through a Fourier transform from the time domain to the frequency domain. $\boldsymbol{\chi}^{(1)}$ describes how the sample responds to the electric field, with its imaginary portion physically manifesting as the absorption spectrum of the material. If **E** can be described as a mono-chromatic plane wave such that

$$\boldsymbol{E}(t) = \boldsymbol{E}(\omega) = \mathcal{E}e^{-i\omega t}, \tag{2.2}$$

then a Fourier transformation of Equation 2.2 provides a much simpler description of the linear polarization of the system:[15,16]

$$\boldsymbol{P}^{(1)}(\mathrm{t}) = \boldsymbol{P}^{(1)}(\omega) = \boldsymbol{\chi}^{(1)}(\omega) \cdot \boldsymbol{E}(\omega) \tag{2.3}$$

And $\boldsymbol{\chi}^{(1)}$is

$$\boldsymbol{\chi}^{(1)}(\omega) = \int_{-\infty}^{\infty} \boldsymbol{\chi}^{(1)}(t) e^{i\omega t} dt \tag{2.4}$$

Taken together, Equations 2.1-2.4 give a description of the linear optical effect that occurs within the material upon interaction with a photon. The photon enters the material, which polarizes in response. This induced polarization will ring out as a function of time as a generated electric field as (see Figure 2-1)

$$\boldsymbol{E}_{induced}(\omega) = \frac{d}{dt}\,\boldsymbol{P}(\omega). \tag{2.5}$$

Due to conservation of momentum, the direction of this radiation is matched to that of the incident field, leading to destructive interference as it leaves the material. If the incident field is energetically resonant with transitions within the material, this polarization is enhanced, and is the source of electronic absorption experiments through $\boldsymbol{\chi}$ as

$$\boldsymbol{\chi} = \boldsymbol{\alpha\mu}, \tag{2.6}$$

where α is the polarizability and μ is the induced dipole moment of the material.

### 2.3: Expansion to Nonlinear Light/Matter Interactions

When describing linear light matter interactions, this is generally where consideration stops. However, we can continue to expand these interactions to incorporate nonlinear interactions between light and matter as well, as the total polarization of the system a sum of the linear polarization with an expansion of nonlinear ones. Assuming that the applied electric field is weak and can thus be described as a perturbation on the system, we can expand the polarization term as a function of **E** as a power series such that[15,16]

$$\begin{aligned}\boldsymbol{P}(\mathrm{t}) = &\int_{-\infty}^{\infty} \boldsymbol{R}^{(1)}(t-t')\cdot\boldsymbol{E}(t')dt' \\ &+ \int_{-\infty}^{\infty} \boldsymbol{R}^{(2)}(t-t_1;t_1-t_2):\boldsymbol{E}(t_1)\boldsymbol{E}(t_2)dt_1\,dt_2 \\ &+ \cdots\end{aligned} \tag{2.7}$$

The terms following $\mathbf{P}^{(1)}$ represent the nonlinear polarizations that occur within the system. It is easy to see then that equation 2.3 can be expanded to include high order polarizations which follow a similar pattern of complexity (here we stop at the second-order polarization

and focus exclusively on the terms needed for ESFG as they are the most relevant for our discussion):

$$\boldsymbol{P}^{(1)}(\omega) = \boldsymbol{\chi}^{(1)}(\omega) \cdot \boldsymbol{E}(\omega)$$
$$\boldsymbol{P}^{(2)}(\omega) = \boldsymbol{\chi}^{(2)}\big(\omega = \omega_i + \omega_j\big) : \boldsymbol{E}(\omega_i)\boldsymbol{E}(\omega_j) \quad (2.8)$$

In Equation 2.8 we have once again taken the Fourier transform of 2.5. Here we can directly begin to draw parallels between the linear polarization that we think of for absorption with that of a higher order term. If $\mathbf{P}^{(1)}$ is the polarization generated in a medium due to an electric field as described by the materials response, $\boldsymbol{\chi}^{(1)}$, we can say something similar for the next higher term. In this case, the second-order polarization term, $\mathbf{P}^{(2)}$, generated in a material through interaction with two electric fields is given through the materials nonlinear susceptibility, $\boldsymbol{\chi}^{(2)}$. This is the basis for how we begin to think about ESFG spectroscopy. An ESFG experiment measures the materials $\boldsymbol{\chi}^{(2)}$ through the use of two fields, in our case the upconversion (a nonresonant field that we use to scatter from a higher energy virtual state as in Figure 2-2) and a white light field (a broadband field that stretches across a region of the electromagnetic spectrum that is resonant with our sample, in the case of ESFG the visible range), and measures the generated electric field it emits from this polarization.

To this point, the discussion for nonlinear interaction is a general description and can be used to describe not only SFG but also other second-order nonlinear interactions such as optical rectification (where one of the fields is zero) and difference frequency generation (where instead of the sum of $\mathbf{E}_1$ and $\mathbf{E}_2$, we instead take the difference). Here, we follow the rotating wave approximation, which states that for a field of sufficiently weak intensity that is near resonance with a material, the quickly oscillating terms within the interaction will average to zero as a function of time. Additionally, the phase matching condition $\mathbf{k} = \mathbf{k}_1 + \mathbf{k}_2$ allows us to select SFG from other second-order interactions. By

placing our detector along the path of the generation beams and measuring the field generated between the two input fields (due to momentum conservation ESFG comes between these two fields while DFG appears outside of these fields) we can selectively measure ESFG. With this basic model of the physical picture for what we are measuring within an ESFG experiment that we have developed, we can now begin to discuss the nature of this $\boldsymbol{\chi}^{(2)}$ for the system that we measure as well as the source of ESFG's interface selectivity in the section below.

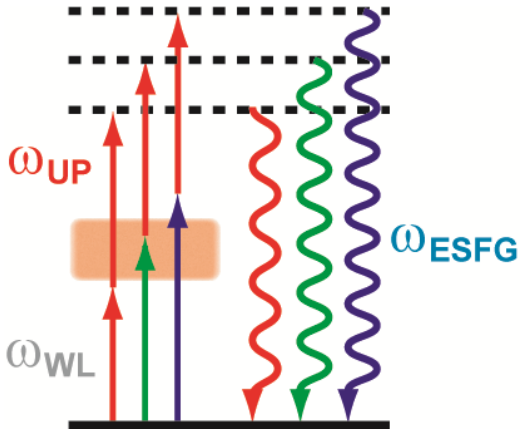


**Figure 2-2**: Cartoon for ESFG generation condition

### 2.4: Establishing $\chi^{(2)}$ and ESFG

Now that we have a description of the physical representation of $\boldsymbol{\chi}^{(2)}$ (as well as its link to the better-known technique of absorption) we can begin to discuss the nature of the nonlinear susceptibility itself. First, the susceptibility of a system is a tensor of rank n+1, where n is the order of interaction, meaning that in the case of absorption the first-order susceptibility is a second-rank tensor (a 3x3 matrix), and for ESFG our second order nonlinear susceptibility is a third-rank tensor ( a 3x3x3 matrix) with elements $\boldsymbol{\chi}^{(2)}_{i,j,k}$. This can be somewhat intuitively determined, as $\mathbf{E}^{(2)}$ and $\mathbf{P}^{(2)}$ are vector quantities, which therefore require a the nonlinear susceptibility term to be a 3D matrix that describes how

each $\hat{x}$, $\hat{y}$, and $\hat{z}$ component of $\mathbf{E}_1$ ($\hat{j}$) and $\mathbf{E}_2$ ($\hat{k}$) impact the $\hat{x}$, $\hat{y}$, and $\hat{z}$ component of the generation polarization ($\hat{i}$). Given that $\hat{i}$, $\hat{j}$, and $\hat{k}$ represent the direction of our produced polarization relative to the orientation of our incoming fields, the experimental orientation we choose is important to our interpretation of our measured ESFG. Below is a cartoon that represents the experimental frame of reference that we choose for our system (Figure 2-3).

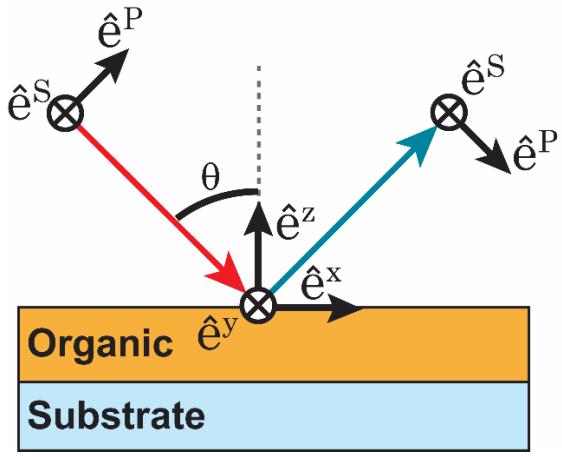


**Figure 2-3:** Frame of reference used for ESFG experiments

In Figure 2-3, we see that we have not just one frame of reference we need to consider, but two. The first is the "lab" frame of reference where we have control over the polarization of our generation fields. These polarizations can be either "$\hat{S}$" or "$\hat{P}$", where for $\hat{S}$ the electric field lies perpendicular to the plain of reflection from the sample, while for $\hat{P}$ the electric field lies within the plain reflection. For the sample frame, which contains the relevant parameters for our nonlinear susceptibility, we have $\hat{x}$, $\hat{y}$, and $\hat{z}$ such that $\hat{z}$ is normal to the surface with $\hat{x}$ along the beam path of incidence/reflection, and $\hat{x}$ and $\hat{y}$ lie along the surface of the sample. This then provides a frame of reference for $\boldsymbol{\chi}^{(2)}_{i,j,k}$, and allows us to write instead, for example, $\boldsymbol{\chi}^{(2)}_{x,y,z}$. We can now say that $\boldsymbol{\chi}^{(2)}_{x,y,z}$ is a third rank tensor,

with individual elements that determine, from Equation 2.8, the polarization generated within a material along the sample axis frame of $\hat{x}$, $\hat{y}$, and $\hat{z}$. We can also see clearly from Figure 2-3 that we can relate the lab frame polarizations to particular indices of the sample frame, namely that $\hat{S}$ polarization exclusively probes the $\hat{y}$-axis of the sample frame, and $\hat{P}$ probes both $\hat{x}$ and $\hat{z}$. How then, do we determine the elements of $\boldsymbol{\chi}^{(2)}$ we want to measure, and how does the surface specificity of ESFG occur?

For the material systems we wish to study with ESFG, we are limiting ourselves to those that are centrosymmetric (the material has a symmetric center of inversion). This single idea allows for a large reduction in the number of independent elements of $\boldsymbol{\chi}^{(2)}$. If our system of interest is centrosymmetric, inversion of Equation 2.8 will cause our vector components to gain negative signs, while our tensor element inherently remains the same as the system has no preference for orientation:[1,3,5,15,16]

$$-\boldsymbol{P}^{(2)}(\omega) = \boldsymbol{\chi}^{(2)}(\omega) : \left(-\boldsymbol{E}(\omega_i)\left(-\boldsymbol{E}(\omega_j)\right)\right) \tag{2.9}$$

$$-\boldsymbol{P}^{(2)}(\omega) = \boldsymbol{\chi}^{(2)}(\omega) : \boldsymbol{E}(\omega_i)\boldsymbol{E}(\omega_j)$$

As the negative signs applied to the electric fields cancel, the right side of Equation 2.9 is equal to that of 2.8, and by substitution:

$$-\boldsymbol{P}^{(2)}(\omega) = \boldsymbol{P}^{(2)}(\omega) \tag{2.10}$$

For this equality to be true, the only valid conclusion is that $\boldsymbol{\chi}^{(2)}$ must be zero within the bulk of the sample. What then happens if we consider an interface between two isotropic materials, such as at the air:organic interface presented in Figure 2-3? In this scenario we have a necessary breakage of symmetry along the $\hat{z}$-axis. Thus, with a reduction in the symmetry of the system when considering an interface, Equations 2.8 and 2.9 aren't required to be equal, and our nonlinear susceptibility becomes non-zero. We can also use the symmetry of the interface to reduce the elements within $\boldsymbol{\chi}^{(2)}$ we need to measure. Assuming the interface is isotropic within the plane of the sample, we are invariant to both

$\hat{x}$ and $\hat{y}$, meaning that $\hat{x} = -\hat{x} = \hat{y} = -\hat{y}$. We can make use of von Neumann's principle, (which states that any physical property of a system must have the same symmetry of the point group it describes, in our case a $C_\infty$ rotation along the $\hat{z}$-axis) such that:[5,15]

$$\boldsymbol{\chi}^{(2)}_{i,j,k} = \boldsymbol{\chi}^{(2)}_{i',j',k'} \tag{2.11}$$

$$\boldsymbol{\chi}^{(2)}_{i,j,k} = sign(\hat{i'})sign(\hat{j'})sign(\hat{k'})\boldsymbol{\chi}^{(2)}_{i',j',k'} \tag{2.12}$$

Here, sign is the sign function and gives ± 1. Taking Equations 2.11 and 2.12, we can reduce the number of unique elements within $\boldsymbol{\chi}^{(2)}$. For both to remain true, the sign of $\boldsymbol{\chi}^{(2)}$ must remain the same after rotation. As our interface is isotropic within the plane of the sample, sign changes of $\hat{x}$ and $\hat{y}$ won't affect our sign, but this isn't true for the $\hat{z}$-axis. As we have a breakage of symmetry along the $\hat{z}$-axis, we need an odd number of $\hat{z}$ elements for valid rotations, and therefore all elements within $\boldsymbol{\chi}^{(2)}$ that probe an even number of $\hat{z}$-axis components must be zero. Thus, for an element within the $\boldsymbol{\chi}^{(2)}$ tensor to be non-zero, either all indices must be $\hat{z}$, or at least one of $\hat{\imath}$, $\hat{\jmath}$, or $\hat{k}$ must lie along $\hat{z}$. This narrows the 27 elements of $\boldsymbol{\chi}^{(2)}$ to just seven elements, which can then be further narrowed as $\hat{x}$ and $\hat{y}$ are equivalent assuming $C_\infty$ symmetry within the $\hat{x}\hat{y}$ plane, leaving only four unique elements for $\boldsymbol{\chi}^{(2)}$:[5,15,17]

$$\boldsymbol{\chi}^{(2)}_{yyz} = \boldsymbol{\chi}^{(2)}_{xxz}\,;\, \boldsymbol{\chi}^{(2)}_{yzy} = \boldsymbol{\chi}^{(2)}_{xzx}\,;\, \boldsymbol{\chi}^{(2)}_{zyy} = \boldsymbol{\chi}^{(2)}_{zxx}\,;\, \boldsymbol{\chi}^{(2)}_{zzz} \tag{2.13}$$

Now that we have identified the non-zero elements of our non-linear susceptibility and an understanding of the source of ESFG's interface specificity for the systems we are studying, we can probe these four elements in the sample frame from our lab by characterizing how the polarization of the emitted ESFG depends on that of each of the generating fields. As mentioned earlier, our lab frame, $\hat{P}$ and $\hat{S}$, probe independently $\hat{x}$ and $\hat{z}$ for $\hat{P}$ and $\hat{y}$ for $\hat{S}$. With control of the polarization of our generating beams and polarized detection optics, we can probe all four of the non-zero elements within our $\boldsymbol{\chi}^{(2)}$ through four unique polarization mapping conditions:[14]

$$\begin{aligned} \boldsymbol{\chi}_{\mathrm{SSP}}^{(2)} &= \boldsymbol{\chi}_{\mathrm{yyz}}^{(2)}; \\ \boldsymbol{\chi}_{\mathrm{SPS}}^{(2)} &= \boldsymbol{\chi}_{\mathrm{yzy}}^{(2)}; \\ \boldsymbol{\chi}_{\mathrm{PSS}}^{(2)} &= \boldsymbol{\chi}_{\mathrm{zyy}}^{(2)}; \\ \boldsymbol{\chi}_{\mathrm{PPP}}^{(2)} &= \boldsymbol{\chi}_{\mathrm{xxz}}^{(2)} + \boldsymbol{\chi}_{\mathrm{xzx}}^{(2)} + \boldsymbol{\chi}_{\mathrm{zxx}}^{(2)} + \boldsymbol{\chi}_{\mathrm{zzz}}^{(2)} \end{aligned} \tag{2.14}$$

Above, we have listed the polarization for a given experiment in order of ESFG, upconversion, and white light. At first it may seem that our ability to probe $\boldsymbol{\chi}_{\mathrm{zzz}}^{(2)}$ is hindered, as $\boldsymbol{\chi}_{\mathrm{PPP}}^{(2)}$ probes four additional elements of our nonlinear susceptibility tensor (this is a result of $\hat{\mathrm{P}}$ lying in the $\hat{x}$-$\hat{z}$ plane for our sample). However, it is important to remember Equation 2.10, such that if we measure $\boldsymbol{\chi}_{\mathrm{SSP}}^{(2)}$, $\boldsymbol{\chi}_{\mathrm{SPS}}^{(2)}$, and $\boldsymbol{\chi}_{\mathrm{PSS}}^{(2)}$ first, we can determine the first four elements of $\boldsymbol{\chi}_{\mathrm{PPP}}^{(2)}$ individually, and determine $\boldsymbol{\chi}_{\mathrm{zzz}}^{(2)}$ using these. Finally, we can relate the nonlinear susceptibility of $\boldsymbol{\chi}^{(2)}$ to the polarizability in the same way as we did above for absorption as in Equation 2.6. The generated dipole moment will be enhanced where the material has electronic states energetically resonant with the white light field, and as such the generated ESFG at the sum of these with the upconversion field will be enhanced and appear as a significant increase in signal at the detector. In this manner, we can calculate the energies for electronic states at the interface by subtracting the energy of the upconversion field, and thus have the effect of an interface specific electronic absorption experiment.

This Chapter has shown a basic background of the theory behind physical picture of ESFG and specifically how it relates to an absorption experiment. We can now begin to discuss the measured nonlinear susceptibilities from our experiments with an understanding for the physical picture they represent below.

## 2.5: Conclusion

For Chapter 2, we started with a basic description for light matter interactions in terms of the polarization generated in a material and how it relates to electronic absorption spectroscopy. The polarization generated in the material through interaction with a given electric field is determined by its susceptibility, $\boldsymbol{\chi}$. We then expanded the polarization to account for higher order, nonlinear effects that describe how matter simultaneously interacts with pairs of electric fields. Through symmetry arguments, we find that this is an interface-specific process for centrosymmetric media, and we can fully characterize its non-zero nonlinear susceptibility by measuring how the polarization of the emitted ESFG signal depends on that of its driving fields. We can measure the nonlinear susceptibility $\boldsymbol{\chi}^{(2)}$ and relate it to energetic states present in the material as an experiment akin to an interface specific electronic absorption experiment. This description will form the basis for our understanding of the measured ESFG spectra in later Chapters and inform how we describe the interfacial states of the material relative to that of its bulk.

## 2.6: Chapter References


(1) Shen, Y. R. Basic Theory of Surface Sum-Frequency Generation. *The Journal of Physical Chemistry C* **2012**, *116* (29), 15505–15509.

(2) Matsuzaki, K.; Nihonyanagi, S.; Yamaguchi, S.; Nagata, T.; Tahara, T. Vibrational Sum Frequency Generation by the Quadrupolar Mechanism at the Nonpolar Benzene/Air Interface. *The Journal of Physical Chemistry Letters* **2013**, *4* (10), 1654–1658.

(3) Myalitsin, A.; Urashima, S.; Nihonyanagi, S.; Yamaguchi, S.; Tahara, T. Water Structure at the Buried Silica/Aqueous Interface Studied by Heterodyne-Detected Vibrational Sum-Frequency Generation. *The Journal of Physical Chemistry C* **2016**, *120* (17), 9357–9363.

(4) Simpson, G. J.; Perry, J. M.; Ashmore-Good, C. L. Molecular and Surface Hyperpolarizability of Oriented Chromophores of Low Symmetry. *Physical Review B* **2002**, *66* (16).

(5) Davis, R. P.; Moad, A. J.; Goeken, G. S.; Wampler, R. D.; Simpson, G. J. Selection Rules and Symmetry Relations for Four-Wave Mixing Measurements of Uniaxial Assemblies. *The Journal of Physical Chemistry B* **2008**, *112* (18), 5834–5848.

(6) Deng, F.; Ulcickas, J. R. W.; Simpson, G. J. Theoretical Foundation for Electric-Dipole-Allowed Chiral-Specific Fluorescence Optical Rotary Dispersion (F-ORD) from Interfacial Assemblies. *The Journal of Physical Chemistry Letters* **2016**, *7* (21), 4248–4252.

(7) Dailey, C. A.; Burke, B. J.; Simpson, G. J. The General Failure of Kleinman Symmetry in Practical Nonlinear Optical Applications. *Chemical Physics Letters* **2004**, *390* (1–3), 8–13.

(8) Dow, X. Y.; DeWalt, E. L.; Newman, J. A.; Dettmar, C. M.; Simpson, G. J. Unified Theory for Polarization Analysis in Second Harmonic and Sum Frequency Microscopy. *Biophysical Journal* **2016**, *111* (7), 1553–1568.

(9) Moad, A. J.; Simpson, G. J. A Unified Treatment of Selection Rules and Symmetry Relations for Sum-Frequency and Second Harmonic Spectroscopies. *The Journal of Physical Chemistry B* **2004**, *108* (11), 3548–3562.

(10) Yamaguchi, S.; Tahara, T. Determining Electronic Spectra at Interfaces by Electronic Sum Frequency Generation: One- and Two-Photon Double Resonant Oxazine 750 at the Air/Water Interface. *The Journal of Chemical Physics* **2006**, *125* (19), 194711.

(11) Yamaguchi, S.; Shiratori, K.; Morita, A.; Tahara, T. Electric Quadrupole Contribution to the Nonresonant Background of Sum Frequency Generation at Air/liquid Interfaces. *The Journal of Chemical Physics* **2011**, *134* (18), 184705.

(12) O'Brien, D. B.; Massari, A. M. Experimental Evidence for an Optical Interference Model for Vibrational Sum Frequency Generation on Multilayer Organic Thin Film Systems. II. Consideration for Higher Order Terms. *The Journal of Chemical Physics* **2015**, *142* (2), 024704.

(13) O'Brien, D. B.; Massari, A. M. Experimental Evidence for an Optical Interference Model for Vibrational Sum Frequency Generation on Multilayer Organic Thin Film Systems. I. Electric Dipole Approximation. *The Journal of Chemical Physics* **2015**, *142* (2), 024703.

(14) O'Brien, D. B.; Massari, A. M. Modeling Multilayer Thin Film Interference Effects in Interface-Specific Coherent Nonlinear Optical Spectroscopies. *Journal of the Optical Society of America B* **2013**, *30* (6), 1503.

(15) Boyd, R. W. *Nonlinear Optics, Third Edition*, 3rd ed.; Academic Press, 2008.

(16) Shen, Y. R. *The Principles of Nonlinear Optics*; Wiley, 1984.

(17) Pandey, R.; Moon, A. P.; Bender, J. A.; Roberts, S. T. Extracting the Density of States of Copper Phthalocyanine at the $SiO_2$ Interface with Electronic Sum Frequency Generation. *The Journal of Physical Chemistry Letters* **2016**, *7* (6), 1060–1066.

# Chapter 3: Modeling Thin Film Optical Interference Contributions to ESFG Spectra[1]

## 3.1: Introduction

To fully understand the processes by which energy transfer proceeds at buried interfaces in semi-conductor devices, it is necessary to know both their morphology and energetic Density of States (DoS) *in situ*. However, this is a difficult task to achieve, as most spectroscopic or probing tip methods that give information of this nature are inherently either most sensitive to the bulk (such as electronic absorption and x-ray diffraction), or are sensitive only to the top most interface (such as atomic force microscopy). Determining morphology and the energetics of an interface are further complicated when the medium we wish to study is *molecular* in nature (organic semi-conductors) as long- and short-range intermolecular interactions are strongly affected by the way these molecules pack together.

Electronic sum frequency generation (ESFG) serves as a powerful tool to solve these problems as it is not only an interface selective energetic probe for centrosymmetric media, it can also provide morphological information through the control of polarization of the generation and measurement beams.[1–4] Also, as ESFG is a light-based technique, it is well suited to studying buried interfaces *in situ* provided consideration is taken for absorption within the layers as the fields (both pump and ESFG) move through the device. Despite these many advantages, ESFG suffers from a particular flaw as while it is interface

[1] Previously published as Pandey, R.; Moon, A. P.; Bender, J. A.; Roberts, S. T. Extracting the Density of States of Copper Phthalocyanine at the $SiO_2$ Interface with Electronic Sum Frequency Generation. *J. Phys. Chem. Lett.* **2016**, *7*(6), 1060-1066 Supplementary Information. My contributions to this paper include helping make samples, helping collect ESFG spectra, building the ESFG spectrometer, creation of thin film modeling software, modeling and fitting ESFG spectra, and interpreting the spectra and writing the paper with my colleagues.

specific, it is not specific to a *particular* interface. Taking a thin film of approximately 100 nm of organic semi-conductor (OSC) deposited on glass ($SiO_2$) as an example, this means that we will generate signal not only from the OSC:$SiO_2$ interface, but also from the air:OSC junction above. The presence of two ESFG active interfaces within a thin film system will lead to interference of signals from each interface that can convolute extraction of the DoS from the interface of interest. To mitigate the potential difficulty presented by this interference, we have developed a thin film interference modeling program. This program gives us not only the ability to model these effects, but also to leverage this interference to our advantage by growing films of different thicknesses to determine the contribution from both air-exposed and buried interfaces through changes in the measured interference pattern. In this Chapter, we will briefly present the method used to achieve this goal as well as describe an example system that will be discussed in more detail in later chapters.

### 3.2: Theory

The model used to predict the influence of interference between ESFG fields emitted by two interfaces within a thin film system is based on an approach developed by O'Brien and Massari for the treatment of vibrational SFG spectra.[5–9] This model accounts for attenuation of the excitation and ESFG fields due to a sample's absorption as well as the interference between fields by taking an infinite sum over the Fresnel coefficients for transmission and reflection associated with each sample boundary. As an example, we will use a thin film of copper phthalocyanine on a glass substrate to illustrate this thin film modeling system. Figure 3-1A defines the frame of reference used for our model. To calculate the electric field about a specific sample interface, we break the sample into two subsystems, one above and one below the interface of interest (Figure 3-1B). An input

transfer matrix is then defined that takes fields from the lab frame (S or P polarized light) and transfers them through the appropriate subsystem into an electric polarization at this interface within the frame of the sample (x, y, and z) under the electric dipole and plane wave approximations:

$$\boldsymbol{P}_{v}^{NL} = \boldsymbol{\chi}_{v}^{(2)} : (\boldsymbol{T}_{Air,v}^{WL}\boldsymbol{E}_{WL})(\boldsymbol{T}_{Air,v}^{Up}\boldsymbol{E}_{Up}). \tag{3.1}$$

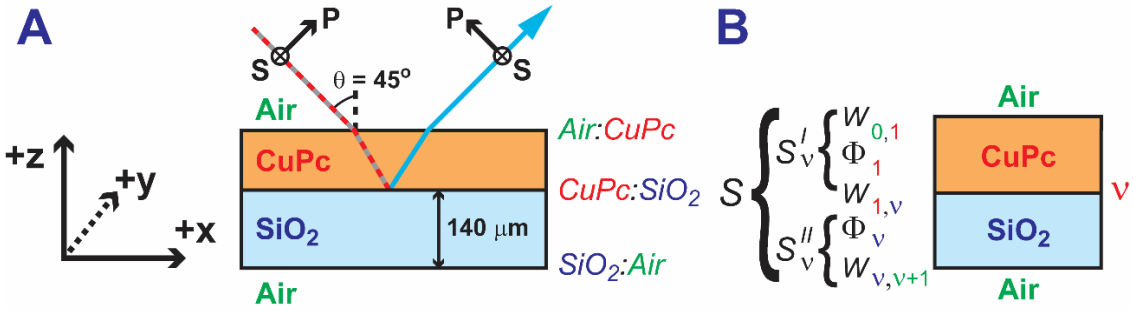


**Figure 3-1:** (A)Frame of reference used for our thin film interference model (B) Example showing how the system is broken into subsystems about an interface. **S**, **W**, and **Φ** are discussed below (Equations 3.6-3.12). Adapted from reference.[6]

Here, $\boldsymbol{P}_{v}^{NL}$ is the nonlinear polarization generated at the interface of interest, *v*, as represented by the electric fields in the sample (x, y, and z) frame. $\boldsymbol{T}_{Air,v}^{WL/Up}$ is the input transfer matrix that transforms the incoming electric field $\boldsymbol{E}_{WL/Up}$ from air in the lab frame (S or P) into an electric field at interface *v* with contributions along x, y, and z. This is achieved through the creation of a total system transfer matrix, **S**, that accounts for the phase of the field as it passes through a layer, **Φ**, and the matrix of refraction, **W**, which generates the electric field on either side of an interface. These will be defined below (see Equations 3.6 – 3.12). Once the polarization at interface *v* is calculated, the electric field generated at this interface is then transferred out of the system via either reflection or transmission back to the lab frame:

$$\boldsymbol{E}_{v,Air}^{ESFG} = \boldsymbol{T}_{v,Air}^{ESFG} \boldsymbol{P}_{v}^{NL}. \tag{3.2}$$

$\boldsymbol{E}_{v,Air}^{ESFG}$ is the outgoing electric field generated by the nonlinear polarization at interface *v* and transformed into the lab frame of reference via the output transfer matrix, $\boldsymbol{T}_{v,Air}^{ESFG}$. Using this method, thin film interference may be considered separately from the molecular response of the sample. This allows us to calculate the outgoing transfer coefficient for each interface individually and then modify each interfacial transfer coefficient by multiplication with a molecular response that is potentially unique to each interface (see Equations 3.3 and 3.4). The sum of each interfacial contribution to the nonlinear polarization of the sample is calculated and the absolute value taken and squared to generate the calculated ESFG signal for the total system for SSP and PPP measurements (where SSP or PPP are the polarizations for the ESFG, upconversion, and whitelight fields, respectively):

$$I_{SSP} \propto \left|(T_{YYZ,Air}\chi_{YYZ,Air} + T_{YYZ,SiO_2}\chi_{YYZ,SiO_2} + T_{YYZ,SiO_2:Air}\chi_{YYZ,SiO_2:Air})E_{Up,S}E_{WL,P}\right|^2 \tag{3.3}$$

$$\begin{aligned} I_{PPP} \propto |([&T_{XXZ,Air}\chi_{YYZ,Air} + T_{XXZ,SiO_2}\chi_{YYZ,SiO_2} + T_{XXZ,SiO_2:Air}\chi_{YYZ,SiO_2:Air}] \\ &+[T_{XZX,Air}\chi_{YZY,Air} + T_{XZX,SiO_2}\chi_{YZY,SiO_2} + T_{XZX,SiO_2:Air}\chi_{YZY,SiO_2:Air}] \\ &+[T_{ZXX,Air}\chi_{ZYY,Air} + T_{ZXX,SiO_2}\chi_{ZYY,SiO_2} + T_{ZXX,SiO_2:Air}\chi_{ZYY,SiO_2:Air}] \\ &+\left[T_{ZZZ,Air}\chi_{ZZZ,Air} + T_{ZZZ,SiO_2}\chi_{ZZZ,SiO_2} + T_{ZZZ,SiO_2:Air}\chi_{ZZZ,SiO_2:Air}\right]E_{Up,P}E_{WL,P}|^2 \end{aligned} \tag{3.4}$$

$$\boldsymbol{T}_{v} = \boldsymbol{T}_{v,Air}^{out,SFG}\boldsymbol{T}_{Air,v}^{in,Up}\boldsymbol{T}_{Air,v}^{in,WL} \tag{3.5}$$

In Equations 3.3 and 3.4, we explicitly write the contributions to the signal from the nonlinear susceptibility elements associated with each interface within our sample films

for two polarizations, SSP and PPP (the equivalent equations for SPS and PSS can be written by permutation of the indices). Here, the subscript "Air" represents the OSC:Air interface while "$SiO_2$" the OSC:$SiO_2$ interface. We also include a new label "$SiO_2$:Air," to denote the $SiO_2$:Air interface at the bottom of our sample films. We explicitly assume that its associated values of $\chi_{YYZ}$, $\chi_{YZY}$, $\chi_{ZYY}$, and $\chi_{ZZZ}$ are zero due to the lack of electronic resonance between our excitation fields and our $SiO_2$ substrates as well as the absence of ESFG signal from a bare $SiO_2$ substrate. While this removes contributions from the $SiO_2$:Air interface to the SFG signal itself, this interface is still considered when calculating the transfer matrix elements that account for reflections within each sample. Also of note, as our ESFG signals display no dependence on the film orientation within the plane of reflection, our sample films possess apparent azimuthal symmetry. Thus, the x and y directions are equivalent when calculating the sample's nonlinear susceptibility (i.e. $\chi_{YYZ} = \chi_{XXZ}$). We have taken advantage of this symmetry to write Equations 3.3 purely in terms of y-dependent susceptibility elements. However, as the transfer matrices that appear in Equation 3.4 are comprised of Fresnel coefficients that differ for x and y field components (see Equation 3.9 below), these terms are not symmetric about these directions (i.e. $T_{YYZ} \neq T_{XXZ}$) and we explicitly account for the directional dependence of these terms in our model.

To construct the input and output transfer coefficients for the system, we must account for the infinite number of reflections of each excitation beam and emitted ESFG field within our thin film samples. To do this we construct a total system transfer matrix, $\boldsymbol{S}$, that accounts for reflection and refraction at each interface, changes in the relative phase of each field as they pass through a layer, and the attenuation of each field due to absorption by each sample layer (Figure 3-1B):

$$\boldsymbol{S} = (\prod_{v=0}^{v_{final}-1} \boldsymbol{W}_{v,v+1}\,\boldsymbol{\Phi}_{v+1})\boldsymbol{W}_{v_{final}-1,v_{final}} \tag{3.6}$$

Here, $\boldsymbol{S}$ is constructed from the multiplication of a phase matrix $\boldsymbol{\Phi}$ that accounts for propagation through layer $v + 1$ and a matrix of refraction $\boldsymbol{W}$ across the interface from layer $v$ to $v + 1$, and represents a sum over the infinite series of reflection and transmission events within the sample. The relationship between $\boldsymbol{S}$ and each of the input and output transfer coefficients described above has been discussed at length by O'Brien and Massari.[6] Equations 3.7 and 3.8 show the construction of the matrix of refraction, which relates fields on either side of an interface to those traveling either to or from that interface:

$$\boldsymbol{W}_{v-1,v} = \frac{1}{t_{v-1,v}}\begin{bmatrix} 1 & r_{v-1,v} \\ r_{v-1,v} & 1 \end{bmatrix} \tag{3.7}$$

$$\begin{bmatrix} E_v^- \\ E_v^+ \end{bmatrix} = \boldsymbol{W}_{v-1,v}\begin{bmatrix} E_v^{-\prime} \\ E_v^{+\prime} \end{bmatrix} \tag{3.8}$$

The subscript "$v$-1,$v$" indicates a property associated with moving from layer $v$-1 to layer $v$ while the subscript "$v$" denotes the $v$th interface within a sample. The superscripts "+" and "-" denote fields moving in the + or – directions along the z-axis in the sample frame and the inclusion of a prime indicates that the field exists below interface $v$ along the z-axis. Therefore, $E_v^+$ and $E_v^{-\prime}$ both indicate travel away from interface $v$, with the former showing travel along the positive z-direction above the interface and the latter travel along the negative z-direction. Within the matrix of refraction, $r_{v-1,v}$ and $t_{v-1,v}$ represent the linear Fresnel coefficients for reflection and transmission at the boundary between layer $v$-1 and $v$ and vary for S and P polarized light:

$$r_{v-1,v}^P = \frac{n_{v-1}\cos(\theta_v) - n_v\cos(\theta_{v-1})}{n_{v-1}\cos(\theta_v) + n_v\cos(\theta_{v-1})} \tag{3.9a}$$

$$r_{v-1,v}^{S} = \frac{n_{v-1}\cos(\theta_{v-1}) - n_v\cos(\theta_v)}{n_{v-1}\cos(\theta_{v-1}) + n_v\cos(\theta_v)} \tag{3.9b}$$

$$t_{v-1,v}^{P} = \frac{2n_{v-1}\cos(\theta_{v-1})}{n_{v-1}\cos(\theta_v) + n_v\cos(\theta_{v-1})} \tag{3.9c}$$

$$t_{v-1,v}^{S} = \frac{2n_{v-1}\cos(\theta_{v-1})}{n_{v-1}\cos(\theta_{v-1}) + n_v\cos(\theta_v)} \tag{3.9d}$$

In Equations 3.9a - 3.9d, $\theta$ is the angle of the beam in either layer *v* or *v*-1 and $n_v$ is the complex refractive index of layer *v*. The phase matrix is used to calculate the spatial phase offset for a field as it travels through a layer (Equations 3.10 - 3.12).

$$\boldsymbol{\Phi}_v = \begin{bmatrix} e^{-i\phi_v} & 0 \\ 0 & e^{i\phi_v} \end{bmatrix} \tag{3.10}$$

$$\begin{matrix} E_{v+1}^{-\prime} \\ E_{v+1}^{+\prime} \end{matrix} = \boldsymbol{\Phi}_v \begin{matrix} E_{v+1}^{-} \\ E_{v+1}^{+} \end{matrix} \tag{3.11}$$

$$\phi_v = \frac{2\pi n_v}{\lambda} d_v \cos(\theta_v) \tag{3.12}$$

For equation 3.12, $\lambda$ is the vacuum wavelength of the beam in question and $d_v$ is the length of layer *v*. To construct sublayers, this process is the same except the system is divided into two separate systems around the interface of interest. As an example, we will discuss the modeling of the ESFG field generated using optical constants for a thin film of octyl perylene diimide derivative on top of an $SiO_2$ substrate, discussed in more detail in Chapters 6 and 7.

### 3.3: Results

Now that we have a method for modeling interference from two active ESFG interfaces in a sample we can predict measured ESFG spectra as a function of the thickness of our OSC thin films and the wavelength of the generated ESFG. In Figure 3-2, we show

model calculations for a PPP polarization experiment. Looking only at Figure 3-2 A to start, we see that the calculated ESFG spectra have an oscillatory signal intensity that "beats" in strength as a function of the thickness of the OSC film. This is consistent with the presence of interference due to multiple ESFG active interface for signal generation that are separated by a small distance (~10's to 100's of nanometers). The location of the peaks in the ESFG signal intensity at ~50 nm and ~150 nm is set by the polarization combination and complex refractive index for the particular molecular system and substrate used. We also see oscillations in the ESFG intensity as a function of the ESFG energy, with peaks at $\lambda_{ESFG}$ = ~325 nm and $\lambda_{ESFG}$ = ~355 nm. For this calculation, these oscillations are also a function of the polarization and complex refractive index, as our molecular response is set such that it doesn't vary as a function of energy.

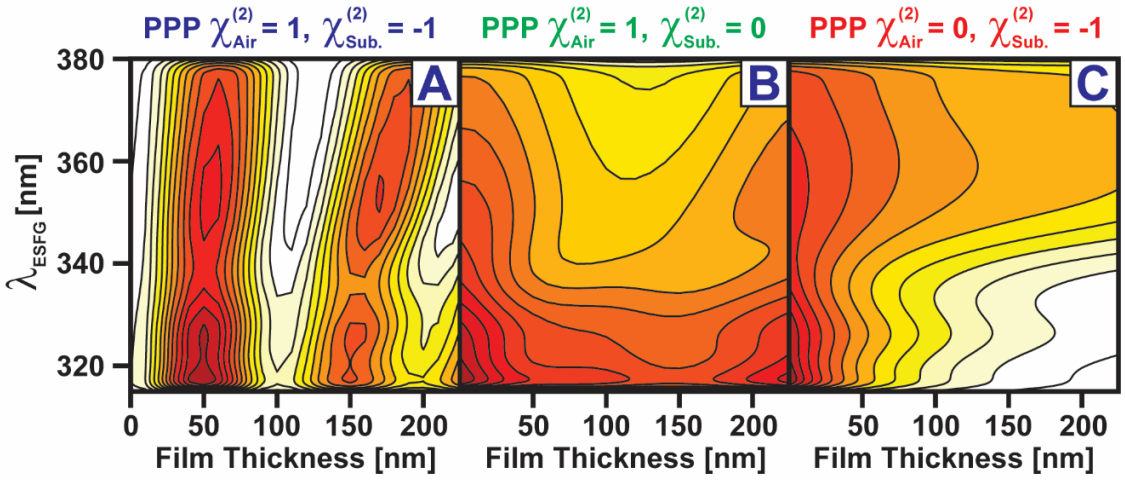


**Figure 3-2**: Model calculation of PPP polarization combination for ESFG spectra as a function of thickness (A) Calculation for $\boldsymbol{\chi}^{(2)}_{\text{Air}}$ = 1 and $\boldsymbol{\chi}^{(2)}_{\text{Sub.}}$ = -1 (B) Calculation for $\boldsymbol{\chi}^{(2)}_{\text{Air}}$ = 1 and $\boldsymbol{\chi}^{(2)}_{\text{Sub.}}$ = 0 (C) (B Calculation for $\boldsymbol{\chi}^{(2)}_{\text{Air}}$ = 0 and $\boldsymbol{\chi}^{(2)}_{\text{Sub.}}$ = -1

As the model separates the interference effects from the molecular response when calculating the ESFG spectra, we can vary our materials response (the nonlinear

susceptibility term $\boldsymbol{\chi}^{(2)}$ as discussed in Chapter 2) for each interface *individually* to determine if we can detect differences within our spectra. As $\boldsymbol{\chi}^{(2)}$ is a complex value for the response of the material, this is done by setting a value for the imaginary portion of the $\boldsymbol{\chi}^{(2)}$ and then calculating a Kramers-Kronig consistent real portion. In Figure 3-2A, we calculate the spectra with our molecular response terms set such that the air exposed interface ($\boldsymbol{\chi}_{\mathrm{Air}}^{(2)}$) is set to one and the molecular interface next to our substrate ($\boldsymbol{\chi}_{\mathrm{Sub.}}^{(2)}$) is oppositely signed as negative one (still modeling the response of the molecule). Here we are making two approximations: first, that the imaginary portion of the molecular response is flat as a function of energy, and second that the buried interface should be oppositely signed relative to the air exposed interface. The first approximation is done to simplify the model calculation for the discussion in this Chapter, and in later Chapters the $\boldsymbol{\chi}^{(2)}$ is treated as a fitting parameter for the collected ESFG data. The second approximation is used as an initial guess for orientation of the dipolar response for molecules that are on opposite sides of the same film, essentially modeling assuming their response is equal, but in the opposite direction.

Figure 3-2B changes the molecular response such that $\boldsymbol{\chi}_{\mathrm{Air}}^{(2)}$ is set to one and $\boldsymbol{\chi}_{\mathrm{Sub.}}^{(2)}$ is set to zero. By constructing our molecular response in this fashion, we can separate the response to our total spectra in 3-2A that comes only from the air exposed interface, as this effectively turns "off" the interface next to the substrate but allows the air exposed interface to be calculated as a function of the internal reflections and transmission within the sample. We see that the generated ESFG signal for the air exposed interface is initially strong at thin film thicknesses, then decreases as we approach a film thickness of ~75 nm, and seems to recover as the thickness gets close to ~200 nm. This initially seems counterintuitive but is likely due to interference from ESFG generated at the top interface propagating into the

sample, reflecting off of the substrate, and exiting through the air exposed surface again to destructively interfere with the initial ESFG signal.

Looking at Figure 3-2C, we have done the opposite of 3-2B and instead set $\boldsymbol{\chi}_{\mathrm{Air}}^{(2)}$ is set to zero and $\boldsymbol{\chi}_{\mathrm{Sub.}}^{(2)}$ back to negative one. In this scenario, we see strong ESFG at thin film thicknesses that only decreases as the film is grown. This can be understood be recognizing that using the complex refractive index for the material also account for the absorption of the generation beams as they pass through the sample (in the imaginary portion of the refractive index). Given that the broadband, white light field is resonant with electronic transitions for the molecule, its field strength is depleted as it passes through the sample to the buried interface. Thus, the generated ESFG signal from the buried interface should decrease as a function of film thickness due to the absorption of the white light field. Figure 3-2 also shows the models sensitivity to the differences in the molecular response. Changes to $\boldsymbol{\chi}_{\mathrm{Air}}^{(2)}$ and $\boldsymbol{\chi}_{\mathrm{Sub.}}^{(2)}$ lead to large changes for the calculated ESFG spectra, and due to the separation of the interference effects of the sample from the molecular response, we can use a sample's optical constants to calculate the interference of the ESFG signal as a function of thickness and turn the molecular response into a fitting parameter used to match the model to the experiment. In this way, we can separate the contributions to the ESFG signal from each interface.

In addition to changing the molecular response for our material for each interface, we can perform the same calculations for different polarization combinations. Figure 3-3 shows the same molecular response for A, B, and C as in Figure 3-2, but for the SSP polarization combination instead. By comparing Figure 3-3 and Figure 3-2 we see clear differences in the calculated spectra caused by changing the polarization combination calculated. This is due to changes in the Fresnel coefficients (Equations 3.9a – 3.9d) that depend on the polarization of the electric field. Changing the Fresnel coefficients in this

manner leads to changes in peaks and troughs of the oscillations of the ESFG signal as a function of film thickness as well as the strength of the ESFG signal measured.

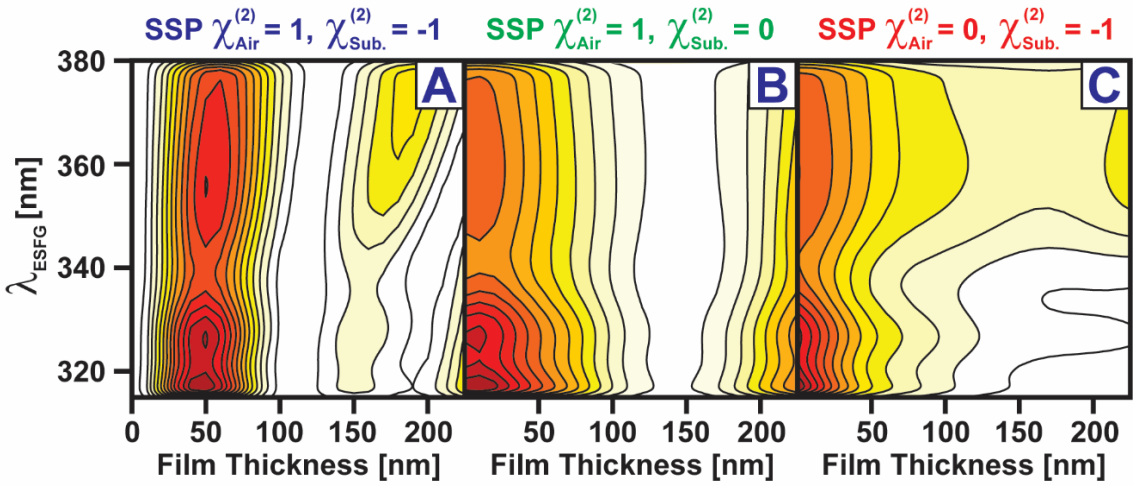


**Figure 3-3**: Model calculation of SSP polarization combination for ESFG spectra as a function of thickness (A) Calculation for $\boldsymbol{\chi}^{(2)}_{\text{Air}}$ = 1 and $\boldsymbol{\chi}^{(2)}_{\text{Sub.}}$ = -1 (B) Calculation for $\boldsymbol{\chi}^{(2)}_{\text{Air}}$ = 1 and $\boldsymbol{\chi}^{(2)}_{\text{Sub.}}$ = 0 (C) (B Calculation for $\boldsymbol{\chi}^{(2)}_{\text{Air}}$ = 0 and $\boldsymbol{\chi}^{(2)}_{\text{Sub.}}$ = -1

Looking at Figure 3-3A compared to Figure 3-2A, we see subtle shifts in the energy at which peaks occur at a film thickness of ~50 nm as well as altering the peak structure, especially around $\lambda_{ESFG}$ = 325 nm. Additionally, looking at a film thickness of 150 nm, we see that in Figure 3-3A we have a large reduction of signal strength as a function of energy, losing most of the ESFG signal intensity at $\lambda_{ESFG}$ = 325 nm and the shifting the low energy peak to $\lambda_{ESFG}$ = ~375 nm. These differences continue as we look at Figure 3-3B, where the valley in our ESFG intensity is much lower in SSP than in PPP, and in Figure 3-3C where the signal falls much more rapidly than it did for PPP.

As a final example of the capabilities of the interference modeling, we can also examine differences in the calculated ESFG spectra as a function collection method. In Figure 3-4A, we are showing the calculation of the PPP polarization combination for a

reflection method for collecting the ESFG signal (meaning that our detector is placed at a 90° angel relative to the incoming generation fields) versus the generated ESFG signal as a function of transmitting through the sample (Figure 3-4B). For this comparison, the molecular response is set such that $\boldsymbol{\chi}^{(2)}_{\text{Air}}$ is one and $\boldsymbol{\chi}^{(2)}_{\text{Sub.}}$ is negative one.

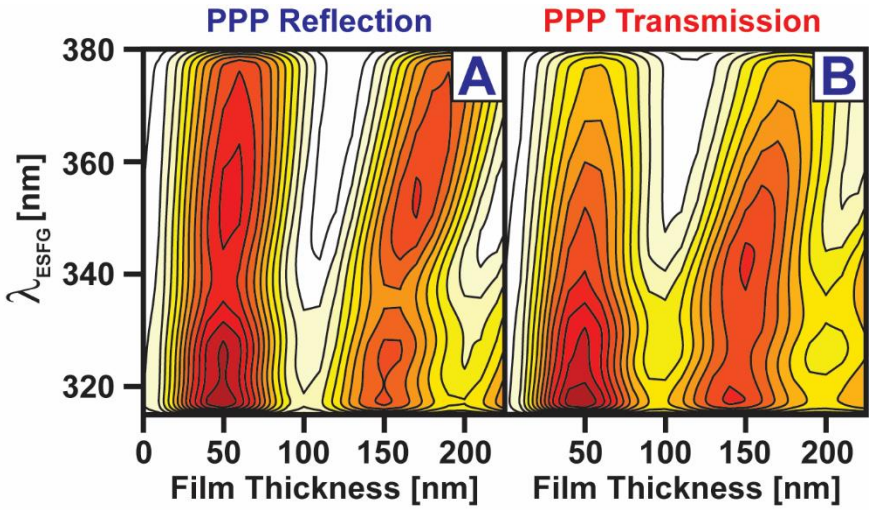


**Figure 3-4**: Model calculation of PPP polarization combination for ESFG spectra as a function of thickness (A) Reflection from the sample (B) Transmission through the sample

The first difference we see by changing the collection method is the peak structure as a function of energy. In the reflection collected calculation, we have a strong peak at $\lambda_{ESFG}$ = 325 nm and $\lambda_{ESFG}$ = 355 nm for a film thickness of 50 nm, but in the transmission collection we lose the well separated, strong peak at $\lambda_{ESFG}$ = 355 nm. Additionally, looking at the recurrence in the ESFG intensity as a function of thickness, the second thickness range with strong ESFG signal in the reflection collected calculation happens at ~150 nm, but this is clearly shifted for transmission down to ~145 nm. The low energy peak is also shifted in transmission to $\lambda_{ESFG}$ = 345 nm as opposed to $\lambda_{ESFG}$ = 355 nm for the reflection calculation. Taken together, Figures 3-3, 3-4, and 3-5 show that the ESFG interference

model that we have developed in Chapter 3 is highly sensitive to subtle shifts in molecular response for each interface, the polarization experiment performed, and the collection method, giving us a strong tool to determine the source of our ESFG signal from a given experiment. Here, we have also shown only a subset of the handles we can vary using our model to extract the molecular response from to ESFG active interfaces in our sample films.

### 3.4: Conclusions

Despite the great benefit ESFG provides in the study of electronic structure at interfaces, it can lead to complex spectra that are challenging to interpret. This is in part caused by the interference of signals that are generated at multiple ESFG active centers within a device, though this same difficulty can be leveraged to our advantage. In this Chapter we have shown that by measuring the ESFG signal from films of multiple different thicknesses our model can be used to extract the electronic structure of the desired interface. Through separation of the interference effects inherent to ESFG generation within a thin film sample from the molecular interaction with the generation fields. This allows us to float the molecular response as a fitting parameter to our ESFG data for each interface *individually*, giving us the ability to calculate the molecular response at each interface separately. This model has been extended and improved to be used with a new detection method of ESFG, heterodyne detected ESFG, which is discussed in detail in Chapter 7.

### 3.5: Chapter References


(1) Yamaguchi, S.; Tahara, T. Precise Electronic c(2) Spectra of Molecules Adsorbed at an Interface Measured by Multiplex Sum Frequency Generation. *J. Phys. Chem. B* **2004**, *108* (50), 19079–19082.

(2) Yamaguchi, S.; Tahara, T. Determining Electronic Spectra at Interfaces by Electronic Sum Frequency Generation: One- and Two-Photon Double Resonant Oxaxine 750 at the Air/Water Interface. *J. Chem. Phys.* **2006**, *125*, 194711–194711.

(3) Shen, Y. R. *The Principles of Nonlinear Optics*; Wiley-Interscience: New York, 1984.

(4) Shen, Y. R. Optical Second Harmonic Generation at Interfaces. *Annu Rev Phys Chem* **1989**, *40*, 327–327.

(5) O'Brien, D. B.; Massari, A. M. Simulated Vibrational Sum Frequency Generation from a Multilayer Thin Film System with Two Active Interfaces. *J. Chem. Phys.* **2013**, *138* (15), 154708–154708.

(6) O'Brien, D. B.; Massari, A. M. Modeling Multilayer Thin Film Interference Effects in Interface-Specific Coherent Nonlinear Optical Spectroscopies. *J. Opt. Soc. Am. B* **2013**, *30* (6), 1503–1503.

(7) O'Brien, D. B.; Massari, A. M. Experimental Evidence for an Optical Interference Model for Vibrational Sum Frequency Generation on Multilayer Organic Thin Film Systems I: Electric Dipole Approximation. *J. Chem. Phys.* **2015**, *142*, 024703–024703.

(8) O'Brien, D. B.; Massari, A. M. Experimental Evidence for an Optical Interference Model for Vibrational Sum Frequency Generation on Multilayer Organic Thin Film Systems II: Consideration for Higher Order Terms. *J. Chem. Phys.* **2015**, *142*, 024704–024704.

(9) Knittl, Z. *Optics of Thin Films*; John Wiley & Sons: London, 1976.

# Chapter 4: Development of an Electronic Sum Frequency Generation Spectrometer

## 4.1: Introduction

Sum frequency generation (SFG) has proven to be a powerful technique. Most often, SFG is performed with the resonant beam centered in the IR spectral range to perform vibrational SFG (VSFG). VSFG has been used to study the structure of water's surface[1,2] and has also been adopted to study thin films of organic molecules by looking at shifts in the frequency of common vibrational modes caused by changes in the local environment at an interface.[3–7] Comparatively, electronic SFG (ESFG) has experienced less use within the SFG community. While ESFG has been used, often for solution phase ESFG for water-air exposed interfaces[8–10] and in the solid state to determine molecular orientation of monolayers on glass substrates by heterodyne detected ESFG,[11] our group[12,13] is one of a few[11,14,15] serving as pioneers in the field of ESFG in the solid state due to the increased experimental complexity when moving to optically thick films studied by beams that span a broad spectral range in the visible region.

What then are the additional considerations that make working with visible beams more difficult? For one, the energy range required to cover the entirety of a vibrational transition is significantly smaller than that of an electronic transition. Additionally, to generate ESFG with a sufficiently strong signal, a fair amount of power is required within the visible field. Given that super-continuum generation is a weak, non-linear optical process, a very strong field is required for generation (our particular setup uses approximately 83 μJ of 804 nm light to generate about 13 μJ for the white light (WL) field, with 2 μJ used at the sample position). The beam's high energy requirements greatly restrict what medium you can use to generate your broadband field. Often for creating broadband visible beams, a crystal such as sapphire or $CaF_2$ is used, but these will burn at the energies

we require, so a water flow cell is used instead. Using water leads to a significant increase in the temporal dispersion of the generated field compared to that gained caused by generation in sapphire and $CaF_2$. ESFG can only be generated when both the WL and upconversion fields impinge on the sample simultaneously. The generation method described above produces a WL beam where the blue colors hit the sample approximately 1 ps after the red colors (this is due to the refractive index of glass, water, and air increasing as we move to bluer wavelengths and is called chirp). Therefore, to upconvert the entire electronic spectrum, either we need to scan the temporal delay of the upconversion beam across that of the WL field, or the upconversion beam must be broad enough in time to cover the chirp of the WL beam. The requirement to cover the temporal width of the WL then requires a stronger upconversion pulse, as ESFG signal scales with the peak intensity of the generation beams. This problem is easily avoided in VSFG as the refractive index across the IR is effectively flat (outside of $CO_2$ and water absorption in the air) within the limited bandwidth of VSFG experiments of ~ 200 $cm^{-1}$. For ESFG, our broadband field stretches across ~ 2000 $cm^{-1}$ in a region where the refractive index increases greatly as you move to higher energy.

Adopting ESFG to optically thick molecular thin films presents additional challenges. As the white light field is resonant with the sample, its amplitude is reduced by absorption of the system as it passes to the buried interface (Figure 4-1). Additionally, given that we upconvert from a resonance in the visible region, the measured ESFG spectra are produced in the UV, where optics for reflection or filtering a broad UV field are more expensive. Finally, as discussed in Chapter 3, measuring an optically thick film with multiple ESFG active interfaces is complicated by the fact that samples tend to be on the length scale of the wavelength for the generated ESFG, which leads to complications in determining contributions to the signal from the film interface of interest. All of this serves

to complicate the movement from VSFG to ESFG, especially on the thin film organic systems that will be discussed in later chapters. However, through careful planning, we can use ESFG to study these films and how their interfaces differ from their bulk.

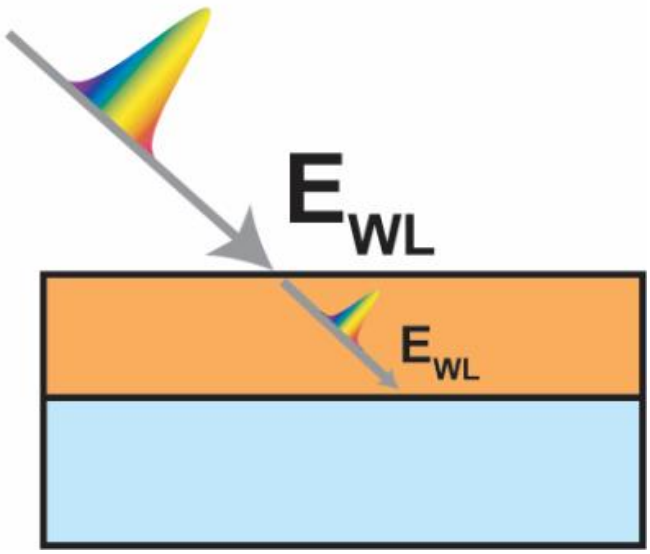


**Figure 4-1**: Cartoon showing depletion of the resonant white light field as it passes to the buried interface in the sample.

Below is a history of the ESFG spectrometer used for the measurements described in this thesis, with a brief description of additional experimental improvements made to the initial spectrometer design. The scientific implications for these improvements are largely reserved for discussion in the following Chapters. Chapter 5 uses the initial design described in Section 4.2, Chapter 6 uses the altered upconversion field described in Section 4.3, and Chapter 7 changes detection method as describe in Section 4.4.

### 4.2: Experimental design for direct detection of ESFG Spectra[2]

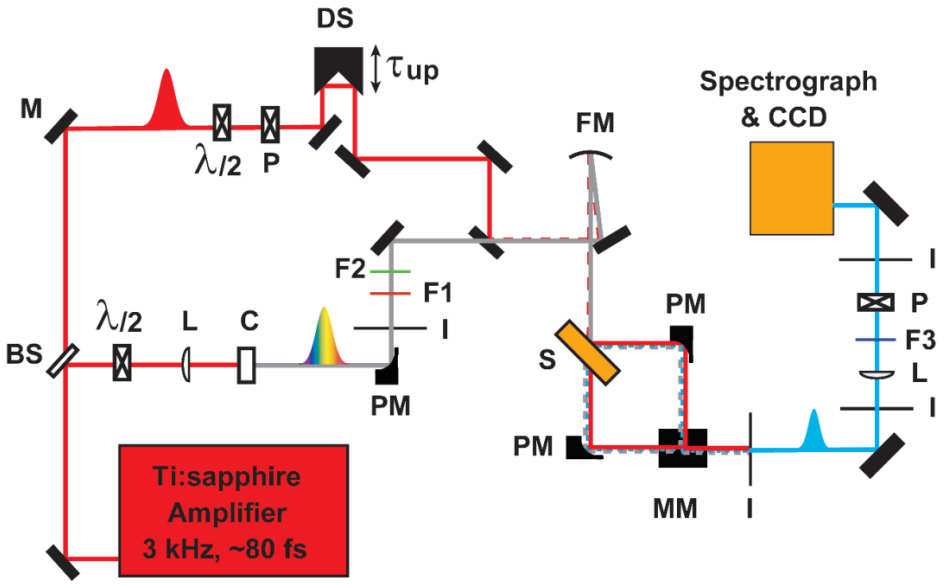


**Figure 4-2**: Schematic of ESFG spectrometer for direct ESFG measurements.

The experimental layout employed for direct ESFG is shown in Figure 4-2. In this detection regime, the signal generated from a sample is immediately imaged through the monochromator. A femtosecond Ti:sapphire regenerative amplifier (Coherent Legend Duo Elite, 3 kHz, 4.5 mJ) generates a 90 fs pulse centered at 804 nm with a bandwidth of 160 $cm^{-1}$ (FWHM). A small portion of the amplifier output (0.1 mJ) was focused into a 1 cm path length water flow cell (Starna Cells, 46-Q-10) to generate a white-light supercontinuum (WL) that was subsequently collimated with a 90° off-axis parabolic mirror (MPD129-G01, Thorlabs). The task of collimation is complicated by the strong chromatic aberration that is visible within the WL beam as the parabolic is moved through

[2] Previously published as Pandey, R.; Moon, A. P.; Bender, J. A.; Roberts, S. T. Extracting the Density of States of Copper Phthalocyanine at the $SiO_2$ Interface with Electronic Sum Frequency Generation. *J. Phys. Chem. Lett.* **2016**, *7*(6), 1060-1066. Supplementary Information. My contributions to this paper include helping make samples, helping collect ESFG spectra, building the ESFG spectrometer, creation of thin film modeling software, modeling and fitting ESFG spectra, and interpreting the spectra and writing the paper with my colleagues.

its focus, however we stress again the importance of proper collimation at this step as it affects the ability to deconvolve the spectrum of the WL beam from the detected ESFG spectrum. The WL beam generated in this fashion extends spectrally from ~ 350 nm to greater than ~750 nm (the cutoff for the spectrometer), centered around the fundamental frequency for generation of 804 nm. Following its collimation ahead of the sample, the WL was passed through a pair of glass filters (FGL455 and FGS900-A, Thorlabs) to remove the residual 800 nm driving field and limit spectral overlap between the blue edge of the WL and the red edge of the emitted ESFG signal field, which aids separation of ESFG from scattered white light. The transmitted portion of the WL (450 nm – 750 nm) spectrally overlaps with transitions of the systems of interest and thus is likely to be resonant with interfacial electronic transitions, allowing it to enhance specific frequency components of the ESFG signal. A second portion of the amplifier output was used as the narrowband upconversion pulse. Typical pulse energies for the filtered WL and up-conversion pulses were ~2 μJ and 1 μJ, respectively. Care must be taken to ensure no damage occurs to the films of interest, as this can lead to changes in the measured ESFG spectra (Figure 4-3).

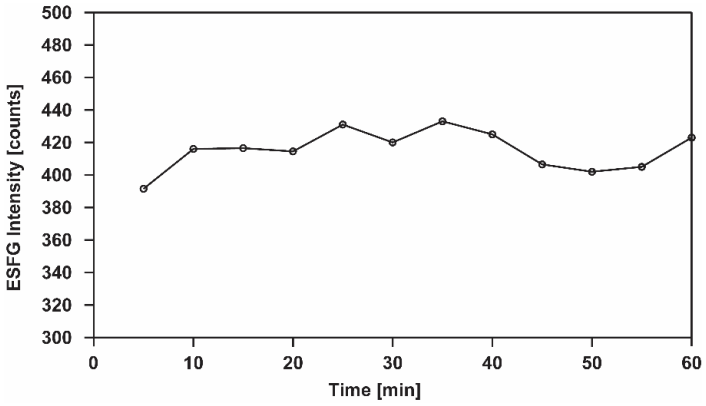


**Figure 4-3**: ESFG signal intensity as a function of exposure time for a 50 nm CuPc film.

The upconversion and WL fields were focused onto the sample using a 15 cm focal length concave mirror in a noncollinear geometry, causing ESFG to be emitted in both the forward (transmitted) and reverse (reflected) directions. While we have recorded spectra using both collection geometries, within this thesis we limit our discussion to ESFG spectra measured using a reflection geometry. We define the *z*-axis to be the direction normal to the sample plane and the ESFG signal is taken to be emitted within the *zx* plane. Spectra were measured using an angle of incidence of $\theta = 45^{o}$ with respect to the sample surface normal for both the WL and upconversion fields (Figure 4-4).

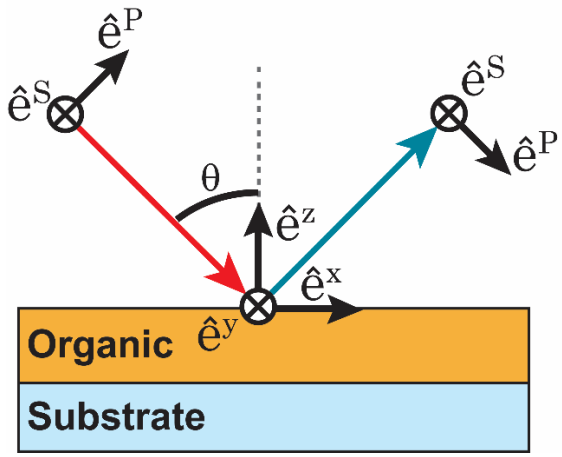


**Figure 4-4:** Beam orientation at the sample for ESFG experiments

Both of the excitation fields were tilted slightly out of the zx-plane of incidence ($\pm 2.5^{o}$-$5^{o}$) which allowed spatial separation of the ESFG signal from the driving fields. Following the sample, the ESFG signal was collected and collimated with a 90° off axis parabolic mirror (50331AL, Newport) and passed through irises and a spectral filter (UG11, SCHOTT) to remove scattered WL. A 50 cm lens focused the ESFG field onto the entrance slit of a spectrometer (Acton Spectra Pro SP-2500) where a 300 grove/mm grating

blazed at 300 nm spectrally dispersed the signal onto a 512 × 2048 pixel liquid nitrogen-cooled CCD (PyLoN, Princeton instruments).

In all ESFG measurements, the polarizations of the WL, upconversion beam, and emitted ESFG were selected using polarization optics shown in Figure 4-2. Although the convention in naming the polarization condition used in a second-order nonlinear experiment is to list the polarization of each incoming/outgoing wave in descending energy order, we choose to break that convention here and instead list our fields in the order ESFG/upconversion/WL. Thus, in our notation a "SSP" measurement corresponds to the detection of the S-polarized component of the ESFG field generated by a S-polarized upconversion field and P-polarized WL. This choice allows us to draw analogies to vibrational SFG spectra wherein the final named interaction is one that is resonant with the sample.

Due to chirp in the WL pulse, ESFG spectral acquisition requires scanning the time delay between the WL and upconversion fields using a computer-controlled delay stage (Newport XMS50) to fully measure a sample's second order response (Figure 4-5B). The top axis of this figure represents the wavelength of the emitted ESFG signal ($\lambda_{ESFG}$) while the bottom denotes the component of the WL ($\lambda_{WL}$) that drives emission at $\omega_{ESFG} = \omega_{WL} + \omega_{UP}$. Each ESFG spectrum plotted in Chapters 5 and 7 represent the sum of a set of measurements wherein the time delay between the WL and upconversion fields was scanned. The spectrum acquired at each step was averaged for a 400 second exposure time. Figure 4-3A displays the ESFG spectrum of z-cut quartz measured in this manner. As quartz contains no resonant transitions in the visible range, this spectrum is purely non-resonant and indicates the spectral instrument response function of our ESFG spectrometer, which spans $\lambda_{WL}$ ~ 450 – 750 nm. To deconvolute the instrument response from our measured spectra and account for day-to-day fluctuations in laser power, each ESFG

spectrum that we include in this report has been normalized using a reference spectrum obtained for z-cut quartz at PPP polarization taken on the same day.

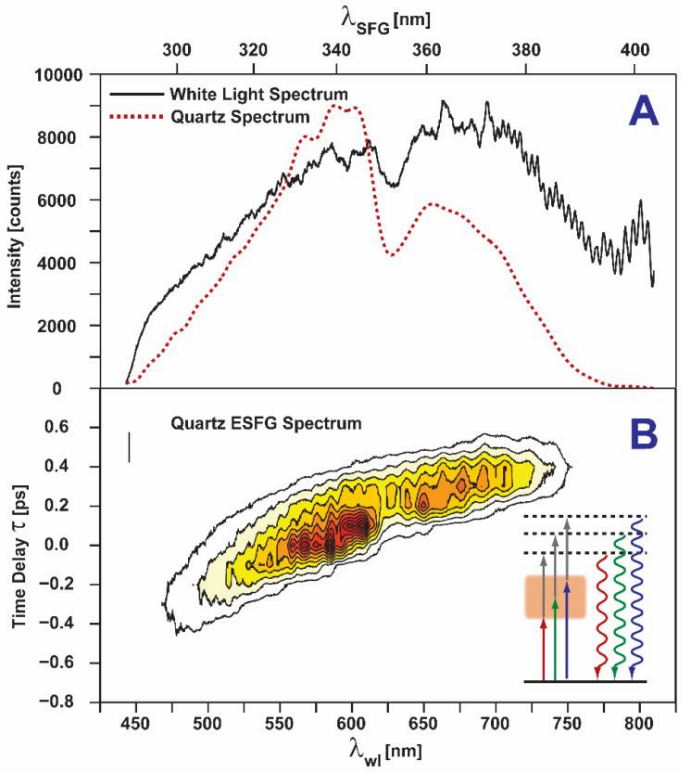


**Figure 4-5**: (A) Representative spectra of the filtered WL spectrum compared vs. collected ESFG for z-cut quartz (B) ESFG spectrum of z-cut quartz as a function of time delay between WL and upconversion beams

### 4.3: Changing the wavelength of the upconversion beam

To improve direct detected ESFG an adjustment in the upconversion field used for ESFG generation was made (Figure 4-6). We follow the same detection method for direct detected ESFG, but instead of using the 804 nm beam directly from the Ti:sapphire amplifier, we pass a portion of this fundamental field (approximately 1.5 mJ) into a picosecond optical parametric amplifier (TOPAS 400, LightConversion). The OPA takes the femtosecond 804 nm field from the regenerative amplifier and converts it to a 3 ps

beam tunable across the visible and near IR. By changing to a beam with a 3 ps pulse width, we can upconvert across the entire WL spectrum at a single time delay instead of having to scan across the temporal dispersion inherent to the WL generation process (Figure 4-6A).

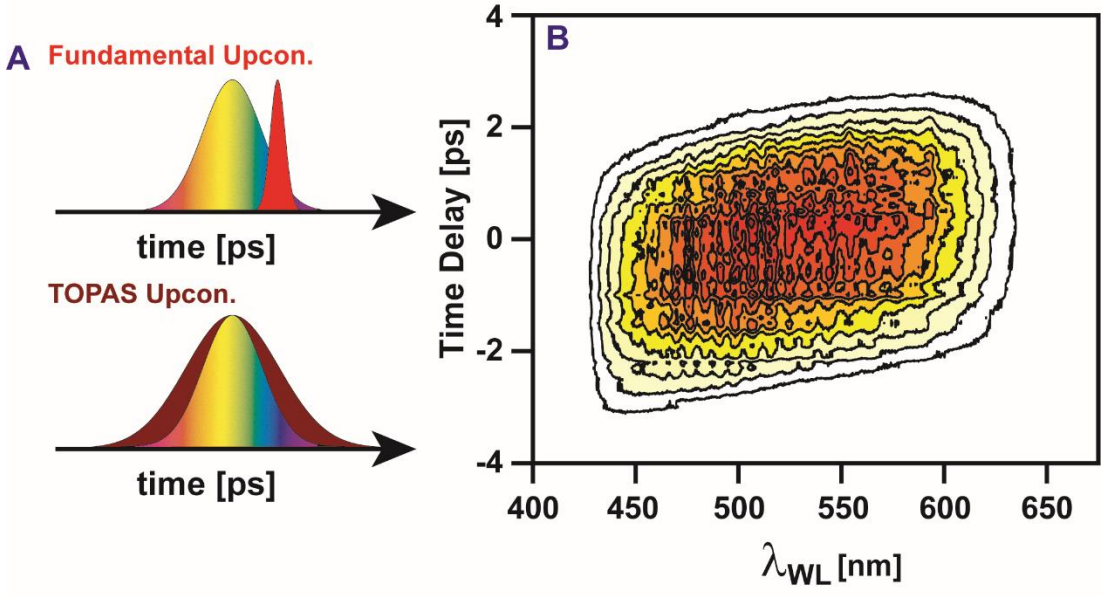


**Figure 4-6**: (A) Cartoon of temporal width for white light vs. fundamental and TOPAS (B) ESFG intensity of quartz LO as a function of time delay between TOPAS and WL fields.

Figure 4-6B shows the intensity of the ESFG field as a function of the time delay between the TOPAS and WL beams. While there is the same growth of different colors as a function of time delay as seen in figure 4-5A (where upconversion was performed with the fundamental beam), there is a clear section where it is possible to upconvert all of the colors within the WL spectrum at a single time delay. This ability removes the need to scan the time delay between the two generation beams, instead being able to upconvert the whole white light field in a single spectrum. It should be noted, however, that as ESFG is a second-order, non-linear spectroscopic technique, high peak intensity is required to

generate a signal from our samples that is strong enough to record above detector noise. This means that with the increase in the upconversion beam's temporal width when switching to the TOPAS for upconversion requires a greater overall field intensity. By comparison of long-term damage measurements performed on organic films we find that field energy of just under 10 μJ generates sufficient signal without damaging our samples. Similar to the previous section, an in-depth discussion of these experiments is reserved for Chapter 6.

In addition to reducing the time required for a complete ESFG spectrum, using an OPA for our upconversion field allows us move away from multiphoton resonance effects within our ESFG generation. The analysis of our ESFG spectra in Chapters 5-7 are performed with the assumption that our white light field is the only beam that is resonant with the electronic states of our sample. If this assumption is true, when we change the energy of our upconversion field our ESFG spectra should shift in energy on the ESFG axis, but should remain invariant as a function of the upconversion beam energy on the one-photon white light axis. Figure 4-7 plots the ESFG spectra collect for a 51 nm N−N′-dimethyl-3,4,9,10-perylenedicarboximide (C1-PDI) thin film on an $SiO_2$ substrate as a function of the upconversion energy after subtraction to the one-photon axis. Here, the blue spectrum (804 nm) is generated using the fundamental beam from the amplifier, and the light blue (885 nm), green (981 nm), and red (1028 nm) fields are made by tuning the TOPAS to the indicated wavelength for ESFG generation. Comparing the two generation schemes, we see that while the spectra collected using the TOPAS do still shift on the one-photon axis as a function of upconversion wavelength (shifting to higher energy as the wavelength is moved to lower energy by ~ 20nm) the shift is significantly less than that seen with when comparing the TOPAS upconversion to that of 804 nm with the fundamental. This is likely due to additional resonance conditions when the upconversion

beam is higher in energy, which can greatly complicate the interpretation of the ESFG spectrum.

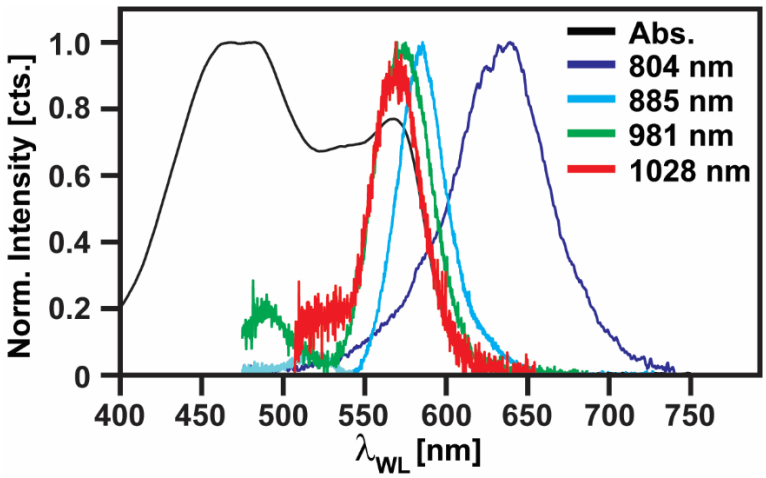


**Figure 4-7**: Comparison of the PPP ESFG spectra for a 51 nm C1-PDI thin film as a function of upconversion wavelength. Spectra are plotted versus the white light axis (after subtraction of the upconversion energy from the ESFG spectra).

As an example, the linear absorption of the 51 nm C1-PDI film is plotted with the ESFG spectra in Figure 4-7 (black trace). While spectra generated when the TOPAS is used for upconversion don't perfectly overlap with the electronic absorption spectrum, they overlap with it (and each other) much more closely than that of the 804 nm upconversion. In addition, the comparatively subtle shifts seen using the TOPAS could be explained by shifts in thin film interference and Fresnel coefficients as discussed in Chapter 3, but this difference is too great for the 804 nm. Thus, by switching to the TOPAS for upconversion, we gain tunability in the energy used for the upconversion field, and gain the ability to move away from multiphoton resonance effects.

### 4.4: Brief overview of design for Heterodyne detection scheme[3]

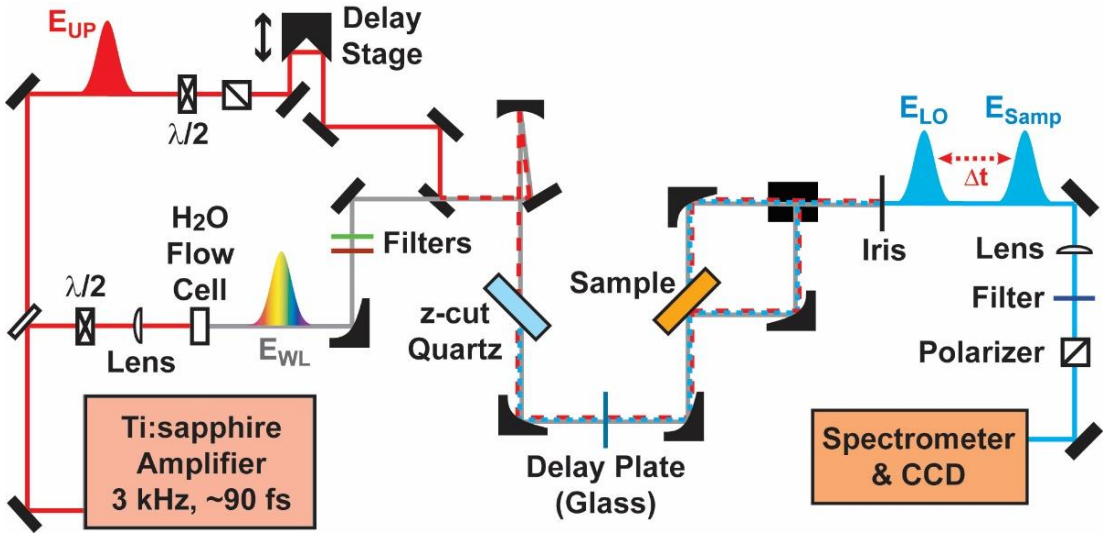


**Figure 4-8:** Schematic showing the experimental layout used for HD-ESFG measurements.

Figure 4-8 shows a schematic of the experimental layout employed for heterodyne-detected electronic sum frequency generation (HD-ESFG) measurements. Here, the significant difference from direct detected ESFG is the inclusion of a z-cut quartz piece in the beam path before the generation fields interact with the sample. Specifically, the beams are generated and focused in the same manner as the direct ESFG experiment, but then focused onto a 20 μm thick z-cut quartz piece (referred to as the local oscillator or LO), which generates a broadband, non-resonant ESFG signal within the material ahead of the sample. The z-cut quartz piece is non-centrosymmetric and therefore gives a strong, bulk allowed ESFG response. By generating a strong ESFG field ahead of the sample, we can

[3] Previously published as Moon, A. P.; Pandey, R.; Bender, J. A.; Cotton, D. E.; Renard, B. A.; Roberts, S. T. Using Heterodyne-Detected Electronic Sum Frequency Generation to Probe the Electronic Structure of Buried Interfaces. *J. Phys. Chem. C* **2017**, *121*(34), 18653-18664. My contributions to this paper include helping collect ESFG spectra, building the ESFG spectrometer, creation of initial thin film modeling software, consultation of modeling and fitting ESFG spectra, and interpreting the spectra and writing the paper with my colleagues.

interfere the signal from the sample against that of the LO to greatly improve detection efficiency of the spectrometer. Following generation of the LO ESFG field, all three beams are collimated by a 90$^{o}$ off-axis parabolic mirror. The next large change in the experimental design comes in the form of the 145 μm glass delay plate placed exclusively in the path traveled by the LO signal before all three beams are refocused onto the sample by a second parabolic mirror. This piece of glass introduces a temporal delay in the ESFG signal from the LO relative to the two generation fields, and therefore the ESFG from the sample. After signal generation from the sample, the beams are then collimated as in a direct ESFG measurement scheme before being focused onto a spectrometer/CCD camera. The existence of two ESFG signals that are temporally separated causes an interference pattern to appear in the measured ESFG field at the CCD camera, and is the basis for the heterodyne ESFG (HD ESFG) detection scheme (Figure 4-5A). It is important to note that you need to carefully choose the delay plate thickness, as too little or too great of a temporal walk off between the LO and the generation fields will lead to a lack of interference.

While the full discussion for this experiment and its results will be left for Chapter 7 of this thesis, Figures 4-9A and B briefly show the advantage of these changes to the direct ESFG spectrometer. In Figure 4-9A we see the interference pattern created when from the 20 μm quartz LO with that of the signal from a 54 nm C1-PDI thin film on fused quartz. Here, the primary peaks are from the strong, bulk allowed non-resonant response of the LO, while the interference fringes on top of these peaks contain the desired information for the sample film. These contributions can be separated by using a fast Fourier transform (FFT), and the signal from the film can be isolated by normalization of HD-ESFG signal from a piece of quartz at the sample position. The upper half of Figure 4-9B shows the comparison in signal-to-noise ratio for the extracted sample-LO ESFG signal relative to that of the direct measurement for a C1-PDI film. We can see that there is a

marked improvement in this signal-to-noise ratio, especially when it is noted that both signals are collected for the same length of time. The lower half of 4-9B shows it is possible to extract signal that depends exclusively on the sample, and that while the noise is greatly reduced in the HD-ESFG measurement, the location of the detected signal and general shape are the same. Differences in these two spectra are again left for discussion in a later Chapter.

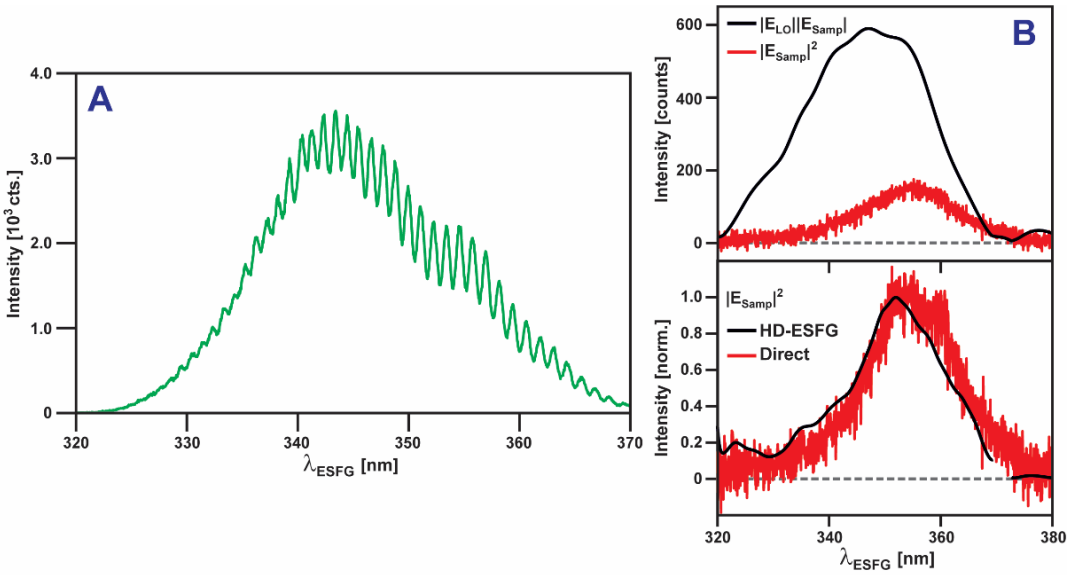


**Figure 4-9**: (A) Example HD ESFG spectra for 20 μm quartz LO and 54 nm C1-PDI thin film (B) Example of signal to noise improvement for detection of C1-PDI film between direct and HD ESFG measurements

### 4.5: Summary

In this Chapter, we have described the challenges of creating an ESFG spectrometer. We started with the description of the initial direct detected ESFG spectrometer used in Chapter 5 and changing the upconversion field from using the fundamental beam to generation by an OPA for Chapter 6. Finally, we developed HD-ESFG for improvement to signal-to-noise ratio for Chapter 7.

## 4.6: Chapter References


(1) Inoue, K.; Ishiyama, T.; Nihonyanagi, S.; Yamaguchi, S.; Morita, A.; Tahara, T. Efficient Spectral Diffusion at the Air/Water Interface Revealed by Femtosecond Time-Resolved Heterodyne-Detected Vibrational Sum Frequency Generation Spectroscopy. *J Phys Chem Lett* **2016**, *7*, 1811.

(2) Wang, J.; Chen, X.; Clarke, M. L.; Chen, Z. Detection of Chiral Sum Frequency Generation Vibrational Spectra of Proteins and Peptides at Interfaces in Situ. *PNAS* **2005**, *102* (14), 4978–4983.

(3) O'Brien, D. B.; Massari, A. M. Experimental Evidence for an Optical Interference Model for Vibrational Sum Frequency Generation on Multilayer Organic Thin Film Systems I: Electric Dipole Approximation. *J. Chem. Phys.* **2015**, *142*, 024703–024703.

(4) O'Brien, D. B.; Massari, A. M. Experimental Evidence for an Optical Interference Model for Vibrational Sum Frequency Generation on Multilayer Organic Thin Film Systems II: Consideration for Higher Order Terms. *J. Chem. Phys.* **2015**, *142*, 024704–024704.

(5) O'Brien, D. B.; Massari, A. M. Simulated Vibrational Sum Frequency Generation from a Multilayer Thin Film System with Two Active Interfaces. *J. Chem. Phys.* **2013**, *138* (15), 154708–154708.

(6) Vanselous, H.; Petersen, P. B. Extending the Capabilities of Heterdoyne-Detected Sum-Frequency Generatino Spectroscopy: Probing Any Interface in Any Polarization Combination. *J. Phys. Chem. C* **2016**, *120* (15), 8175–8184.

(7) Li Fu, S.-L. C.; Wang, H.-F. Validation of Spectra and Phase in Sub-1 Cm-1 Resolution Sum-Frequency Generatino Vibrational Spectroscopy through Internal Heterodyne PHase-Resolved Measurement. *J. Phys. Chem. B* **2016**, *120* (8), 1579–1589.

(8) Mondal, S. K.; Yamaguchi, S.; Tahara, T. Molecules at the Air/Water Interface Experience a More Inhomogeneous Solvation Environment than in Bulk Solvents: A Quantitative Band Shape Analysis of Interfacial Electronic Spectra Obtained by HD-ESFG. *J. Phys. Chem. C* **2011**, *115* (7), 3083–3089.

(9) Yamaguchi, S.; Bhattacharyya, K.; Tahara, T. Acid-Base Equilibrium at an Aqueous Interface: PH Spectrometry by Heterodyne-Detected Electronic Sum Frequency Generation. *J Phys Chem C* **2011**, *115*, 4168.

(10) Yamaguchi, S.; Tahara, T. Precise Electronic c(2) Spectra of Molecules Adsorbed at an Interface Measured by Multiplex Sum Frequency Generation. *J. Phys. Chem. B* **2004**, *108* (50), 19079–19082.

(11) Yamaguchi, S.; Tahara, T. Heterodyne-Detected Electronic Sum Frequency Generation: “Up” versus “down” Alignment of Interfacial Molecules. *J. Chem. Phys.* **2008**, *129*, 101102–101102.

(12) Pandey, R.; Moon, A. P.; Bender, J. A.; Roberts, S. T. Extracting the Density of States of Copper Phthalocyanine at the SiO2 Interface with Electronic Sum Frequency Generation. *J. Phys. Chem. Lett.* **2016**, *7* (6), 1060–1066.

(13) Moon, A. P.; Pandey, R.; Bender, J. A.; Cotton, D. E.; Renard, B. A.; Roberts, S. T. Using Heterodyne-Detected Electronic Sum Frequency Generation to Probe the Electronic Structure of Buried Interfaces. *J Phys Chem C* **2017**, *121* (34), 18653–18664.

(14) Li, Y.; Wang, J.; Xiong, W. Probing Electronic Structures of Organic Semiconductors at Buried Interfaces by Electronic Sum Frequency Generation Spectroscopy. *J. Phys. Chem. C* **2015**, *119* (50), 28083–28089.

(15) Wilcox, D. E.; Sykes, M. E.; Niedringhaus, A.; Shtein, M.; Ogilvie, J. P. Heterodyne-Detected and Ultrafast Time-Resolved Second-Harmonic Generation for Sensitive Measurements of Charge Transfer. *Opt. Lett.* **2014**, *39* (14), 4274–4274.

# Chapter 5: Extracting the Density of States of Copper Phthalocyanine Using Electronic Sum Frequency Generation[4]

## 5.1: Introduction

In previous Chapters we have established the need for an interfacial specific spectroscopy that reports on the density of states for organic semiconductors (OSC's) at buried interfaces. With a theoretical understanding of electronic sum frequency generation (ESFG), we can consider its application to a known OSC to determine the information we can gain through our interface specificity. The ability ESFG will give to compare the energetic states for a molecule in its bulk relative to that at the interface will provide new insights into the changes we see for a system put into a new environment, and can be applied to improving the function and capability of nanostructured semiconductors. To begin, we need a well-known OSC system that can be used to study the strength of ESFG applied to these systems. We have chosen copper phthalocyanine (CuPc) thin films grown on $SiO_2$ substrates by thermal evaporation. CuPc was one of the first OSCs used as an electron donor in organic photovoltaic cells[1] and is noted both for its long-lasting photostability and high extinction at the red-edge of the visible spectrum.[2] When thermally deposited, CuPc forms crystallites that pack in centrosymmetric slip-stacked arrangements.[3–5] Therefore, no dipolar ESFG signal is expected from the bulk of a CuPc film, allowing ESFG measurements to report on distortions of the electronic density of states of interfacial CuPc molecules.

In this Chapter, we present ESFG spectra of CuPc thin films prepared by thermal deposition on $SiO_2$. Features that appear in these spectra are similar to those in a linear

[4] Previously published as Pandey, R.; Moon, A. P.; Bender, J. A.; Roberts, S. T. Extracting the Density of States of Copper Phthalocyanine at the $SiO_2$ Interface with Electronic Sum Frequency Generation. *J. Phys. Chem. Lett.* **2016**, *7*(6), 1060-1066. My contributions to this paper include helping make samples, helping collect ESFG spectra, building the ESFG spectrometer, creation of thin film modeling software, modeling and fitting ESFG spectra, and interpreting the spectra and writing the paper with my colleagues.

absorption spectrum but are shifted in energy, which implies changes in the electronic structure of these films at the $SiO_2$ interface relative to their bulk. In addition, ESFG line shapes are found to be strongly dependent on film thickness. Prior studies of CuPc films using a related even-order nonlinear spectroscopy, second harmonic generation (SHG), observed a similar dependence of the SHG signal on film thickness.[6–11] While these studies attributed this result to electric quadrupolar coupling of the SHG fields to the bulk of their sample films, a process permitted in centrosymmetric media,[12–14] these studies neglected to consider that optically thin CuPc films necessarily have two SHG active surfaces. As such, fields emitted by both surfaces will interfere with one another and could explain the experimentally observed thickness trend. Indeed, we find that by applying a thin film interference model,[15–18] we are able to largely reproduce the changes observed in ESFG spectra with film thickness. This model also allows us to separate the second-order nonlinear susceptibility, $\chi^{(2)}$, associated with both the CuPc:$SiO_2$ and CuPc:Air interfaces. Such information reports on the electronic structure and organization of molecules at these interfaces. This work demonstrates that ESFG is an effective tool that can noninvasively probe the interfacial density of states of thin film electronics and provide information critical to their optimization.

### 5.2: Characterization

Figure 5-1B plots the linear absorption spectrum of a 50 nm thick CuPc film in the region about its Q-band. For monomeric phthalocyanines in solution, the Q-band corresponds to a doubly degenerate $\pi$-to-$\pi^*$ HOMO-to-LUMO transition with dipole moments polarized along perpendicular directions within CuPc's molecular plane.[19,20] Due to intermolecular excitonic coupling in the solid state, the Q-band splits into two prominent transitions in thin films, one centered at 695 nm and another at 615 nm.[21,22] For simplicity,

we denote these bands $Q_A$ and $Q_B$, respectively. we also observe a weak transition that broadens the high-energy side of the Q-band near 575 nm. While spectra of isolated phthalocyanines display a weak absorption in this region that has been assigned to both an n-to-π* transition[19,23,24] and a vibronically allowed $b_{1g} \rightarrow e_g$ transition,[25] a more likely explanation for this band in the solid state is coupling of intermolecular charge transfer states to the Frenkel excitonic states that comprise the Q-band.[26] This assignment is supported by electro-absorption[26–28] and electron energy-loss spectra[29] that have each shown the resonances comprising the Q-band contain charge transfer character, particularly on its high energy side.[26,27] As such, we label this band $Q_{CT}$.

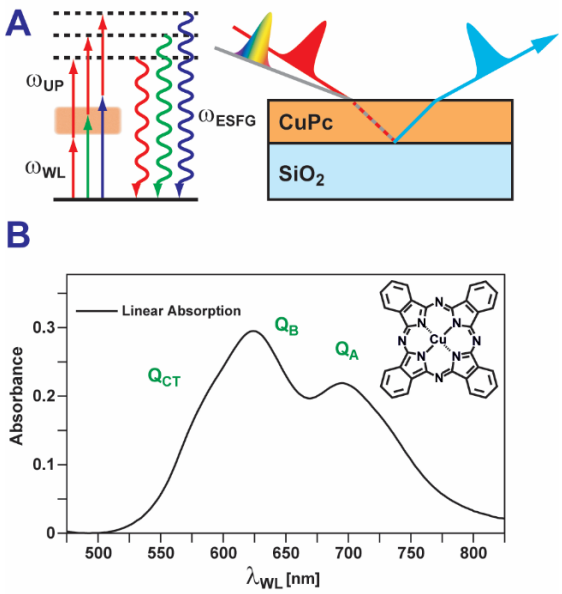


**Figure 5-1**: (A) Example ESFG energy level scheme with experimental geometry used in this Chapter (B) Absorption spectrum for a 50 nm CuPc film on $SiO_2$ substrate.

CuPc was obtained from Sigma-Aldrich and used as received to prepare thin films. Prior to deposition, $SiO_2$ substrates (Borosilicate Glass, Fisherbrand, thickness = 140 μm) were carefully cleaned by washing first with detergent, followed by deionized water,

methanol, and finally dried with flowing $N_2$ gas. All CuPc films were prepared at room temperature using a thermal evaporator (Amod, Angstrom Engineering) at pressures of $10^{-6}$-$10^{-7}$ Torr with a deposition rate of 1 Å/sec. Film thicknesses were determined via spectroscopic ellipsometry (M-2000, J. A. Woollam) performed by scanning the incidence angle from 40-55° in 5º steps and fitting data recorded outside of the CuPc absorption region (900 – 1000 nm) using a Cauchy model. Absorption spectra of CuPc films were recorded using a UV-Vis spectrometer with an integrating sphere attachment (Shimadzu UV-2600). Absorption spectra for all investigated CuPc films appear in Figure 5-2 A and scale linearly in amplitude with film thickness.

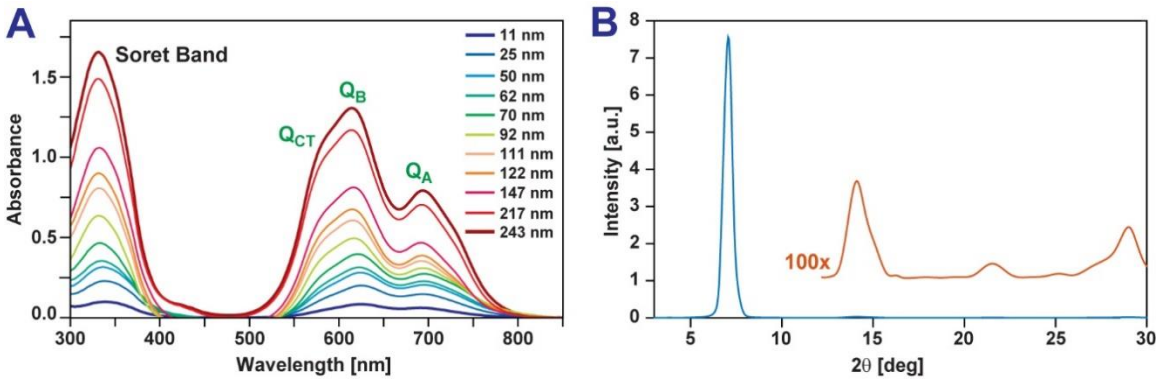


**Figure 5-2**: (A) Linear absorption spectra of thermally evaporated CuPc films as a function of film thickness. (B) GIXRD pattern of a 149 nm thick CuPc film.

Prior studies that have prepared thermally deposited CuPc films at room temperature have observed they tend to form polycrystalline grains that adopt a centrosymmetric brickstone structure referred to as CuPc's α-phase.[3–5] Additionally, CuPc films deposited on weakly interacting substrates such as $SiO_2$ are found to preferentially align with their molecular planes tilted normal to the substrate surface as this maximizes van der Waals interactions among CuPc molecules.[30–32] Thermal annealing of these films can cause them to form CuPc's more stable herringbone polymorph (β-phase)[33] which is

also centrosymmetric.[34] Our data display an intense peak near 2θ = 7.05º that has been assigned to the (200) Bragg diffraction plane from CuPc's α-phase and is indicative of grains containing CuPc molecules tilted perpendicular to the substrate surface (Figure 5-2B).[30,31,35] In addition to higher order diffraction peaks associated with this feature at 2θ = 14.1º and ~21º, we observe a weak clustering of peaks near 2θ = 27.8º that are characteristic of CuPc molecules lying flat along a surface.[31,35] These features are consistent with both polymorphs, suggesting that our films may contain a mixture of α- and β-phase crystallites. However, the relatively small amplitude of this feature allows us to conclude the majority of crystallites that comprise our films orient in an edge-on manner.

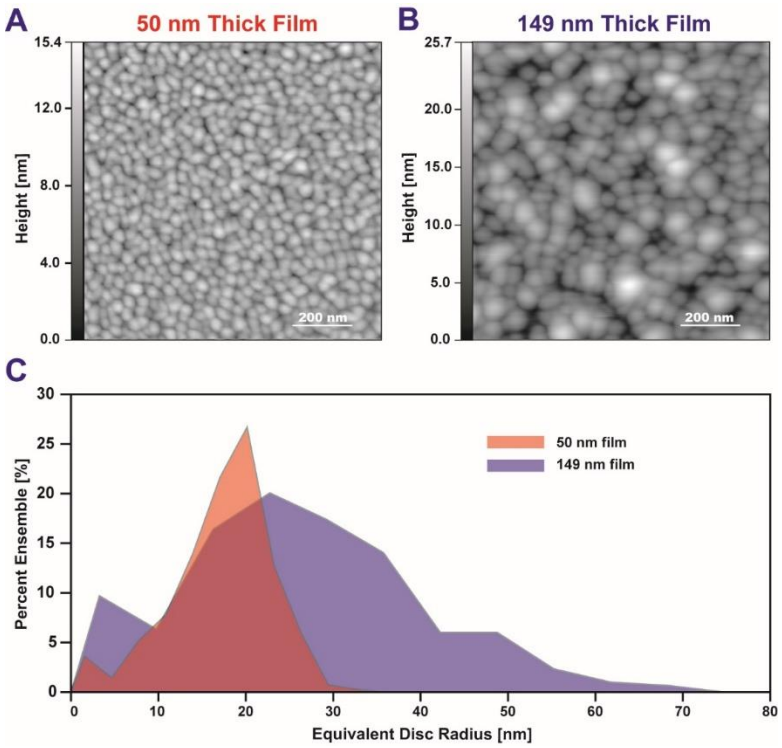


**Figure 5-3**: (A and B) AFM images of 50 nm and 149 nm thick CuPc films. (C) Grain size distributions extracted from these images.

AFM images of our CuPc films, collected in tapping mode, are consistent with the formation of polycrystalline grains with an average diameter of 40 nm (Figure 5-3). However, despite being polycrystalline, these films are smooth, possessing an RMS surface roughness of 2 – 4 nm depending on film thickness.

### 5.3: ESFG Spectra of CuPc Films

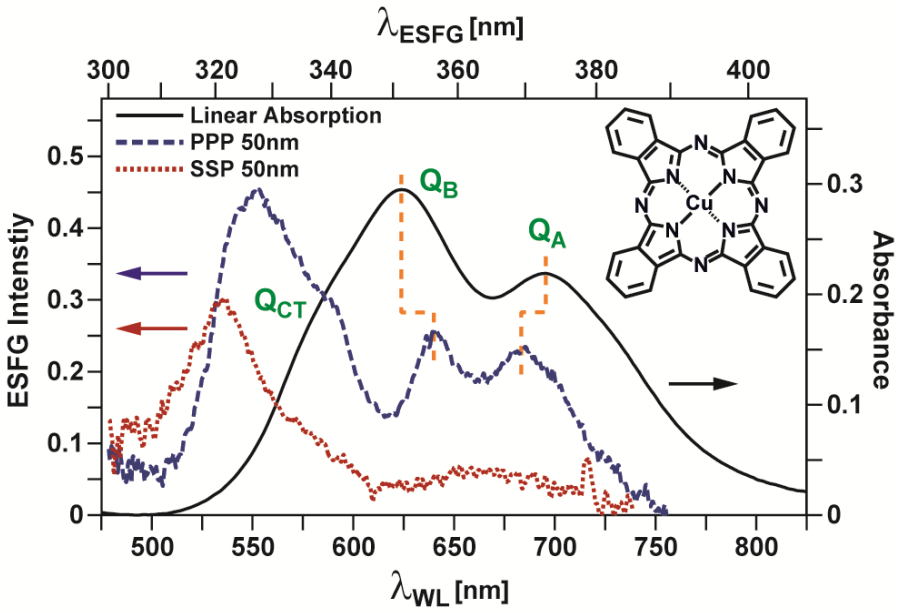


**Figure 5-4**: Comparison of electronic absorption spectrum of a 50 nm CuPc film to PPP and SSP ESFG spectra measured for the same film in a reflection geometry.

Plotted alongside the linear absorption spectrum in Figure 5-4 are ESFG spectra of our CuPc sample film collected for both PPP and SSP polarization conditions. Details regarding our ESFG spectrometer and the preparation of CuPc sample films are given previously in Chapter 4. In the PPP spectrum, we observe two prominent peaks at $\lambda_{WL}$ = 682 nm and 642 nm as well as a broad feature near 565 nm that appears to be comprised of multiple peaks. Focusing first on the two lower energy peaks, we find that they resemble the two excitonically split resonances $Q_A$ and $Q_B$ in CuPc's linear absorption spectrum but

are spectrally shifted. In particular, these resonances decrease their peak spacing from 0.23 eV in the linear absorption spectrum to 0.12 eV in the PPP spectrum, suggesting that excitonic coupling is reduced among interfacial CuPc molecules relative to those in the film's bulk. Studies of the growth mechanism of CuPc films on $SiO_2$ have shown the initial monolayer grows by nucleating one-dimensional slip-stacked arrangements of molecules whose growth axis lies along the substrate plane.[36] Simultaneous nucleation of multiple crystallites during film growth could lead to preferential formation of small grains and defects with excitonic structures that strongly differ from CuPc's bulk. Alternatively, the peak shifts we observe may result from electrostatic interactions between CuPc molecules and the $SiO_2$ surface.[37] Indeed, prior studies have suggested such interactions can distort CuPc's molecular symmetry and perturb its interfacial density of states with respect to the bulk.[38] Examining the ESFG spectrum measured for SSP polarization conditions, we find the prominent $Q_A$ and $Q_B$ features that appear in the PPP spectrum are strongly suppressed.

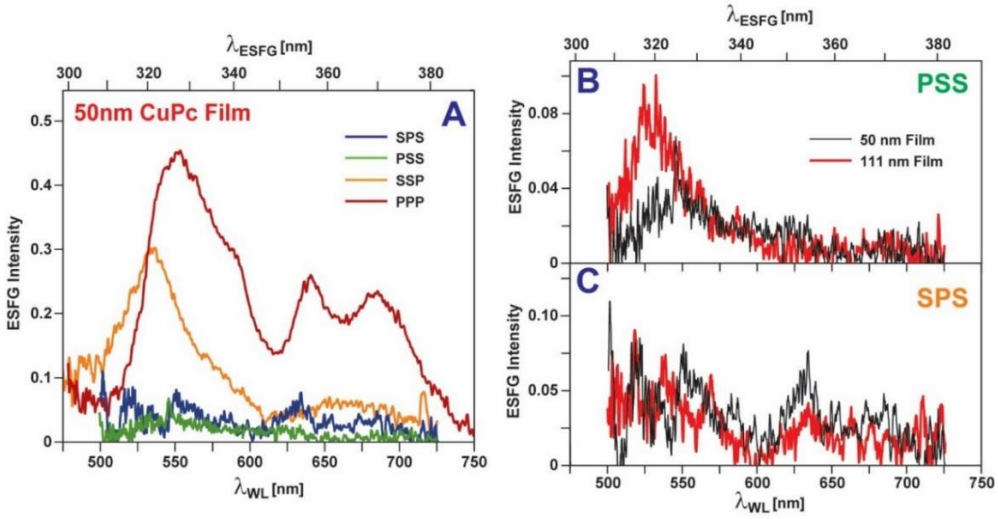


**Figure 5-5**: (A) ESFG spectra 50 nm CuPc on $SiO_2$ measured for SPS, PSS, SSP, and PPP polarizations. (B and C) PSS and SPS spectra of a 50 nm (black) and 111 nm thick (red) CuPc film.

We have also measured spectra for PSS and SPS polarization conditions (Figure 5-5) and found that the $Q_A$ and $Q_B$ peaks are absent in these spectra. In Figure 5-6, we show the frame of reference used for our ESFG spectrometer as it relates the sample frame of x, y, and z to the lab frame in polarizations. The +z direction is defined as the normal direction pointing away from the CuPc surface and the emitted ESFG field lies in the xz-plane. Given this frame of reference, PSS and SPS spectra respectively probe the $\chi_{zyy}$ and $\chi_{yzy}$ components of the second order nonlinear susceptibility, $\chi^{(2)}$, and report on electronic resonances whose transition dipole moments lie in the sample plane. In contrast, SSP spectra report $\chi_{yyz}$, which describes resonances with moments perpendicular to the sample plane. PPP spectra probe all three of these tensor elements in addition to $\chi_{zzz}$, which is sensitive to out-of-plane transitions.

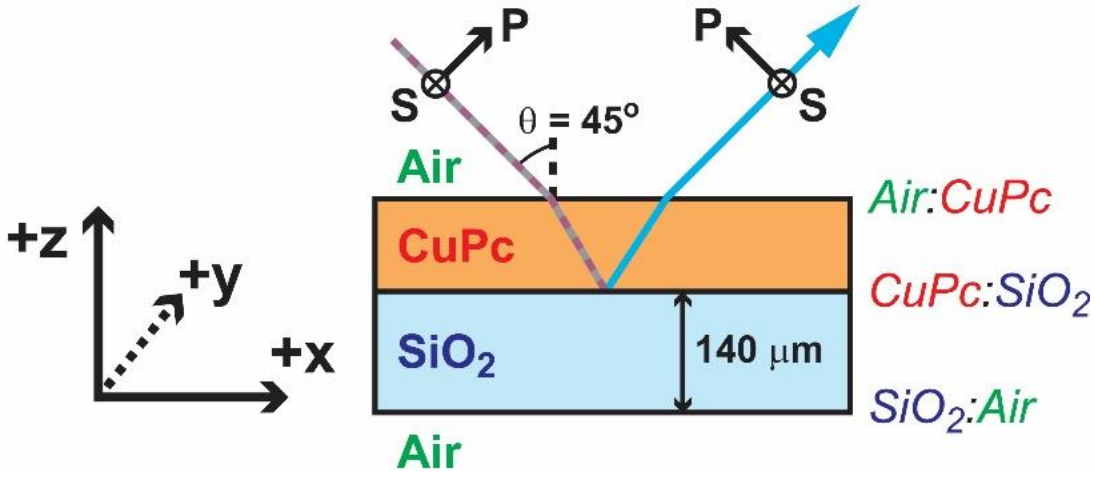


**Figure 5-6**: Frame of reference used for our ESFG experiment

The relative intensities we observe for peak features between SSP, PPP, SPS, and PSS ESFG spectra support the notion that CuPc molecules orient at the $SiO_2$ surface in an edge-on fashion. CuPc molecules oriented normal to this surface should possess Q-band transition moments with both in-plane and out-of-plane character. However, as CuPc

crystallites grow with random orientations in the plane of the surface, in-plane contributions to $\chi^{(2)}$ will be suppressed as the film will on average adopt azimuthal symmetry.[39,40] The absence of strong Q-band features in PSS and SPS spectra supports this scenario. In addition, the larger Q-band signal observed for PPP spectra over SSP spectra is consistent with CuPc oriented normal to the $SiO_2$ interface. While both of these measurements probe transition moments with out-of-plane character, the $\chi_{yyz}$ tensor element measured by SSP spectra represents the product of an out-of-plane transition moment and the in-plane polarizability of the sample film, $\chi_{yyz} = \alpha_{yy}\mu_z$.[41] In contrast, $\chi_{zzz}$ is the product of the out-of-plane transition moment and the sample's out-of-plane polarizability, $\chi_{zzz} = \alpha_{zz}\mu_z$. As the polarizability of CuPc is largest within its molecular plane,[42] if CuPc aligns with this plane normal to the sample surface, this will boost the value of $\chi_{zzz}$ relative to $\chi_{yyz}$.

Turning our focus to the high energy band that appears in the PPP spectrum, we find that it roughly falls into resonance with the $Q_{CT}$ peak observed in CuPc's linear absorption spectrum. As such, we assign this band to $Q_{CT}$ in accord with prior SHG work performed on CuPc films.[6,8] Interestingly, the $Q_{CT}$ resonance also appears in the SSP spectrum but displays lower amplitude and is noticeably blue shifted with respect to a peak near $\lambda_{WL}$ = 535 nm. We believe this amplitude change is in part related to the orientation of interfacial CuPc molecules. However, the spectral shift of this band between SSP and PPP spectra and its complicated peak structure may in part be explained by optical interference between ESFG signals emanating from the CuPc:Air and CuPc:$SiO_2$ interfaces.

### 5.3: Modeling Thin Film Interference

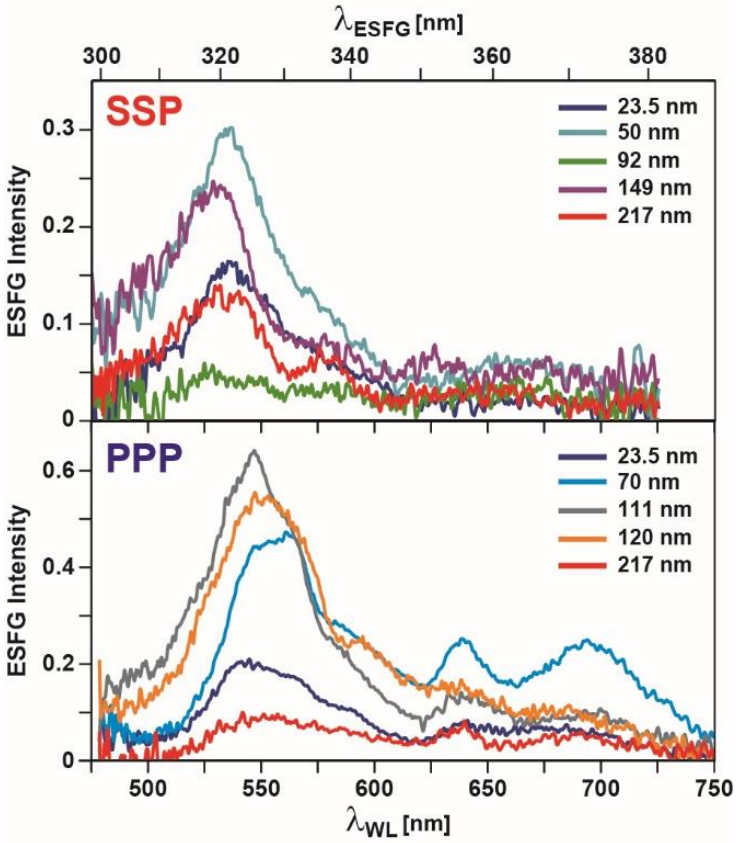


**Figure 5-7**: SSP and PPP ESFG spectra measured as a function of CuPc film thickness.

In Chapter 3 we discussed the need for (and theory behind) a thin film interference model as ESFG is generated from both interfaces within our system (CuPc:Air and CuPc:$SiO_2$), and we need to separate their contributions. To study the effects of this interference and to vet the model described, we have examined how CuPc's ESFG spectrum changes with film thickness (Figure 5-7). If signal purely originates from the buried CuPc:$SiO_2$ surface, we would expect our ESFG signal to peak for our thinnest films and to decrease with increasing film thickness due to attenuation of both the excitation and ESFG fields as they travel to and from this buried interface. In contrast, if ESFG is emitted from both the top and bottom surfaces of our CuPc films, we should observe oscillations

in the intensity of our ESFG signal with film thickness due to changes in the relative phase of these two signals. Examining the SSP data in Figure 5-7, we see that the $Q_{CT}$ band near 535 nm changes its amplitude with film thickness, peaking at a value of 50 nm before decreasing drastically at a thickness of 92 nm and displaying a strong recurrence at 149 nm. The PPP spectra in Figure 5-7 display similar oscillations in band intensities that suggest we observe ESFG from both the CuPc:Air and CuPc:$SiO_2$ interfaces. Although prior studies concluded that SHG emitted by CuPc films resulted from quadrupolar coupling of electric fields to their bulk,[7,9] if ESFG emitted by our films was generated via this mechanism we would expect a quadratic growth of our signal with film thickness,[43] which we do not observe.

The specifics of the model we apply is discussed in detail in Chapter 3. Briefly, to model the oscillatory behavior of our CuPc SSP data, the thickness dependence of the signal is fit by optimizing the values of $\chi_{yyz,Air}$ and $\chi_{yyz,SiO_2}$. Given the complexity of our measured spectra, we have avoided using a line-shape model, such as a sum of complex Lorentizans, to fit our measured spectra. Rather, the values of $\chi_{yyz,Air}$ and $\chi_{yyz,SiO_2}$ are determined on a point-by-point basis by taking individual wavelength slices through the data set and independently optimizing the values of $\chi_{yyz,Air}$ and $\chi_{yyz,SiO_2}$ for each wavelength slice. To ensure that the real and imaginary components of $\chi_{yyz,Air}$ and $\chi_{yyz,SiO_2}$ that result from our fitting routine are Kramers-Kronig consistent, we input an initial guess for the imaginary components of these two quantities, optimize their values with their real components to zero, and then compute their real components using a Kramers-Kronig transform.[44] The thickness dependent ESFG spectra are then recomputed using our now complex values of $\chi_{yyz,Air}$ and $\chi_{yyz,SiO_2}$. If a significant deviation from experiment occurs, the real components of these two quantities are held fixed, their imaginary components reoptimized, and their real components recomputed using via Kramers-Kronig

transformation. This process is repeated until a fit to our ESFG spectra converges. During this process, we assume that $\chi_{yyz,Air}$ and $\chi_{yyz,SiO_2}$ are oppositely signed due to the inversion of the CuPc film orientation with respect to these interfaces. Our model also assumes $\chi_{yyz,Air}$ and $\chi_{yyz,SiO_2}$ are thickness independent, which ignores the possibility of restructuring of these interfaces during film growth. This is likely justified as we observe only minor changes in film roughness with thickness. We also ignore any non-resonant ESFG fields produced by the $SiO_2$ substrate as measurements of bare $SiO_2$ failed to produce any discernable signal. The complex refractive index of CuPc was taken from Reference[45] and assumed to be isotropic throughout the bulk of our CuPc films. This validity of this assumption is supported by prior ellipsometry measurements that have suggested anisotropy in CuPc's refractive index due to a net orientation of CuPc molecules within a film could be ignored for sufficiently thin (<200 nm) films.[45,46] The quality of our fits below supports this assumption.

Figure 5-8 compares our experimental SSP ESFG spectra (Figure 5-8A) and the fit generated by our model (Figure 5-8B). Overall, the model reproduces the data well, predicting the correct location of recurrences as a function of film thickness. This is highlighted in Figure 5-8C, which shows a slice along the ESFG data at $\lambda_{WL}$ = 560 nm. We see that the model matches the peak height and position of the experimental data for films < 100 nm in thickness but underestimates the amplitude of the ESFG signal for thicker films. This discrepancy may arise from minor contributions from electric quadrupolar signals (discussed in a later section) and we are currently working to incorporate a description of these effects into our model. However, we stress that a simple electric dipolar treatment of both interfaces can explain most of the experimental thickness trend for SSP spectra, leading us to conclude that dipolar response dominates the ESFG response.

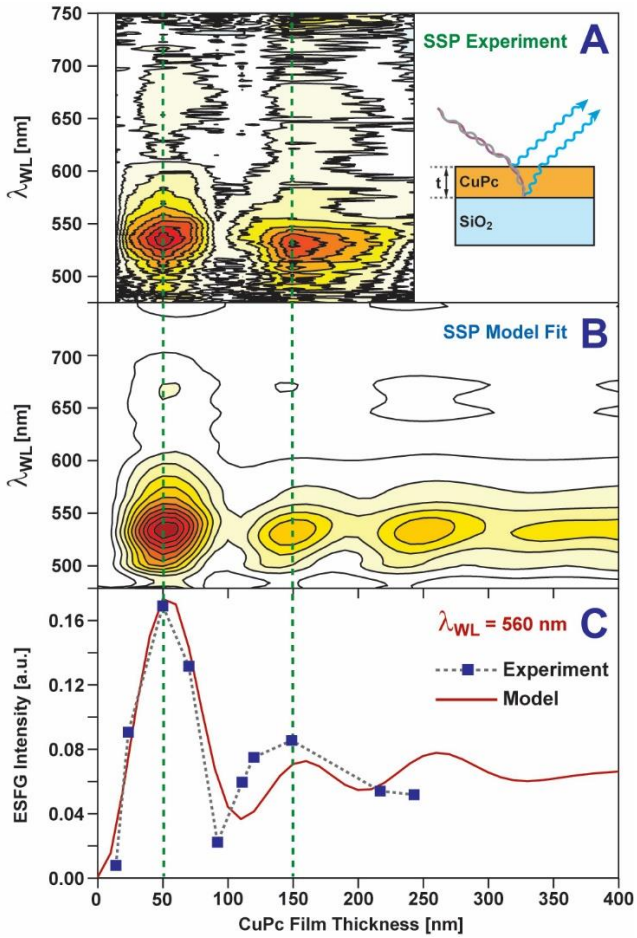


**Figure 5-8**: (A and B) Comparison of measured experimental CuPc SSP spectra and a fit. (C) Side-by-side comparison of experiment and model slice.

Figure 5-9 compares the imaginary portions of the complex quantities, $\chi_{yyz,Air}$ and $\chi_{yyz,SiO_2}$,calculated by fitting the measured SSP spectra. Also shown in the figure are the values of Im[$\chi_{zzz,Air}$] and Im[$\chi_{zzz,SiO_2}$] extracted from PPP spectra, which were fit using the values of $\chi_{yyz,Air}$ and $\chi_{yyz,SiO_2}$ obtained from SSP data and assuming that $\chi_{zyy}$ and $\chi_{yzy}$ are negligible for both interfaces due to the low amplitude measured for PSS and SPS spectra (Figure 5-5 B and C). Focusing first on the buried interface, we find Im[$\chi_{zzz,SiO_2}$] displays two distinct peaks at 645 and 685 nm, similar to the PPP spectrum in Figure 5-4, that we assign to $Q_A$ and $Q_B$. The narrower spacing of these peaks relative to CuPc's linear

absorption spectrum suggests a change in the coupling of CuPc's states at the $SiO_2$ interface.

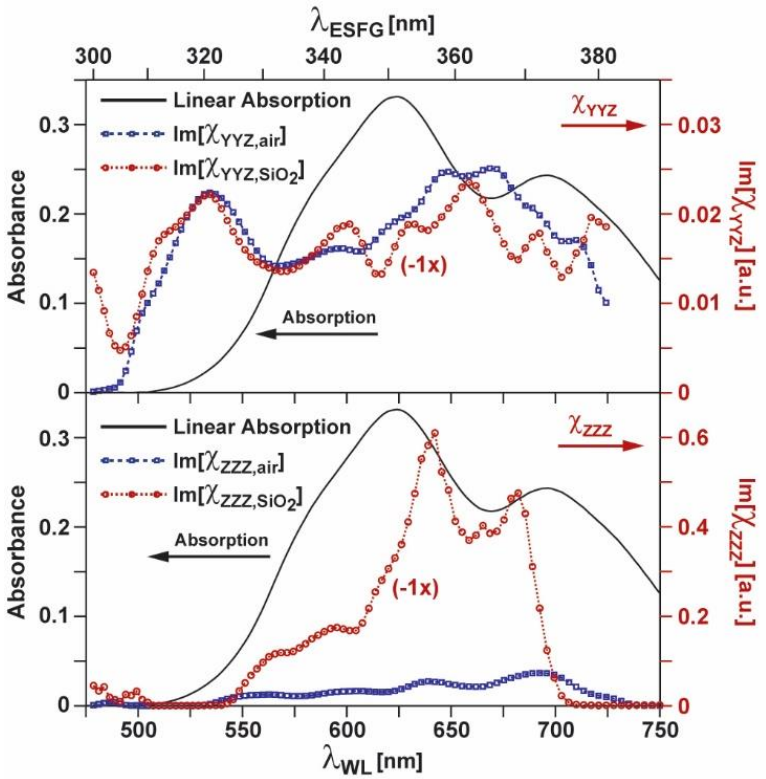


**Figure 5-9**: Comparison of the linear absorption spectrum of a 50 nm CuPc film and the best fit values.

Interestingly, we find the bluest portion of $Q_{CT}$ is strongly suppressed in $Im[\chi_{zzz,SiO_2}]$ appearing instead as a broad resonance peaked near 525 nm in $Im[\chi_{yyz,SiO_2}]$. Thus, we conclude the band we assign to $Q_{CT}$ in our PPP data significantly reflects $\chi_{yyz}$'s contribution to these spectra and that this band's complicated peak structure largely originates from the optical interference of signals emitted by the CuPc:Air and CuPc:$SiO_2$ interfaces. Additionally, prior electro-reflectance studies of CuPc single crystals have concluded that the charge transfer interactions that give rise to $Q_{CT}$ largely involve cofacial molecules arranged along CuPc's b-axis.[26] As our data support a scenario wherein CuPc molecules

preferentially align with their molecular planes normal to the sample surface, this would suggest $Q_{CT}$ is associated with charge transfer interactions that occur within the plane of the sample surface. Exciting this transition then should induce a large change in the in-plane polarizability of the sample and hence a stronger signal from $Im[\chi_{yyz,SiO_2}]$with respect to $Im[\chi_{zzz,SiO_2}]$, indicating this may be an additional contribution to the strength of $Q_{CT}$.

Comparing the response of the CuPc:Air interface to that of CuPc:$SiO_2$, we find $Q_A$ and $Q_B$ are much more intense in $Im[\chi_{zzz,SiO_2}]$ than $Im[\chi_{zzz,SiO_2}]$. This may suggest a stronger degree of vertical alignment of CuPc molecules at the buried interface. Such structural ordering could also in part explain the narrow linewidths we observe for $Q_A$ and $Q_B$ in $Im[\chi_{zzz,SiO_2}]$, which would be consistent with a decrease in structural heterogeneity at the buried CuPc:$SiO_2$ interface. Alternatively, the sharpness of these features as well as their decreased peak spacing relative to that in linear absorption spectra of our films may indicate a decrease in the average size of CuPc crystalline grains at the $SiO_2$ interface. A reduction in crystallite size will lower the number of molecules that electronically couple to give rise to the $Q_A$ and $Q_B$ features that appear in our spectra, reducing both the bandwidth of these features and their peak spacing. However, any change in the average molecular organization of the air-exposed and buried interface would also be expected to induce a change in the relative amplitudes of $Im[\chi_{yyz,SiO_2}]$ and $Im[\chi_{yyz,Air}]$, which we find to be more similar than not. While our fit to our SSP data is very robust, our model's fit to our PPP spectra is of lower quality (Figure 5-10). This likely reflects some of the shortcomings of our model, which assumes no contribution of $\chi_{zyy}$ and $\chi_{yzy}$ to our spectra and that quadrupolar contributions can be ignored. However, given our model's overall good agreement with SSP spectra, we reason that bulk quadrupolar contributions to our PPP spectra are small as a similar amplitude of these signals would be expected for both SSP

and PPP spectra. Rather, if quadrupolar signals contribute to our response, they are likely interfacial in origin as discussed by Matsuzaki *et. al.*[13]

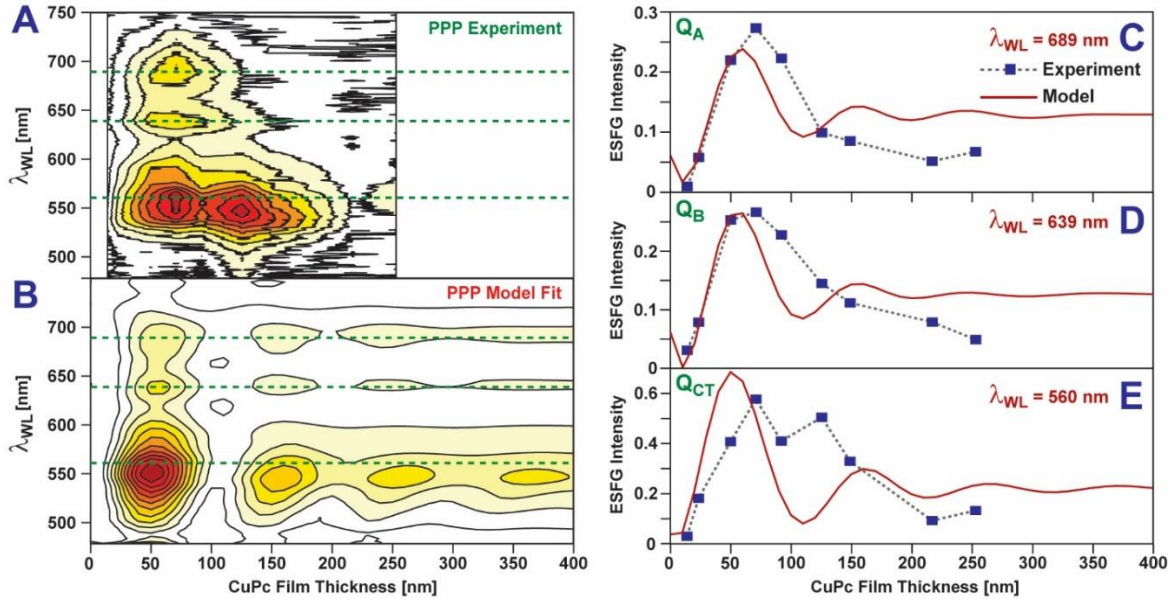


**Figure 5-10**: (A and B) Comparison of experimental CuPc PPP and fit. (C - E) Side-by-side comparison of experiment and model for data slices.

For materials with azimuthal symmetry such as our CuPc sample films, features that appear in PPP spectra are dependent on four nonzero components of $\chi^{(2)}$: $\chi_{yyz}$, $\chi_{yzy}$, $\chi_{zyy}$, and $\chi_{zzz}$.[6] Thus, fitting PPP spectra requires finding values for each of these four terms. As discussed in Chapter 3, $\chi_{yyz}$ can be obtained by fitting SSP spectra as this data only depends on this tensor element. Likewise, $\chi_{yzy}$ and $\chi_{zyy}$ can in principle be found by fitting SPS and PSS spectra, respectively. As seen in Figure 5-5, spectra measured for these two polarization combinations are weak compared to spectra measured for both SSP and PPP polarizations. This implies $\chi_{yzy}$ and $\chi_{zyy}$ are likely small compared to both $\chi_{yyz}$ and $\chi_{zzz}$ and justify setting $\chi_{yzy}$ and $\chi_{zyy}$ equal to zero, which allows us to fit our PPP spectra by floating only a single tensor element, $\chi_{zzz}$.

Figure 5-10 compares PPP spectra measured experimentally as a function of CuPc film thickness to a fit produced by our interference model. Overall, our fit agrees qualitatively well with experiment, especially in the region of the $Q_A$ and $Q_B$ transitions, as highlighted by Figure 5-10C. However, our fit is noticeably poorer near $Q_{CT}$, wherein the model predicts a minimum at a thickness of 100 nm that is not observed experimentally. This discrepancy likely results in part from our neglect of $\chi_{zyy}$ as PSS spectra show a weak but discernable peak due to $Q_{CT}$, but also from our lack of inclusion of EQ source terms as discussed in a later section.

In interpreting the values retrieved for $\mathrm{Im}[\chi_{yyz,SiO_2}]$ and $\mathrm{Im}[\chi_{zz,SiO_2}]$ above, we have compared these quantities to the linear absorption spectra of our films in the Q-band region. This comparison assumes the primary resonance condition that enhances our ESFG spectra is that between our WL pulse and the Q-band. However, the sum of our WL and upconversion fields place them into resonance with CuPc's Soret band, raising the question if this additional resonance enhances our ESFG spectra. In such a scenario, our spectra would represent a product of the transition dipoles[41,47] for moving from the $a_{1u}$ and $e_g$ states that comprise the Q-band, $a_{2u}$ and $e_g$ states that form the Soret band, and importantly, the $a_{1u}$ and $a_{2u}$ states that contribute to both bands.[19] As this latter transition is not dipole allowed, we expect this to strongly reduce doubly resonant contributions to our spectra.

### 5.4: Quadrupolar Contributions to Spectra

Thus far, our interpretation of features observed in ESFG implicitly assumes signal from the films' interfacial regions dominate the response. However, prior SHG studies of CuPc films have suggested the possibility of electric quadrupolar (EQ) contributions to these measurements.[7,9] Specifically, three ESFG contributions can be identified that result from EQ coupling of the sample to either the nonresonant upconversion field (Quad1), the

white light continuum (Quad2), or the outgoing ESFG field (Quad3). In naming these terms we have followed the convention employed by Yamaguchi et. al.[48] In principle, ESFG generated by each of these mechanisms can originate from both the bulk of a sample and from molecules located at interfaces.[12,13,48,49] In particular, interfacial EQ ESFG signals can be of a similar magnitude or larger than those generated by a film's bulk as a discontinuity of the sample's dielectric constant at an interface can create large field gradients for both the incoming excitation fields and emitted ESFG field. Fortunately, the contribution of both bulk and interfacial EQ ESFG signals to our CuPc spectra can be estimated by examining the polarization and thickness dependence of our measured signals. The interfacial contribution to Quad1, Quad2, and Quad3 can be estimated by noting that each of these terms will be largest when the involved field is P-polarized as EQ coupling depends on the gradient of the involved field. These will be maximized along the direction normal to a sample surface due to discontinuities in the sample's dielectric constant along this direction at both the CuPc:Air and CuPc:$SiO_2$ interfaces.[13,48] Thus, we expect the interfacial EQ contribution due to Quad1 to appear in spectra measured for SPS polarization conditions, Quad2 in SSP spectra, Quad3 in PSS spectra, and contributions from all three interfacial EQ terms in PPP spectra.[13] While interfacial EQ signals will experience the same interference effects, bulk EQ signals are expected to grow quadratically with film thickness. Moreover, as the electric quadrupole signals arise from the bulk, we expect spectral features due to these terms to overlap well with bands observed in bulk spectra of our sample films.

To estimate the contribution of interfacial EQ source terms to the $Q_A$ and $Q_B$ bands that appear in CuPc's ESFG spectra, we can use the measured PSS and SPS spectra for two CuPc films with thicknesses of 50 and 111 nm (Figure 5-5 B and C). Overall, the signal intensity is much weaker than that observed for SSP and PPP spectra and given our signal-

to-noise, no features can be clearly attributed to $Q_A$ or $Q_B$ near 682 or 642 nm, respectively. The absence of these features in both PSS and SPS spectra strongly suggest that the interfacial Quad1 and Quad3 contributions do not contribute to $Q_A$ or $Q_B$. Likewise, we can also conclude that bulk EQ contributions to these bands are minimal as their spectral position in our PPP spectra are notably distinct compared to bulk linear absorption spectra. However, at this time we cannot entirely rule out interfacial contributions due to Quad2.

Examining the $Q_{CT}$ region at higher energy, we find that this band is absent from SPS spectra, allowing us to immediately rule out interfacial Quad1 contributions to it. However, for a 50 nm CuPc film, we observe a relatively weak feature in its PSS spectrum that appears at $\lambda_{WL}$ = 550 nm (Figure 5-5B). Increasing the film thickness to 111 nm causes this feature to blueshift to 530 nm and grow in intensity. As the transition dipole moments associated with the intermolecular charge transfer transitions that comprise $Q_{CT}$ are likely polarized within the sample plane due to CuPc's preference to orient with its molecular plane normal to the sample surface, this should give rise to a nonzero value of $\chi_{ZYY,SiO_2}$. However, if our measured PSS spectra were purely due to an electric dipolar response, we would predict from interference modeling that the signal we would measure for a 50 nm film should be larger than that of a 111 nm film. This suggests $Q_{CT}$ likely contains some degree of EQ contribution. As the band we attribute to $Q_{CT}$ in PSS spectra is blue shifted with respect to linear absorption spectra of our CuPc films, both bulk and interfacial Quad3 contributions to this band are likely negligible. Thus, we are left with the conclusion that EQ contributions to $Q_{CT}$ are likely interfacial Quad2 contributions that are then convoluted with the dipolar response. The overall good agreement of our model and SSP spectra suggest that the dominant contribution is dipolar in origin, but the poor fit of our model to PPP spectra in the $Q_{CT}$ region may point to the presence of interfacial Quad2 EQ contributions to this band.

### 5.5: Additional Contributions to Measured ESFG

One potential concern regarding the interpretation of our ESFG spectra is that the structure of our CuPc films may change as they are grown in thickness due to the ability of different crystalline grains to template off of features produced closer to the $SiO_2$ surface. Such thickness dependent variations in film structure could disrupt the centrosymmetry of our films, and potentially allow ESFG to be emitted from their bulk. However, if such a bulk-emission mechanism dominated our ESFG signals we would expect to observe a quadratic growth of signal intensity with CuPc film thickness as the nonlinear susceptibility, $\chi^{(2)}$, of our samples should scale linearly with film thickness. As we do not observe this trend in our data, this argues against there being contributions to our spectra due to a continual variation in film structure. Moreover, this conclusion is consistent with our observation that we can well reproduce our measured spectra using a model that includes an isotropic refractive index. If significant structural variation in our films occurred as they were grown, this would likely result in a significant asymmetry in the optical constants of our films. We find such variations, if they do exist, are likely small as we do not need to account for them to fit our spectra.

A second process to consider is the interaction of both the upconversion and WL fields with DC fields present within our samples. Indeed, the presence of a DC field can facilitate mixing of the upconversion and WL fields via a four-wave, $\chi^{(3)}$, mixing process. As the DC field resides at zero frequency, this process would produce photons at the sum frequency of the upconversion and WL fields. However, we are confident this process makes minimal contributions, if any, to our spectra. In our experiments, no voltage bias is applied to our samples. As such, any DC component that could mix with our driving fields must come from the static buildup of charge carriers produced by the WL excitation field during our measurements. We believe we can rule out the presence of these species for two

reasons: (1) The repetition rate of our laser is 3 kHz, so any trapped charge carriers produced would need to live for at least 333 μs to have an impact on our data. This seems very long for the lifetime of such species. (2) The primary relaxation pathway for singlet excitons in CuPc films is likely not charge generation but rather intersystem crossing, which has been measured to occur on a 1 ps rate,[50] followed by internal conversion to the ground state. The formation of free carriers is likely uphill in energy from the triplet state, suggesting their population in our films is negligible. Moreover, even in the event that static fields contribute to our spectra, they will act to modify the amplitude of spectral features, but not their energetic positions. This is because static fields contribute a zero-frequency component to a sample's nonlinear response. Thus, even if the amplitude of spectral features we observe are enhanced by static fields internal to our sample films, the shifts we observe for the $Q_A$ and $Q_B$ features in our spectra will not be impacted by such enhancement.

### 5.6: Conclusions

In conclusion, we have demonstrated ESFG can probe the electronic structure of buried interfaces in OSC films. By analyzing the polarization dependence of the emitted field, we can recover information that reports on the orientation of molecules at this interface. Our results indicate it is important to consider the presence of signals generated from each sample interface and their interference. We caution the analysis of thin film ESFG data that does not account for this effect. Through the use of a thin film model, we were able to extract the electronic density of states of both the buried and exposed interfaces within our sample, an essential task for the study of energy and charge transfer within organic semiconductors.

## 5.7: Chapter References


(1) Tang, C. W. Two-Layer Organic Photovoltaic Cell. *Appl. Phys. Lett.* **1986**, *48*, 183–185.

(2) Stillman, M. J.; Nyokong, T. Absorption and Magnetic Circular Dichrosim Spectral Properties of Phthalocyanines Part 1: Complexes of the Dianion Pc(-2). In *Phthalocyanines: Properties and Applications*; VCH: New York, 1989; Vol. 1, pp 133–290.

(3) Ashida, M.; Uyeda, N.; Suito, E. Unit Cell Metastable-Form Constants of Various Phthalocyanines. *Bull. Chem. Soc. Jpn.* **1966**, *39* (12), 2616–2624.

(4) Hoshino, A.; Takenaka, Y.; Miyaji, H. Redetermination of the Crystal Structure of A-Copper Phthalocyanine Grown on KCl. *Acta Crystallogr.* **2003**, *B59*, 393–403.

(5) Cruickshank, A. C.; Dotzler, C. J.; Din, S.; Heutz, S.; Toney, M. F.; Ryan, M. P. The Crystalline Structure of Copper Phthalocyanine Films on ZnO($1\bar{1}00$). *J. Am. Chem. Soc.* **2012**, *134* (35), 14302–14305.

(6) Sato, M.; Takeuchi, A.; Yamada, T.; Hoshi, H.; Ishikawa, K.; Mori, T.; Takezoe, H. Intermolecular Transitions Observed by Electric-Quadrupole-Resonant Second-Harmonic Generation in a Discotic Liquid Crystal of Phthalocyanine. *Phys. Rev. E* **1997**, *56* (6), R6264–R6266.

(7) Yamada, T.; Hoshi, H.; Manaka, T.; Ishikawa, K.; Takezoe, H.; Fukuda, A. Resonant Enhancement of Second-Harmonic Generation of Electric Quadrupole Origin in Phthalocyanine Films. *Phys. Rev. B* **1996**, *53* (20), R13314–R13317.

(8) Yamada, T.; Manaka, T.; Hoshi, H.; Ishikawa, K.; Takezoe, H. Optical Second Harmonic Generation Spectra in Vacuum-deposited Thin Films of Various Phthalocyanines. *J. Porphyr. Phthalocyanines* **1998**, *2* (2), 133–137.

(9) Hoshi, H.; Yamada, T.; Ishikawa, K.; Takezoe, H.; Fukuda, A. Second-Harmonic Generation in Centrosymmetric Molecular Films: Analysis under Anisotropic Conditions. *Phys. Rev. B* **1995**, *52* (16), 12355–12365.

(10) Chollet, P.-A.; Kajzar, F.; Moigne, J. L. Structure and Nonlinear Optical Properties of Copper Phthalocyanine Thin Films. *Mol. Eng.* **1991**, *1* (1), 35–47.

(11) Li, C. Q.; Manaka, T.; Cheng, X. M.; Iwamoto, M. Second Harmonic Generation from Copper-Tetratert-Butyl-Phthalocyanine Langmuir-Blodgett Film/Metal Interface: Electric Quadrupole or Electric Field Induced Second Harmonic Generation Effect? *J. Appl. Phys.* **2002**, *92* (11), 6390–6398.

(12) Sun, S.; Tian, C.; Shen, Y. R. Surface Sum-Frequency Vibrational Spectroscopy of Nonpolar Media. *Proc. Natl. Acad. Sci.* **2015**, *112* (19), 5883–5887.

(13) Matsuzaki, K.; Nihonyanagi, S.; Yamaguchi, S.; Nagata, T.; Tahara, T. Vibrational Sum Frequency Generation by the Quadrupolar Mechanism at the Nonpolar Benzene/Air Interface. *J. Phys. Chem. Lett.* **2013**, *4* (10), 1654–1658.

(14) Guyot-Sionnest, P.; Shen, Y. R. Bulk Contribution in Surface Second-Harmonic Generation. *Phys. Rev. B* **1988**, *38* (12), 7985–7989.

(15) O'Brien, D. B.; Massari, A. M. Modeling Multilayer Thin Film Interference Effects in Interface-Specific Coherent Nonlinear Optical Spectroscopies. *J. Opt. Soc. Am. B* **2013**, *30* (6), 1503–1503.

(16) O'Brien, D. B.; Massari, A. M. Experimental Evidence for an Optical Interference Model for Vibrational Sum Frequency Generation on Multilayer Organic Thin Film Systems I: Electric Dipole Approximation. *J. Chem. Phys.* **2015**, *142*, 024703–024703.

(17) O'Brien, D. B.; Massari, A. M. Experimental Evidence for an Optical Interference Model for Vibrational Sum Frequency Generation on Multilayer Organic Thin Film Systems II: Consideration for Higher Order Terms. *J. Chem. Phys.* **2015**, *142*, 024704–024704.

(18) O'Brien, D. B.; Massari, A. M. Simulated Vibrational Sum Frequency Generation from a Multilayer Thin Film System with Two Active Interfaces. *J. Chem. Phys.* **2013**, *138* (15), 154708–154708.

(19) Mack, J.; Stillman, M. J. Band Deconvolution Analysis of the Absorption and Magnetic Circular Dichroism Spectral Data of ZnPc (-2) Recorded at Cryogenic Temperatures. *J. Phys. Chem.* **1995**, *99* (20), 7935–7945.

(20) Mack, J.; Stillman, M. J. Electronic Structures of Metal Phthalocyanine and Porphyrin Complexes from Analysis of the UV–Visible Absorption and Magnetic Circular Dichroism Spectra and Molecular Orbital Calculations. In *The Porphyrin Handbook: Volume 16, Phthalocyanines: Spectroscopic and Electrochemical Characterization*; Academic Press: Amsterdam, 2003; Vol. 16, pp 43–116.

(21) E. A. Lucia; Verderame, F. D. Spectra of Polycrystalline Phthalocyanines in the Visible Region. *J. Chem. Phys.* **1968**, *48* (6), 2674–2681.

(22) Schechtman, B. H.; Spicer, W. E. Near Infrared to Vacuum Ultraviolet Absorption Spectra and the Optical Constants of Phthalocyanine and Porphyrin Films. *J. Mol. Spectrosc.* **1970**, *33*, 28–48.

(23) Huang, T.-H.; Rieckhoff, K. E.; Voigt, E. M. New Singlets in the Phthalocyanines. *J. Phys. Chem.* **1981**, *85* (22), 3322–3326.

(24) Van Cott, T. C.; Rose, J. L.; Misener, G. C.; Williamson, B. E.; Schrimpf, A. E.; Boyle, M. E.; Schatz, P. N. Magnetic Circular Dichroism and Absorption Spectrum of Zinc Phthalocyanine in an Argon Matrix between 14700 and 74000 Cm-1. *J. Phys. Chem.* **1989**, *93* (8), 2999–3011.

(25) Nemykin, V. N.; Hadt, R. G.; Belosludov, R. V.; Mizuseki, H.; Kawazoe, Y. Influence of Molecular Geometry, Exchange-Correlation Functional, and Solvent Effects in the Modeling of Vertical Excitation Energies in Phthalocyanines Using Time-Dependent Density Functional Theory (TDDFT) and Polarized Continuum Model TDDFT Methods: Can Modern Computational Chemistry Methods Explain Experimental Controversies? *J. Phys. Chem. A* **2007**, *111* (50), 12901–12913.

(26) Tokura, Y.; Koda, T.; Iyechika, Y.; Kuroda, H. Electro-Reflectance Spectra of Charge-Transfer Excitations in Copper Phthalocyanine Single Crystals. *Chem. Phys. Lett.* **1983**, *102* (2), 174–178.

(27) Yoshida, H.; Tokura, Y.; Koda, T. Charge-Transfer Excitation Bands in Electro-Absorption Spectra of Metal (Co, Ni, Cu, Zn)-Phthalocyanine Films. *Chem. Phys.* **1986**, *109* (2–3), 375–382.

(28) Kirichenko, N. A.; Blinov, L. M. Charge-Transfer States and Optical Spectra in the Condensed Phase. *Zhurnal Prikl. Spektrosk.* **1978**, *28* (6), 1057–1061.

(29) Knupfer, M.; Schwieger, T.; Peisert, H.; Fink, J. Mixing of Frenkel and Charge Transfer Excitons in Quasi-One-Dimensional Copper Phthalocyanine Molecular Crystals. *Phys. Rev. B* **2004**, *69* (16), 165210.

(30) Resel, R.; Ottmar, M.; Hanack, M.; Keckes, J.; Leising, G. Preferred Orientation of Copper Phthalocyanine Thin Films Evaporated on Amorphous Substrates. *J. Mater. Res.* **2000**, *15* (04), 934–939.

(31) Cheng, C. H.; Wang, J.; Du, G. T.; Shi, S. H.; Du, Z. J.; Fan, Z. Q.; Bian, J. M.; Wang, M. S. Organic Solar Cells with Remarkable Enhanced Efficiency by Using a CuI Buffer to Control the Molecular Orientation and Modify the Anode. *Appl. Phys. Lett.* **2010**, *97* (8), 083305.

(32) Peisert, H.; Schwieger, T.; Auerhammer, J. M.; Knupfer, M.; Golden, M. S.; Fink, J.; Bressler, P. R.; Mast, M. Order on Disorder: Copper Phthalocyanine Thin Films on Technical Substrates. *J. Appl. Phys.* **2001**, *90* (1), 466–469.

(33) Berger, O.; Fischer, W.-J.; Adolphi, B.; Tierbach, S.; Melev, V.; Schreiber, J. Studies on Phase Transformations of Cu-Phthalocyanine Thin Films. *J. Mater. Sci. Mater. Electron.* **2000**, *11* (4), 331–346.

(34) Brown, C. J. Crystal Structure of β-Copper Phthalocyanine. *J. Chem. Soc. Inorg. Phys. Theor.* **1968**, 2488–2493.

(35) Rand, B. P.; Cheyns, D.; Vasseur, K.; Giebink, N. C.; Mothy, S.; Yi, Y.; Coropceanu, V.; Beljonne, D.; Cornil, J.; Brédas, J.-L.; et al. The Impact of Molecular Orientation on the Photovoltaic Properties of a Phthalocyanine/Fullerene Heterojunction. *Adv. Funct. Mater.* **2012**, *22* (14), 2987–2995.

(36) Kobayashi, T.; Fujiyoshi, Y.; Uyeda, N. The Observation of Molecular Orientations in Crystal Defects and the Growth Mechanism of Thin Phthalocyanine Films. *Acta Crystallogr.* **1982**, *A38*, 356–362.

(37) Yost, S. R.; Voorhis, T. V. Electrostatic Effects at Organic Semiconductor Interfaces: A Mechanism for "Cold" Exciton Breakup. *J. Phys. Chem. C* **2013**, *117* (11), 5617–5625.

(38) Kumagai, K.; Mizutani, G.; Tsukioka, H.; Yamauchi, T.; Ushioda, S. Second-Harmonic Generation in Thin Films of Copper Phthalocyanine. *Phys. Rev. B* **1993**, *48* (19), 14488–14495.

(39) Shen, Y. R. *The Principles of Nonlinear Optics*; Wiley-Interscience: New York, 1984.

(40) Richmond, G. L. Molecular Bonding and Interactions at Aqueous Surfaces as Probed by Vibrational Sum Frequency Spectroscopy. *Chem. Rev.* **2002**, *102* (8), 2693–2724.

(41) Lin, C.-K.; Hayashi, M.; Lin, S. H. Theoretical Formulation and Simulation of Electronic Sum-Frequency Generation Spectroscopy. *J. Phys. Chem. C* **2013**, *117* (45), 23797–23805.

(42) Ramprasad, R.; Shi, N. Polarizability of Phthalocyanine Based Molecular Systems: A First-Principles Electronic Structure Study. *Appl. Phys. Lett.* **2006**, *88* (22), 222903.

(43) Stiopkin, I. V.; Jayathilake, H. D.; Bordenyuk, A. N.; Benderskii, A. V. Heterodyne-Detected Vibrational Sum Frequency Generation Spectroscopy. *J. Am. Chem. Soc.* **2008**, *130*, 2271–2275.

(44) Lucarini, V.; Saarinen, J. J.; Peiponen, K.-E.; Vartiainen, E. *Kramers-Kronig Relations in Optical Materials Research*; Optical Sciences; Springer: Berlin, 2005.

(45) Djurisic, A. B.; Kwong, C. Y.; Lau, T. W.; Guo, W. L.; Li, E. H.; Liu, Z. T.; Kwok, H. S.; Lam, L. S. M.; Chan, W. K. Optical Properties of Copper Phthalocyanine. *Opt. Commun.* **2002**, *205*, 155–162.

(46) Barrett, M. A.; Borkowska, Z.; Humphreys, M. W.; Parsons, R. Ellipsometry of Thin Films of Copper Phthalocyanine. *Thin Solid Films* **1975**, *28* (2), 289–302.

(47) Moad, A. J.; Simpson, G. J. A Unified Treatment of Selection Rules and Symmetry Relations for Sum-Frequency and Second Harmonic Spectroscopies. *J. Phys. Chem. B* **2004**, *108* (11), 3548–3562.

(48) Yamaguchi, S.; Shiratori, K.; Morita, A.; Tahara, T. Electric Quadrupole Contribution to the Nonresonant Background of Sum Frequency Generation at Air/Liquid Interfaces. *J. Chem. Phys.* **2011**, *134* (18), 184705.

(49) Guyot-Sionnest, P.; Shen, Y. R. Local and Nonlocal Surface Nonlinearities for Surface Optical Second-Harmonic Generation. *Phys. Rev. B* **1987**, *35* (9), 4420.

(50) Dutton, G. J.; Robey, S. W. Exciton Dynamics at CuPc/C 60 Interfaces: Energy Dependence of Exciton Dissociation. *J. Phys. Chem. C* **2012**, *116* (36), 19173–19181.

# Chapter 6: Detecting Difference in Interfacial Order for Perylenediimide Derivatives Through ESFG

## 6.1: Introduction

Wide spread solar energy usage presents a compelling step toward fully green energy. As silicon (Si) processing has advanced to become more efficient and cheaper, this goal is all the more attainable. However, there is an inherent issue that limits the total possible efficiency of solar energy technology: the Shockley-Queisser limit.[1] A substantial energy loss mechanism is thermalization from photons above the band-gap within silicon semiconductor devices.[2] If a photon of energy higher than the inherent band gap impinges on the device, the excited electron-hole pair will undergo thermalization to the band-edge, dissipating the excess energy as heat and extracting charges that only provide the energy of the band gap. Making multijunction solar cells with many different materials can greatly mitigate these losses, but can be cost prohibitive due to the expense of the new inorganic systems as well as increased complexity to device manufacturing.[1–3] Instead, singlet fission presents a potentially cost-effective alternative through the use of organic dyes.

Singlet fission (SF) is a process by which the absorption of a single photon of energy can be converted to two lower energy excitations across two molecules within the system. This is possible when an organic dye has a singlet excited state that is roughly two times greater than its triplet state.[2,4–7] The process of converting to triplet excitations from a singlet can also be quite fast, as through the use of two molecules, no spin flipping is necessary to achieve a spin-triplet excitation. Through careful consideration of the energetics within the dye molecule used, an SF active material can be combined with a Si solar cell to reduce energy loss within the device.[3,8,9] If the singlet energy is higher than the band gap of silicon, and the triplet of the dye equal to silicon's bandgap, a high energy photon can be absorbed within the dye, converted to two excitations, and both can then be

transferred into the Si reducing thermalization losses. The primary advantage of using organic dyes over multijunction inorganic cells is the cost of manufacturing. These molecules can be deposited onto the Si layer through low cost, low energy means such as spin coating, as opposed to the high energy methods required for the growth of crystalline inorganic materials, and would not require the additional complexities inherent to tandem solar cell designs. Concerns for the balancing act between film thickness and excited state lifetime are also reduced within these systems. Given the long lifetime of triplet states, the film can be thick enough to absorb all of the photons that interact with the device and still allow triplets from the outer interface to migrate to the Si for transfer and extraction. Yet, while this idea was originally proposed in the 70's by Dexter,[9] SF has yet to be incorporated into a working Si solar cell device due to poor transfer from dye molecules to Si for charge separation.[3,10–12]

Dye sensitized solar cells that operate on the principle of SF have often been tested with pentacene, which has been shown to readily undergo singlet fission.[11,12] Generally, there is evidence of minimal triplet transfer into a solar cell for current collection.[8] This is likely due to poor transfer into the silicon layer (the cause for which is poorly understood): to separate charge and generate free carriers, the triplet generated within the organic dye must be transferred into silicon.[10] The cause of poor transfer has many potential sources. For instance, band bending at the interface between the two layers could lead to changes in the energetic landscape that prevent excitons from efficient movement into the inorganic system.[8,11] The morphology of the organic dye at the junction could also be a bottle neck to transfer. It is easy to imagine certain molecular orientations that could lead to strong transfer as well as others that don't, and it's possible the dye doesn't generally adopt a proper orientation relative to the silicon's surface.[8,13] A further reason that potentially ties

the previous ideas together is the effect the morphology at the interface might have on the energetics of the molecule's triplet energy.[6,14–16]

Organic dyes tend to have strong energetic coupling between individual molecules within a film, and the energetic states of the film can differ greatly as a function of the morphology of the sample.[6,15] This is readily seen for the singlet energy when moving organic dyes from solution to the solid state as thin films.[6,14,15] Thus, due to changes in the morphology of the dye at the junction with silicon, the triplet energy may have shifted relative to the bulk such that it is lower in energy than the band gap of silicon, preventing transfer from both energetics as well as morphology.[6,8,16–19] To truly understand the cause of poor transfer, there is a critical need to determine how the film is affected when interacting with silicon, however this need is a complex problem to address. Notice that all the potential complications listed are specific to changes in the films energetic density of states (DoS) and its morphology around an interface that is buried within the system. While there are excellent tools for studying these effects, (electronic absorption for DoS and morphology interactions[20], x-ray diffraction and atomic force microscopy[21–23] for morphology to name a few), these techniques are either much more sensitive to the bulk of the film or are limited to examine only the exposed interfaces rather than the buried ones. We need a method that allows for the study of this transfer process through energetics and the morphology at a buried interface, and electronic sum frequency generation is a fantastic tool to address this requirement.

Electronic sum frequency generation (ESFG) can serve as an interfacial probe of the electronic DoS and morphology of a thin film organic-inorganic hybrid system.[24–26] As discussed in previous sections, the selection rules allow for similar experiment to an interface specific absorption measurement that, with proper consideration of the polarization of our beams, can provide information on the morphology of the molecular

system. In Chapter 5 we used thin films of Copper Phthalocyanine to benchmark the sensitivity of ESFG to the differences between the bulk and the interface for an organic dye.[27] In this Chapter, we will instead switch to thin films of different derivatives of perylenediimide (PDI) films. We choose to examine this new class of organic dye as it has many desirable qualities for use as an active SF layer within a dye sensitized solar cell. First, our group and others have shown that PDI's readily undergo SF when in the solid state as thin films.[28,29] Additionally, the triplet energy for many of the derivatives are near the proper energy for transfer to a Si system (around 1.1 eV).[6,28] These dyes are also easily functionalized to form many different derivatives that have many different packing structures, and these morphological changes gives us a handle for different packing arrangements at the bulk to examine.[6,20,30] Finally, despite the significantly high number of studies performed on the acene class of molecules, the rylene dyes show a much higher stability in air, with stronger absorption cross sections, making them potentially better for use in dye-sensitized solar cells. For this chapter, we will look at the differences between three PDI derivatives deposited as thin films on fused quartz substrates in preparation for moving to films on silicon. Additionally, we will implement the change from the 800 nm upconversion for ESFG to using the TOPAS for upsconversion as discussed in Chapter 4.

**6.2: Materials**

For our systems of interest, we have chosen three derivatives within the PDI family through substitution at the imide position of the base PDI molecule (Figure 6-1): N−N′-dimethyl-3,4,9,10-perylenedicarboximide (C1-PDI, black)**,** -dioctyl (C8-PDI, red), and - diethylphenyl (EP-PDI, blue). The derivatives are vapor deposited at varying thickness onto 1 mm thick fused quartz substrates. Figure 6-1 shows the absorption spectra for 50-60 nm thick films for each derivative used. As we can see in Figure 6-1, the absorption

spectra shift greatly as the functional group on the PDI is changed. This is due to subtle shifts of molecules within the molecular stack of the PDI sample that alter the electronic coupling between molecules within a stack.[20,30] The proximity of these molecules in the solid state enhances dipolar through-space coupling between distant molecules as well as direct charge-resonance interactions between neighboring PDIs that modify their absorption spectra. PDI films grow long co-facial stacks with strong coupling of the conjugated π-orbitals, which cause large changes in their electronic absorption spectra. This gives us a strong handle to manipulate the energetics of the film and a way to determine morphological differences at an interface relative to the bulk film.

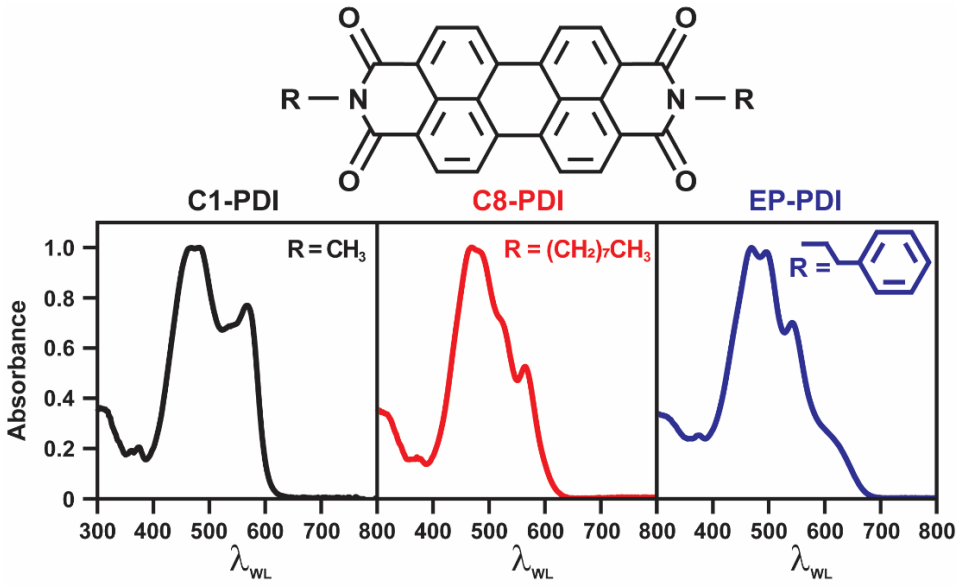


**Figure 6-1**: Molecular structure for the base PDI molecule and Absorption spectra for films of C1-PDI, C8-PDI, and EP-PDI

The primary absorption for each derivative has a four peaked structure that occurs between $\lambda_{WL}$ = 400 nm and $\lambda_{WL}$ = 700 nm. For the C1-PDI derivative, the linear absorption has a strong peak at $\lambda_{WL}$ = 568 nm with a weak companion peak at $\lambda_{WL}$ = 540 nm and a strong, closely spaced two peak structure at $\lambda_{WL}$ = 480 nm and $\lambda_{WL}$ = 468 nm. For the C8-

PDI derivative there is a comparatively weak peak on the red edge at $\lambda_{WL}$ = 565 nm, a weak shoulder at $\lambda_{WL}$ = 540 nm, and a similar two peak structure as in C1-PDI at $\lambda_{WL}$ = 480 nm and $\lambda_{WL}$ = 468 nm. Finally, for the EP-PDI derivative the lowest energy peak is a poorly defined shoulder at $\lambda_{WL}$ = 624 nm, a much stronger peak at $\lambda_{WL}$ = 542 nm, and again the stronger two peaked structure at $\lambda_{WL}$ = 495 nm and $\lambda_{WL}$ = 469 nm.

To characterize the degree of polycrystallinity and crystallite texturing, we used a representative a ~50 nm C1-PDI film deposited on a glass coverslip. Grazing-incidence wide-angle X-ray scattering (GIWAXS) produced the resultant diffractogram ($\lambda$ = 1.5461 Å; $\omega$ = 0.2°) is shown in Figure 6-2 A. The spectrum is shown on a logarithmic scale to highlight the diffraction peaks observed against a nonlinear background. The measured diffraction pattern indicates the presence of crystallites within the film whose structure are in agreement with that published by Hädicke and Graser[31] (Figure 6-2, inset).

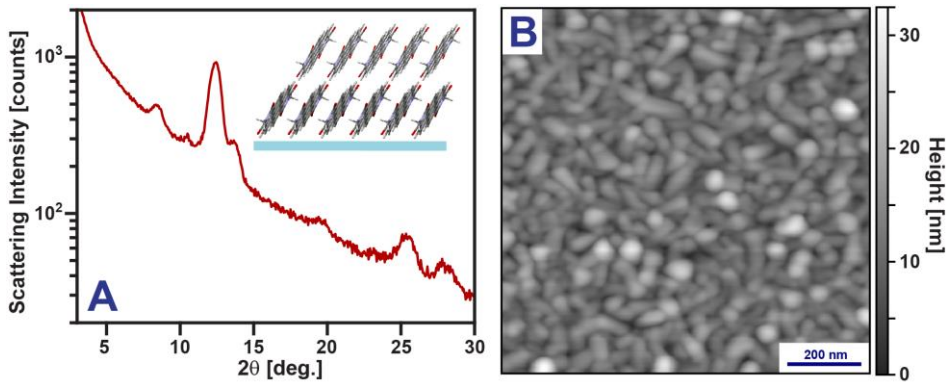


**Figure 6-2:** (A) GIWAXS diffractogram of a ~50 nm C1-PDI film grown on a glass substrate (B) AFM image of the same film.

Atomic force microscopy (AFM) was performed with an Asylum Research MFD-3D AFM in tapping mode using an aluminum coated n-type silicon cantilever (μmasch, HQ:NSC14/Al BS) to image the film's topography. Analysis of the resulting AFM images was carried out using the Gwyddion software package. Figure 6-2B displays a

representative AFM image of a C1-PDI film. The AFM image highlights the polycrystalline nature of the film, indicating that it is comprised of crystalline grains with an average diameter of ~50 nm that cover the full surface of the film.

### 6.3: ESFG Spectrometer

The changes to the ESFG spectrometer are described in detail in Chapter 4. Briefly, the generation of the white light supercontinuum for ESFG remains the same, but instead of using a left over portion of the fundamental from the 804 nm fundamental pump laser for upconversion, we have switched to a field generated using an optical parametric amplifier (OPA, TOPAS 400 New Light Photonics). The OPA allows us to tune across the near IR, in principle from ~885 nm to further than ~1075 nm. The ability to tune the upconversion beam allows further control of the wavelength range across which the ESFG is emitted to avoid complications from reabsorption. Additionally, by shifting the energy of the upconversion field we can move farther from possible resonance of the upconversion with the sample. For this Chapter, we limit ourselves to upconverting with 885 nm light. The OPA beam has a temporal width of roughly 3 ps, which allows us to upconvert the entire WL spectrum at a single time delay between the upconversion and white light fields as opposed to the 804 nm beam, which required scanning time delays as in Chapter 5. To avoid sample damage, the beam energies used for the C1-PDI were 2.1 mJ for the white light beam and 12.5 mJ for the 885 nm upconversion. For the C8-PDI and EP-PDI, the energy was lowered to 0.7 mJ and 8 mJ, as these films damaged more easily. The collection time for each film was consistent for a derivative, but varied for better signal to noise for each derivative, with 2 min. C1-PDI, 5 min. C8-PDI, and 10 min. for the EP-PDI data.

## 6.4: Results

With a variety of PDI derivatives to study, we can begin to elucidate differences in the DoS and morphology of not only the bulk of these films but also their interface. For C1-PDI and C8-PDI, we will focus the discussion on the ESFG spectra from a single film thickness that is representative of the approximately seven different film thicknesses measured across a thickness range from about 30 nm to 250 nm. For the EP-PDI, we measured four thickness points, and will examine in detail the ESFG spectra from each as they vary greatly across the thickness series. Figure 6-3 shows the ESFG spectra for a 51 nm C1-PDI film collected for the PPP, SPS, SSP, and PSS polarization conditions compared to its electronic absorption spectrum. These spectra are all normalized relative to the strongest peak in the PPP spectrum of the derivative to maintain the ratio between the polarization conditions. We see drastic differences in the DoS for the interface relative to the bulk for the C1-PDI film.

Starting with the PPP spectrum, we see that the four peaks that contribute to the electronic absorption are lost and only two peaks remain, the strongest at $\lambda_{WL}$ = 585 nm and the weaker at $\lambda_{WL}$ = 521 nm. In addition to the change in the number of peaks, there is also a redshift in energy of the peak location relative to the electronic absorption of 10 nm (comparing the lowest energy peak for both ESFG and absorption). The peak at $\lambda_{WL}$ = 521 nm seems to fall in a valley relative to the absorption, and is more difficult to assign to a single peak. This description continues to the SPS spectra, where we see a slight red shift of the low energy peak to $\lambda_{WL}$ = 588 nm accompanied by a reduction in intensity. For the high energy peak, we again see a slight red shift (to $\lambda_{WL}$ = 522 nm), but with no change in peak intensity. Moving to SSP, we lose the high energy peak, instead having only a single, broad peak centered at $\lambda_{WL}$ = 590 nm with much lower intensity compared to PPP and SPS. PSS shows zero signal for the beam energy and collection time used in these experiments.

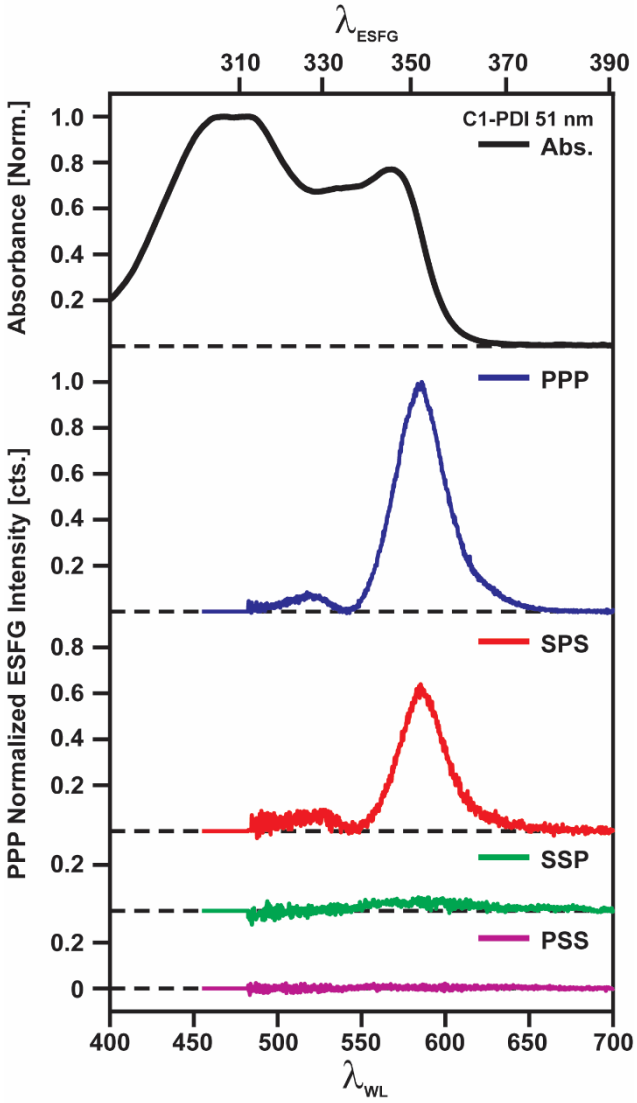


**Figure 6-3**: Comparison of 51 nm C1-PDI ESFG vs absorption. ESFG spectra normalized to PPP spectra

As discussed in Chapter 5, we can begin to determine the morphology of the interfacial molecules for the C1-PDI. Given the strength of the SPS signal, where $\chi_{YZY} = \alpha_{YZ}\mu_Y$, we are probing the in-plane transition dipole of the C1-PDI with an out-of-plane polarizability. Given that the transition dipole for the PDI molecule lies along the long axis of perylene core, this would indicate the molecule primarily lies parallel to the substrate

surface (Figure 6-2 A inset). This is consistent with the weak SSP spectrum, which probes an out of plane dipole with in plane polarizability. The PPP spectra is somewhat trickier to interpret, as it probes all four nonzero non-linear susceptibility terms, $\chi_{ZZZ}, \chi_{YZY}, \chi_{YYZ}$, and $\chi_{ZYY}$. However, given the intensity of the PPP spectrum, it is clear that $\chi_{ZZZ}$ has a strong contribution to the measured signal. This, combined with the small ESFG signal from the SSP spectrum, could indicate that the molecules don't lie perfectly within the plane of the sample. Another possibility is that, while we assume the an SFG spectrum's signal intensity modulation comes from resonance with the dipole moment of the molecule, the polarizability of the molecular stack could be strongly anisotropic and contribute to the measured signal's polarization dependence. As C1-PDI forms tall molecular stacks, the strong intermolecular coupling known to exist within these molecules combined with its orientation relative to the substrate surface suggests there might be strong polarizability perpendicular to the surface of the substrate and diminished polarizability parallel to it.

Moving to C8-PDI (Figure 6-4) we see a similar story to that of C1-PDI, at least in the red shift for peaks in the ESFG spectra relative to those in the electronic absorption where the interfacial signal is significantly different from that of the bulk film. We again see a reduction in the number of peaks that comprise the measured spectra, here showing the same two peak structure for PPP in comparison to the electronic absorption spectrum. The lowest energy peak occurs at $\lambda_{WL}$ = 587 nm, a red shift of 22.5 nm relative to the lowest energy peak for the absorption spectrum. The high energy peak for ESFG occurs at $\lambda_{WL}$ = 505 nm, again roughly in the middle of the broad electronic absorption for the bulk of the film. For C8-PDI, we find that the next strongest ESFG signal occurs for the SSP polarization combination, showing a single, broad peak centered at about $\lambda_{WL}$ = 595 nm. SSP and PSS show no significant intensity for the collection time and beam energy used for these experiments.

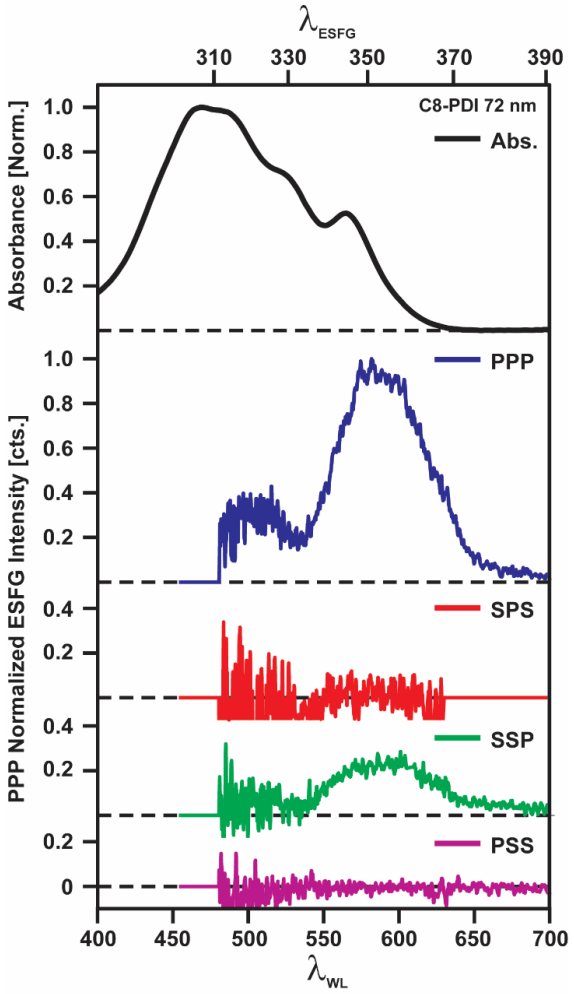


**Figure 6-4**: Comparison of 72 nm C8-PDI ESFG vs absorption. ESFG spectra normalized to PPP spectra

We can again use the intensity of the different polarization experiments to determine details about the morphology of the interface. For the C8-PDI, the strongest spectrum (that depends on a single nonlinear susceptibility term) is the SSP polarization combination. This indicates that that C8-PDI molecule stands perpendicular to the surface of the substrate (parallel to sample normal). The strength of the PPP spectrum corroborates the interpretation. Here, unlike for C1-PDI, the transition dipole stands normal to the

surface of the sample, thus the strength of the $\chi_{ZZZ}$ can be explained with the resonant transition dipole, as the higher polarizability now likely lies along the plane of the sample.

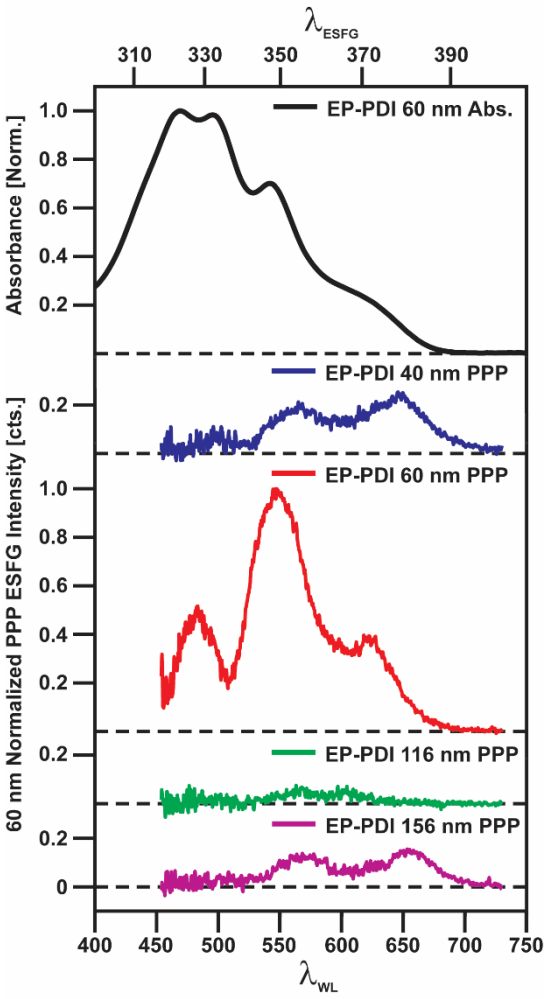


**Figure 6-5**: Comparison of EP-PDI PPP ESFG vs absorption. ESFG spectra normalized to 60 nm spectra

For the C1-PDI and C8-PDI, the ESFG spectra for each polarization combination was shown for a chosen film thickness that is representative of a series of films measured as a function of thickness. However, moving final derivative, EP-PDI, we see a complicated picture as a function of thickness (Figure 6-5), specifically for the 60 nm EP-

PDI film. Focusing on the 40 nm, 116 nm, and 156 nm PPP spectra, the EP-PDI ESFG spectra are comparable to the C1-PDI and C8-PDI. We see a reduction in the number of peaks that comprise the spectra compared to the electronic absorption spectrum, again from four to two. For the 40 nm and 156 nm films, we also see a red shift in the peaks, occurring at $\lambda_{WL}$ = 648 nm and 567 nm for the 40 nm film, with $\lambda_{WL}$ = 655 nm and 570 nm for the 156 nm film. Conversely, while the 116 nm film retains the two-peak structure of the others, they occur at $\lambda_{WL}$ = 604 nm and $\lambda_{WL}$ = 568 nm. While the high energy peak similarly placed with the others, the low energy peak is blue shifted approximately 50 nm from those of the 40 nm and 156 nm, and by 30 nm of the low energy peak in the absorption spectrum at $\lambda_{WL}$ = 630 nm. Briefly, the SSP spectra for these three films are negligible, as are the PSS and SPS spectra for all four films, and therefore these polarization combinations are not shown.

Moving to the 60 nm EP-PDI film, we see a drastic difference in the structure of the PPP spectrum relative to those of the other EP-PDI samples. Here, we see three strong, distinct peaks in the ESFG spectrum occurring at, from low to high energy, $\lambda_{WL}$ = 622 nm, 548 nm, and 485 nm. The two low energy peaks align very well with those in the absorption spectrum at $\lambda_{WL}$ = 630 nm and 585.5 nm, while the high energy peak falls between the peaks in the electronic absorption at $\lambda_{WL}$ = 501nm and 472 nm. Additionally, while the other EP-PDI films show no SSP signal for the experimental conditions used here, the 60 nm film has a weak two peak structure at approximately $\lambda_{WL}$ = 635 nm and 588 nm (Figure 6-6).

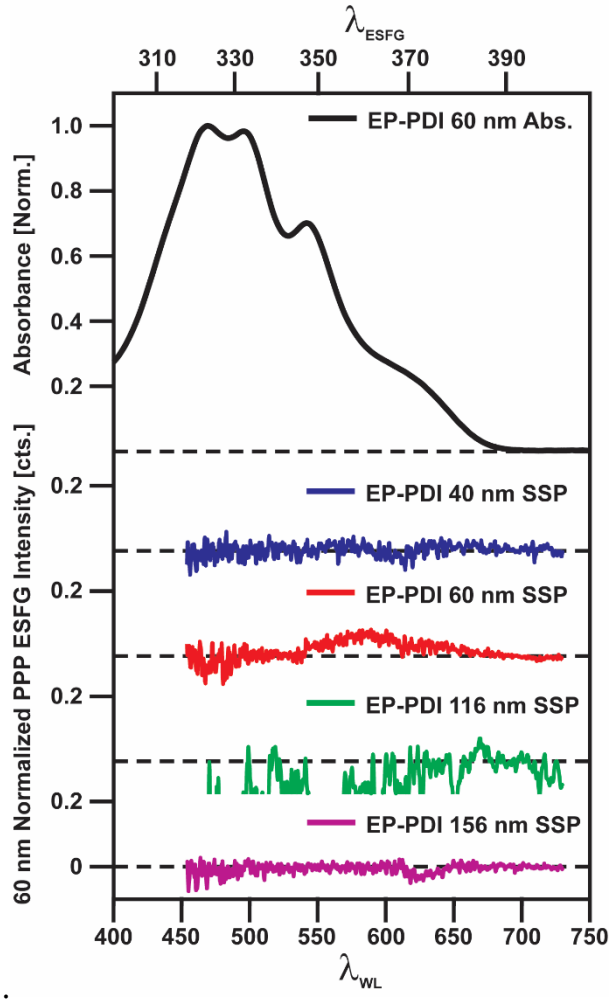


**Figure 6-6**: Comparison of EP-PDI SSP ESFG vs absorption. ESFG spectra normalized to 60 nm PPP spectra

After considering the film ESFG data as two groups, they are at a glance difficult to rationalize. The strong, well separated three peak structure of the 60 nm EP-PDI spectra seem vastly different from those of the 40 nm and 116 nm spectra. However, if we take a close look at the 40 nm PPP spectra, it's possible to see a weak third peak located at $\lambda_{WL}$ = 499 nm. Looking at the relative peak intensity for each spectrum, in the 40 nm and 156 nm film the lowest energy peak is the strongest, while for the 60 nm spectra the strongest is instead the middle peak, and in the 116 nm spectra they are approximately equal.

Examining these as a function of thickness paints a picture where instead of what appear to be strong shifts from one film to the next could instead could be explained through optical thin film interefence.

If we take the 40 nm PPP spectra as three peaks, they grow and blue shift as a function of thickness to the 60 nm spectra, and slightly change the peak ratios from the reddest being strongest to instead the middle peak. From there, the film growth leads the optical interference to reduce the peak intensity as we grow to the 116 nm film. This will readily be shown as consistently a trough in the ESFG spectra for PDI. Finally, we grow to a recurrence in the oscillatory interference pattern when we reach the 156 nm film, where the peaks are growing in strength again and the reddest peak is the strongest. To determine if this scenario is consistent with how the ESFG signal scales as a function of thickness, we are currently working to fill gaps in the thickness series for the EP-PDI film data set and to model these optical interference effects with the current set of data available. Finally, we can describe the EP-PDI morphology in a similar fashion to that of the C1-PDI and C8-PDI data. As the only polarization combinations that provide meaningful intensity are the PPP and SSP combinations, we can again say that the EP-PDI molecules likely stand vertically on the substrate surface at the interface.

Looking at the combination of data for the C1-PDI, C8-PDI, and the EP-PDI, we have shown that in each case the interfacial DoS is drastically different from that of the bulk film and varies between derivatives. Additionally, we have demonstrated our ability to distinguish morphological differences at the interface for three derivatives of PDI molecule that have only subtle changes to the base molecule. We propose that the changes in the interfacial density of states for these molecules are likely due to slight modifications of the slip-stack arrangement at the interface compared to the bulk of these films, which modify the intermolecular coupling terms within a PDI stack. Additionally, there is

possible evidence for ESFG signals originating from monomeric PDI molecules at the interface. If we compare the solution spectra for each of the three PDI derivatives, there is very little difference. Each has their strongest peak at approximately $\lambda_{WL}$ = 530 nm, though they shift drastically when moved into the solid state. In the ESFG spectra for each of the PDI derivatives, there is a peak that occurs at a common location of around $\lambda_{WL}$ = 500 nm to 520 nm. This could be due to contributions to the ESFG spectra from mostly separated PDI molecules at the interface, with difference in the location of the monomer peak due to subtle changes in the dielectric environment for each molecular system as well as slight difference in the optical thin film interference.

### 6.5: Interference Modeling PDI Derivatives

As discussed in Chapter 5, the PDI films have two ESFG active interfaces that can cause an interference beating pattern in the measured ESFG spectra as the film grows. We can use this thin film interreference to our advantage to extract the molecular response of each interface by the thin film modeling system we developed in Chapter 3. The fit data is generated using the modeling system described in Chapter 3 with Matlab's constrained minimization algorithm incorporating a homebuilt random restart method. The free-floating parameter for the fitting routine is the nonlinear susceptibility, $\chi^{(2)}$, for each interface, which we modeled as a sum of 3 Gaussians for each interface. The Gaussians used for the susceptability are constrained such that they share the same central wavelength and line width for each polarization and interfacebut are allowed to change amplitude freely.

Figure 6-7 compares the measured ESFG spectra for the SPS polarization combination of C1-PDI films measured at thickness ranging from ~20 nm to ~200 nm. Looking at the measured ESFG spectra (Figure 6-7 top) we see the first strong ESFG signal

at ~50 nm, the first trough at ~110 nm, and a recurrence at ~140 nm for the main peak at $\lambda_{ESFG}$ = 355 nm, with a weak peak at $\lambda_{ESFG}$ = 325 nm that is only present for the ~50 nm film. The thin film modeling fit (Figure 6-7 middle) agrees well with experiment, with peaks and valleys largely occurring at the same film thickness as that of the experiment. This is easily seen by looking at the bottom of Figure 6-7, where we plot the ESFG intensity as a function of thickness after taking a sum across the $\lambda_{ESFG}$ axis, where the largest discrepancies between experiment and fit occur at the depth of the trough near ~100 nm and the flat ESFG intensity in the experiment moving from ~155 nm to ~200 nm.

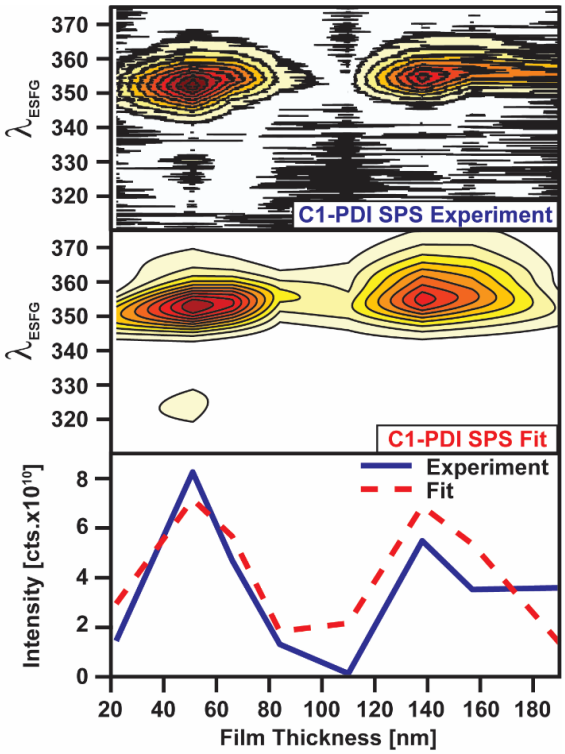


**Figure 6-7**: Comparison of SPS ESFG spectra to interference model as a function of film thickness for C1-PDI films (Top) Experiment (Middle) Theory (Bottom) Comparison as a function of film thickness after taking the sum across the $\lambda_{ESFG}$ axis for experiment (blue line) and model fit (red, dashed line)

Moving to Figure 6-8 we show the same comparison as in Figure 6-7 but show the PPP polarization ESFG spectra instead. The model fit agrees admirably with the experiment for the PPP polarization combination, with peaks that occur in similar thickness regions to that of the SPS combination. Looking at the bottom of Figure 6-8 we see that unlike SPS our peaks and troughs for the fit match well with that of experiment to include the higher thickness films. While the SSP and PSS polarization combinations for ESFG were measured and fit, they are weak compared to the polarization combinations shown here and are therefore not shown.

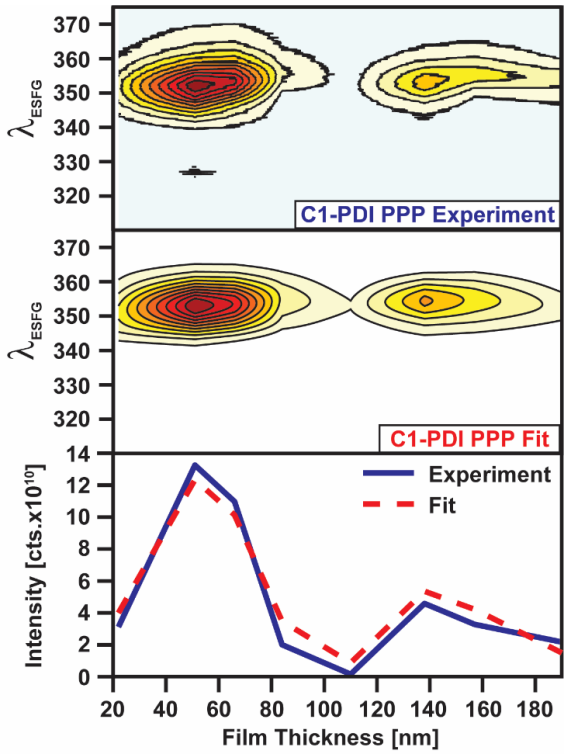


**Figure 6-8**: Comparison of PPP ESFG spectra to interference model as a function of film thickness for C1-PDI films (Top) Experiment (Middle) Theory (Bottom) Comparison as a function of film thickness after taking the sum across the $\lambda_{ESFG}$ axis for experiment (blue line) and model fit (red, dashed line)

By separating the thin film interference effects from the molecular response at each interface, we can extract the contribution to the measured ESFG spectra from each interface. In Figure 6-9 we show the extracted imaginary portion of $\chi^{(2)}$ for each interface in a film as a function of the element probed by the polarization conditions above. Note that the gaussian functions are the basis set for the $\chi^{(2)}$ response, rather than the response's fundamental physical representation. As such, it is their sum that forms a line shape that is representative of the molecular response at the interface and may be more complicated than just three peaks. This is somewhat different from vibrational modeling, which typically uses lorentzians as the fundamental representation for different vibrational modes due to their relatively well separatable nature.

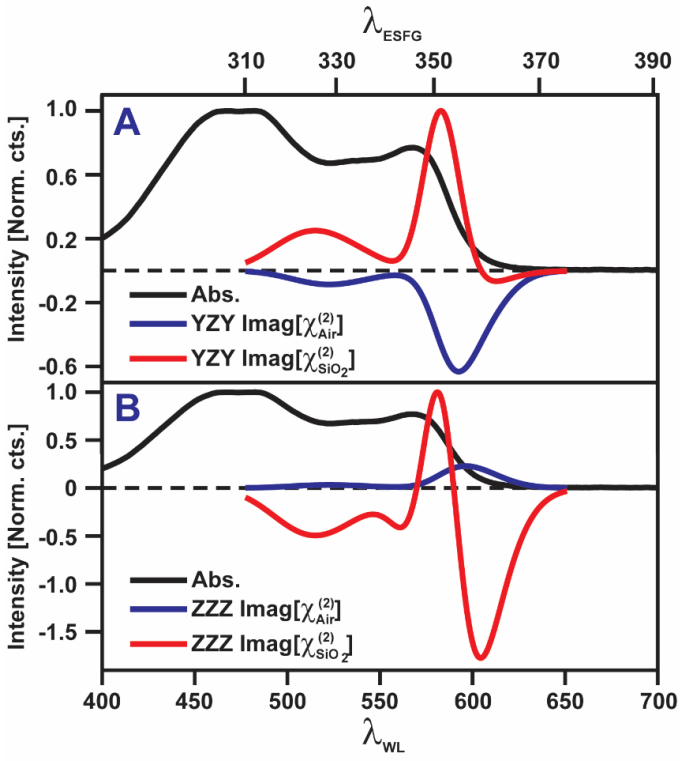


**Figure 6-9**: Comparison of the imaginary portion of extracted $\chi^{(2)}$ for the Air:C1-PDI (blue) and C1-PDI:$SiO_2$ (red) interfaces (A) Imaginary portion of $\chi_{yzy}$ (B) Imaginary portion for $\chi_{zzz}$

Figure 6-9A shows the imaginary portions for $\chi_{yzy}$ against the electronic absorption spectrum of a 51 nm C1-PDI film, with the Air:C1-PDI in blue and the C1-PDI:$SiO_2$ interface in red. For the two strong peaks in $\chi_{yzy}$, the first is centered at ~ $\lambda_{WL}$ = 580 nm, and aligns well with the strong peak in the experimental spectrum (Figure 6-3, red), as does the higher energy peak at ~ $\lambda_{WL}$ = 520 nm. There is also an additional, weak peak at low energy (~ $\lambda_{WL}$ = 605 nm) that contributes minimally to the spectra. Of note, the strength of $\chi^{(2)}$ from the C1-PDI:$SiO_2$ is higher than that of Air:C1-PDI. This likely indicates a higher degree of order at the burried C1-PDI:$SiO_2$ that is lost as the films grow, with molecules at the C1-PDI:$SiO_2$ lying more directly within the plain of the sample than those at the Air:C1-PDI interface.

Figure 6-9B shows the same comparison as in A, but instead for the $\chi_{zzz}$ susceptability element. Here, we see that once again the C1-PDI:$SiO_2$ is stronger, but we also see a more complicated structure. While the Air:C1-PDI is similar to that for $\chi_{yzy}$ (though oppositely signed), the C1-PDI:$SiO_2$ appears to have additional peaks, with a fourth appearing at ~ $\lambda_{WL}$ = 560 nm. Additionally, while the $\chi_{yzy}$ element for the C1-PDI:$SiO_2$ interface did flip from positive to negative (for the weak, lowest energy peak), here we see a large flip in the middle of the spectra for the peak at ~ $\lambda_{WL}$ = 580 nm. First, while the flip in sign for the Air:C1-PDI and C1-PDI:$SiO_2$ interfaces when comparing $\chi_{yzy}$ and $\chi_{zzz}$ may seem surprising, it is important to remember that they are probing different mappings for the molecular dipole as $\chi_{yzy} = \alpha_{yz}*\mu_y$ and $\chi_{zzz} = \alpha_{zz}*\mu_z$, and as such they need not have the same sign for the same interface. The additional complicated structure for the $\chi_{zzz}$ elment likely indicates a much more complicated interaction of the polarizabilty with that of the excitaion dipole of the molule. As the C1-PDI packs with the excitation axis of of the molecule lying in the plain of the film, the long stacks these molecules form should largely be normal to the sample surface. This is also likely to be the direction with the

strongest polarizability for the material system through the face-on π-π stacking of the strongly coupling PDI molecules, and could cause the polarizability term that is normal to the film surface to be strong, leading to a more complicated picture for the extracted $\chi_{zzz}$ term. The change in sign for certain features of this extracted spectra could indicate non-equivalent sites within the polycrystaline film that causes phase flip for electronic transitions at a different site within the crystal, similar to the well-known Davydov splitting that occurs in various PDI derivatives and other organic molecules. We are currently working to fit the ESFG spectra for the other PDI derivatives.

### 6.6: Conclusion

In conclusion, we have measured the ESFG spectra of three different derivatives of PDI molecule, the C1-PDI, C8-PDI, and the EP-PDI. We have found that not only is the DoS different at the interface relative to the bulk for each derivative, but we are able to detect morphological differences in the way each derivative pack at the interface through polarization control of our ESFG spectrometer. For the C1-PDI, we find that the molecule primarily lies along the surface of the sample substrate, while the C8-PDI and the EP-PDI stand largely vertically on the substrate. We have also proposed a cause for the drastic changes in the ESFG spectra we see as a function of thickness for the EP-PDI molecule. We have shown evidence that could suggest that for the PDI class of molecules monomers at the interface could contribute to the measured ESFG signal and extracted the contribution to the ESFG spectra for each interface and posed possible explanations for the complicated structure presented in the $\chi_{zzz}$ spectra for the C1-PDI:$SiO_2$ interface.

## 6.7: Chapter References


(1) Lewis, N. S. Research Opportunities to Advance Solar Energy Utilization. *Science* **2016**, *351* (6271), aad1920–aad1920.

(2) Rao, A.; Friend, R. H. Harnessing Singlet Exciton Fission to Break the Shockley–Queisser Limit. *Nat. Rev. Mater.* **2017**, *2*, 17063.

(3) Futscher, M. H.; Rao, A.; Ehrler, B. The Potential of Singlet Fission Photon Multipliers as an Alternative to Silicon-Based Tandem Solar Cells. *ACS Energy Lett.* **2018**, *3* (10), 2587–2592.

(4) Berkelbach, T. C.; Hybertsen, M. S.; Reichman, D. R. Microscopic Theory of Singlet Exciton Fission. I. General Formulation. *J. Chem. Phys.* **2013**, *138* (11), 114102.

(5) Casanova, D. Theoretical Modeling of Singlet Fission. *Chem. Rev.* **2018**, *118* (15), 7164–7207.

(6) Farag, M. H.; Krylov, A. I. Singlet Fission in Perylenediimide Dimers. *J. Phys. Chem. C* **2018**, *122* (45), 25753–25763.

(7) Smith, M. B.; Michl, J. Singlet Fission. *Chem. Rev.* **2010**, *110* (11), 6891–6936.

(8) Gish, M. K.; Pace, N. A.; Rumbles, G.; Johnson, J. C. Emerging Design Principles for Enhanced Solar Energy Utilization with Singlet Fission. *J. Phys. Chem. C* **2019**.

(9) Dexter, D. L. Two Ideas on Energy Transfer Phenomena: Ion-Pair Effects Involving the OH Stretching Mode, and Sensitization of Photovoltaic Cells. *J. Lumin.* **1979**, *18–19*, 779–784.

(10) Piland, G. B.; Burdett, J. J.; Hung, T.-Y.; Chen, P.-H.; Lin, C.-F.; Chiu, T.-L.; Lee, J.-H.; Bardeen, C. J. Dynamics of Molecular Excitons near a Semiconductor Surface Studied by Fluorescence Quenching of Polycrystalline Tetracene on Silicon. *Chem. Phys. Lett.* **2014**, *601*, 33–38.

(11) MacQueen, R.; Liebhaber, M.; Niederhausen, J.; Mews, M.; Gersmann, C.; Jäckle, S.; Jäger, K.; Tayebjee, M. J. Y.; Schmidt, T. W.; Rech, B.; et al. Crystalline Silicon Solar Cells with Tetracene Interlayers: The Path to Silicon-Singlet Fission Heterojunction Devices. *Mater. Horiz.* **2018**.

(12) Pazos-Outón, L. M.; Lee, J. M.; Futscher, M. H.; Kirch, A.; Tabachnyk, M.; Friend, R. H.; Ehrler, B. A Silicon–Singlet Fission Tandem Solar Cell Exceeding 100% External Quantum Efficiency with High Spectral Stability. *ACS Energy Lett.* **2017**, *2* (2), 476–480.

(13) Chen, Y.; Tamblyn, I.; Quek, S. Y. Energy Level Alignment at Hybridized Organic?Metal Interfaces: The Role of Many-Electron Effects. *J. Phys. Chem. C* **2017**.

(14) Hestand, N. J.; Tempelaar, R.; Knoester, J.; Jansen, T. L. C.; Spano, F. C. Exciton Mobility Control through Sub − Å Packing Modifications in Molecular Crystals. *Phys. Rev. B* **2015**, *91* (19).

(15) Hestand, N. J.; Spano, F. C. Molecular Aggregate Photophysics beyond the Kasha Model: Novel Design Principles for Organic Materials. *Acc. Chem. Res.* **2017**, *50* (2), 341–350.

(16) Le, A. K.; Bender, J. A.; Arias, D. H.; Cotton, D. E.; Johnson, J. C.; Roberts, S. T. Singlet Fission Involves an Interplay between Energetic Driving Force and Electronic Coupling in Perylenediimide Films. *J. Am. Chem. Soc.* **2018**, *140* (2), 814–826.

(17) Coropceanu, V.; Cornil, J.; da Silva Filho, D. A.; Olivier, Y.; Silbey, R.; Brédas, J.-L. Charge Transport in Organic Semiconductors. *Chem. Rev.* **2007**, *107* (4), 926–952.

(18) Ryno, S. M.; Fu, Y.-T.; Risko, C.; Brédas, J.-L. Polarization Energies at Organic–Organic Interfaces: Impact on the Charge Separation Barrier at Donor–Acceptor Interfaces in Organic Solar Cells. *ACS Appl. Mater. Interfaces* **2016**, *8* (24), 15524–15534.

(19) Ryno, S. M.; Risko, C.; Brédas, J.-L. Impact of Molecular Orientation and Packing Density on Electronic Polarization in the Bulk and at Surfaces of Organic Semiconductors. *ACS Appl. Mater. Interfaces* **2016**, *8* (22), 14053–14062.

(20) Austin, A.; Hestand, N. J.; McKendry, I. G.; Zhong, C.; Zhu, X.; Zdilla, M. J.; Spano, F. C.; Szarko, J. M. Enhanced Davydov Splitting in Crystals of a Perylene Diimide Derivative. *J. Phys. Chem. Lett.* **2017**, *8* (6), 1118–1123.

(21) Vasseur, K.; Rolin, C.; Vandezande, S.; Temst, K.; Froyen, L.; Heremans, P. A Growth and Morphology Study of Organic Vapor Phase Deposited Perylene Diimide Thin Films for Transistor Applications. *J. Phys. Chem. C* **2010**, *114* (6), 2730–2737.

(22) Takahashi, Y.; Mikasa, T.; Hayakawa, K.; Yokokura, S.; Hasegawa, H.; Harada, J.; Inabe, T. Fabrication of Conducting Thin Films on the Surfaces of 7,7,8,8-Tetracyanoquinodimethane Single-Component and Charge-Transfer Complex Single Crystals: Nucleation, Crystal Growth, Morphology, and Charge Transport. *J. Phys. Chem. C* **2016**, *120* (31), 17537–17545.

(23) Griffin, M. P.; Gearba, R.; Stevenson, K. J.; Vanden Bout, D. A.; Dolocan, A. Revealing the Chemistry and Morphology of Buried Donor/Acceptor Interfaces in Organic Photovoltaics. *J. Phys. Chem. Lett.* **2017**, 2764–2773.

(24) Humbert, C.; Dreesen, L.; Nihonyanagi, S.; Masuda, T.; Kondo, T.; Mani, A. A.; Uosaki, K.; Thiry, P. A.; Peremans, A. Probing a Molecular Electronic Transition by Two-Colour Sum-Frequency Generation Spectroscopy. *Appl. Surf. Sci.* **2003**, *212–213*, 797–803.

(25) Lin, C.-K.; Lei, J.; Lin, Y.-D.; Lin, S. H. Electronic Sum-Frequency Generation (ESFG) Spectroscopy: Theoretical Formulation of Resonances with Symmetry-Allowed and Symmetry-Forbidden Electronic Excited States. *Mol. Phys.* **2017**, 1–10.

(26) Moon, A. P.; Pandey, R.; Bender, J. A.; Cotton, D. E.; Renard, B. A.; Roberts, S. T. Using Heterodyne-Detected Electronic Sum Frequency Generation To Probe the Electronic Structure of Buried Interfaces. *J. Phys. Chem. C* **2017**, *121* (34), 18653–18664.

(27) Pandey, R.; Moon, A. P.; Bender, J. A.; Roberts, S. T. Extracting the Density of States of Copper Phthalocyanine at the $SiO_2$ Interface with Electronic Sum Frequency Generation. *J. Phys. Chem. Lett.* **2016**, *7* (6), 1060–1066.

(28) Le, A. K.; Bender, J. A.; Roberts, S. T. Slow Singlet Fission Observed in a Polycrystalline Perylenediimide Thin Film. *J. Phys. Chem. Lett.* **2016**, *7* (23), 4922–4928.

(29) Eaton, S. W.; Shoer, L. E.; Karlen, S. D.; Dyar, S. M.; Margulies, E. A.; Veldkamp, B. S.; Ramanan, C.; Hartzler, D. A.; Savikhin, S.; Marks, T. J.; et al. Singlet Exciton Fission in Polycrystalline Thin Films of a Slip-Stacked Perylenediimide. *J. Am. Chem. Soc.* **2013**, *135* (39), 14701–14712.

(30) Kazmaier, P. M.; Hoffmann, R. A Theoretical Study of Crystallochromy. Quantum Interference Effects in the Spectra of Perylene Pigments. *J. Am. Chem. Soc.* **1994**, *116* (21), 9684–9691.

(31) Hädicke, E.; Graser, F. Structures of Eleven Perylene-3,4:9,10-Bis(Dicarboximide) Pigments. *Acta Crystallogr. C* **1986**, *42* (2), 189–195.

# Chapter 7: Probing the Electronic Structure of Buried Interfaces Using Heterodyne-Detected Electronic Sum Frequency Generation[5]

## 7.1: Introduction

While electronic sum frequency generation (ESFG) is a useful probe of interfacial electronic structure and morphology, measuring and interpreting ESFG signals from OSC thin films presents a few specific challenges. First, as ESFG is produced by only a small number of monolayers near an interface, the signals generated in this technique are inherently weak, leading to the need for long collection times to achieve a reliable signal-to-noise ratio. Secondly, though ESFG signals are intrinsically interface-specific, an organic semi-conductor (OSC) film has at minimum two interfaces that can each produce an ESFG signal. This complicates the interpretation of the measurement for the buried interface where charge and energy transfer take place compared to the air exposed signal. As discussed in Chapter 3, signals emitted by these two interfaces can interfere with each other, making the extraction of information exclusive to the buried interface difficult.[1–5] Finally, the signal measured in an ESFG experiment contains no information related to the *sign* of the induced polarization between an OSC and its underlying substrate. This reflects that a measurement of the ESFG field emitted by a sample, $\vec{E}_{Samp}$, using a square law detector like a CCD measures the field's intensity rather than its amplitude and phase:

$$I_{ESFG} \propto |\vec{E}_{Samp}|^2 \propto |\chi^{(2)}|^2. \quad (7\text{-}1)$$

In Equation 7-1, $\chi^{(2)}$ is the second-order nonlinear susceptibility of an interface. The sign of $\chi^{(2)}$ reports on the direction of the induced polarization between an OSC and

[5]Previously published as Moon, A. P.; Pandey, R.; Bender, J. A.; Cotton, D. E.; Renard, B. A.; Roberts, S. T. Using Heterodyne-Detected Electronic Sum Frequency Generation to Probe the Electronic Structure of Buried Interfaces. *J. Phys. Chem. C* **2017**, *121*(34), 18653-18664. My contributions to this paper include helping collect ESFG spectra, building the ESFG spectrometer, creation of initial thin film modeling software, consultation of modeling and fitting ESFG spectra, and interpreting the spectra and writing the paper with my colleagues.

the substrate, yet the intensity of the ESFG signal depends upon the square of this term.[6–8] When only the intensity of an emitted ESFG field is measured, information regarding the sign of the induced polarization giving rise to the ESFG field is lost. However, knowledge of such information is critical as it can describe how OSC molecules polarize when placed into contact with a high-dielectric inorganic semi-conductor (ISC), leading to band bending of both materials at the junction.[8,9] We refer to ESFG signals measured in this manner, which lose phase information, as "direct ESFG".

To overcome the shortcomings of direct ESFG, our group has implemented a heterodyne detection scheme (HD-ESFG) for recording ESFG spectra. In contrast to a direct ESFG measurement where the WL and upconversion beams simply generate an ESFG field from a sample, in an HD-ESFG experiment these beams are also used to create a reference field, referred to as a local oscillator (LO), by focusing them onto a non-centrosymmetric material that produces a strong, non-resonant ESFG signal. The signal field produced by a sample is then spatially overlapped with the LO, $\vec{E}_{LO}$, and spectrally detected.[6–8,10–19] Interference between the strong LO and weaker signal gives rise to a cross term that oscillates at the phase difference between these two fields (Equation 7-2):[7]

$$I_{HD-ESFG} \propto |\vec{E}_{Samp}\vec{E}_{LO}|^2 = |\vec{E}_{Samp}|^2 + |\vec{E}_{LO}|^2 + 2|\vec{E}_{Samp}||\vec{E}_{LO}|cos(\phi_{Samp} - \phi_{LO}) \quad (7\text{-}2)$$

Fourier filtering of the data selectively isolates this cross term. If the LO phase and amplitude are known, the phase and amplitude of the ESFG signal can be directly determined from the cross term. Importantly, as we demonstrate below, the retrieval of the ESFG signal phase from a thin OSC film provides an additional constraint that aids in separating signal contributions that arise from the film's outer and buried interfaces. Moreover, as the cross-term scales linearly in both the ESFG signal field and the LO field,

the LO can amplify weak ESFG fields, reducing the data collection times needed to obtain signals above the shot-noise limit.

We employ HD-ESFG to study the buried interfacial structure of thin films of N−N′-dimethyl-3,4,9,10-perylenedicarboximide (C1-PDI) that have been vapor-deposited on fused quartz. C1-PDI is a member of the larger family of perylenediimide molecules that have been examined as promising candidates for SF sensitizers for photovoltaic cells and other light harvesting schemes.[20–23] Below, we describe a simplistic scheme for constructing an HD-ESFG spectrometer that makes use of common-path optics to minimize phase jitter between the sample and LO fields during measurements. This spectrometer shows minimal drift over multiple hours and the scheme for its implementation should be readily amenable to integration with existing ESFG spectrometers. We also show that HD-ESFG aids in the detection of weak ESFG features and that the inclusion of spectral phase in an optical interference model allows for a more accurate reconstruction of the $\chi^{(2)}$ of a buried OSC interface. We find that HD-ESFG spectra of C1-PDI thin films are significantly red-shifted relative to their bulk absorption spectra. This result highlights the sensitivity of HD-ESFG to the electronic density of states (DoS) of buried OSC interfaces and suggests its future utility in studying exciton and charge extraction from OSC thin films.

### 7.2: Materials Characterization

C1-PDI was purchased from Sigma-Aldrich (98% purity) and used as received. Uniform thickness C1-PDI films were vapor-deposited onto fused quartz ($SiO_2$) plates (GM Associates, 1/16” thickness) using a UHV thermal deposition chamber (AMOD PVD system, Ångström Engineering) with a base pressure of ~$5 \times 10^{-7}$ Torr and a deposition rate of 1 Å/s. Substrates were sonicated sequentially in chloroform, toluene, and

isopropanol, rinsed with methanol, and dried under $N_2$ prior to thermal deposition. Variable angle spectral ellipsometry (M-2000, J. A. Woollam) was used to determine the thickness of vapor-deposited films as well as their optical constants. Samples for these measurements consisted of films that were grown on top of n-type Si(100) substrates with a native oxide layer. These films were produced concomitantly with films deposited on $SiO_2$ for ESFG measurements to ensure thickness uniformity for both samples. Si substrates were cleaned using a procedure identical to that for $SiO_2$ plates prior to film deposition. All of the ESFG results presented in this Chapter were measured for a C1-PDI film found to have a thickness of 52 nm via ellipsometry. Transmission and reflection spectra of sample films were recorded using a UV-Vis spectrometer with an integrating sphere attachment (Shimadzu UV-2600). Absorption spectra that appear in Figures 7-2 & 7-11 have been corrected to account for reflection and scattering losses.

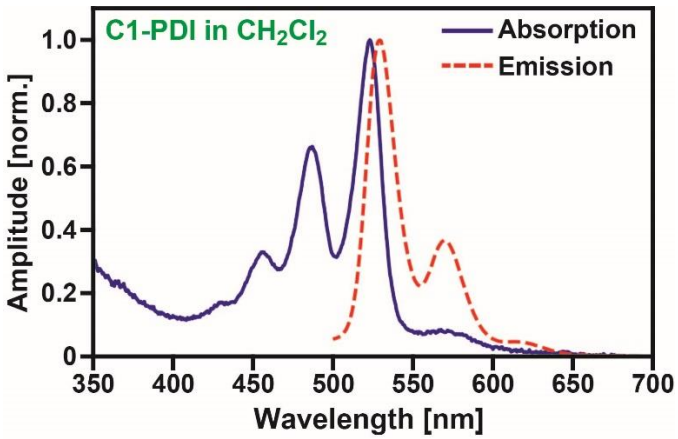


**Figure 7-1**: Absorption and fluorescence spectrum of C1-PDI in $CH_2Cl_2$.

Figure 7-1 plots the absorption and emission spectrum of C1-PDI in $CH_2Cl_2$. The absorption spectrum was obtained using a 1 cm cuvette with a UV-Vis spectrometer (Shimadzu UV-2600) while the fluorescence spectrum was collected using a Horiba Jobin Yvon Fluorolog3 fluorimeter employing a right-angle geometry. The excitation source for

emission measurements was the 402 nm portion of a Xenon lamp selected using a dispersive grating. A set of slits was used to obtain an excitation and emission-resolution bandwidth of 1 nm. The absorption spectrum of C1-PDI monomers in solution display a vibronic progression with a ~1410 $cm^{-1}$ peak spacing characteristic of the ring stretching modes of aromatic systems. In addition to this progression, a broad shoulder appears in the absorption spectrum at ~575 nm that we assign to C1-PDI aggregates due to the similarity of the spectral position of this band to the absorption edge of a vapor-deposited C1-PDI thin film (Figure 7-2). The appearance of this feature is not surprising given C1-PDI's limited solubility in $CH_2Cl_2$. Examining the fluorescence spectrum of C1-PDI, we observe a modest Stokes shift and a vibronic progression that largely mirrors that observed in the molecule's absorption spectrum.

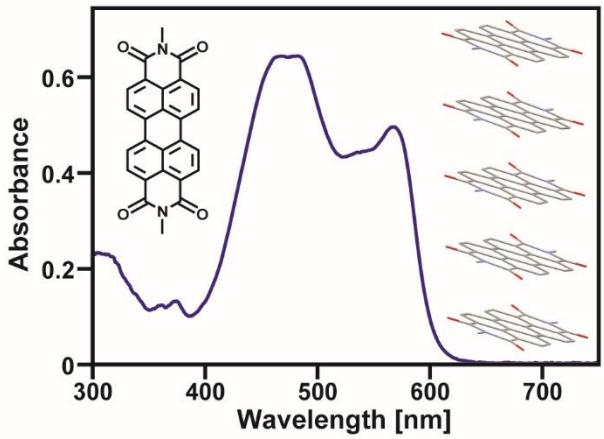


**Figure 7-2:** Linear absorption spectrum of a 52 nm C1-PDI film (structure inset). Films arrange in a slip-stacked manner (right inset).[24]

Figure 7-2 plots the linear absorption spectrum of a 52 nm C1-PDI film vapor-deposited on $SiO_2$. The film's spectrum distinctly differs from that of monomeric C1-PDI, displaying two broad peaks at 474 and 568 nm and a smaller shoulder at 536 nm.

Characterization of the C1-PDI films using XRD and AFM have already been discussed in Chapter 6 (see Figure 6-2).

### 7.3: Spectrometer for HD-ESFG

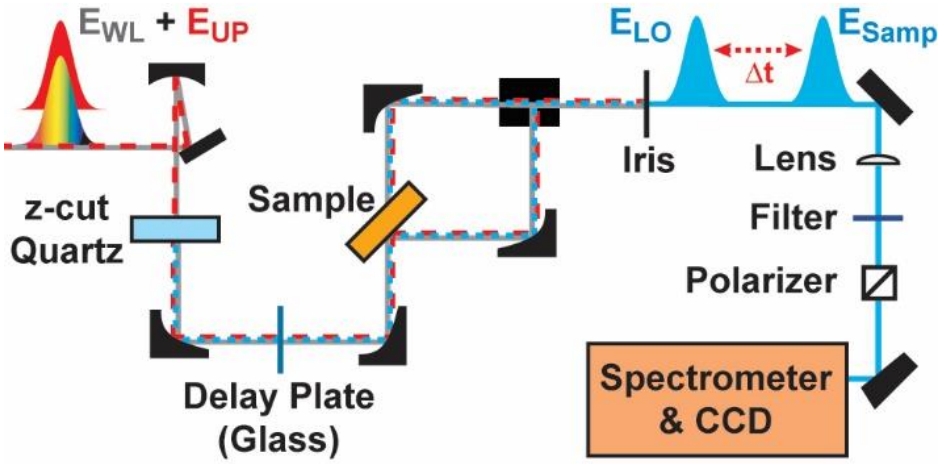


**Figure 7-3:** Experimental layout for HD-ESFG.

Our experimental setup for HD-ESFG measurements (Figure 7-3) was built as an addition to our spectrometer for direct ESFG (described in detail in Chapter 4). Briefly, a femtosecond Ti:sapphire regenerative amplifier (Coherent Legend Duo Elite, 3 kHz, 4.5 mJ) was used to generate a 90 fs pulse centered at 804 nm with a bandwidth of 160 $cm^{-1}$ (FWHM). A small portion of the amplifier output (0.1 mJ) was focused into a water flow cell to generate a white light supercontinuum (WL). The WL was collimated and passed through a pair of spectral filters to reduce its bandwidth to a spectral range extending from 450 nm to 800 nm. A second portion of the amplifier output was used as the narrowband upconversion pulse.

Prior to the sample, the upconversion and WL beams were focused using a 15 cm focal length concave mirror in a noncollinear geometry into a 20 μm thick piece of z-cut quartz (Newlight Photonics). As z-cut quartz is a noncentrosymmetric material, it generates

a nonresonant, bulk-allowed ESFG signal that serves as the LO field for HD-ESFG measurements. Following the quartz piece, the transmitted LO, WL, and upconversion fields were collimated with a 90º off-axis parabolic mirror (A50331AL, Newport). Following beam collimation, there was enough spatial separation between the three beams to introduce a silica microscope coverslip with a thickness of 145 μm (Fisherbrand) into the path of the LO exclusively. This coverslip acts as a delay plate that slows the time of arrival of the LO at the sample relative to the WL and upconversion fields by ~ 360 fs. Following the delay plate, all three fields are focused using a second 90º off-axis parabolic mirror onto a sample film oriented at 45º with respect to the plane of the incident beams. Here, the WL and upconversion fields drive generation of an ESFG field form the sample that, due to phase matching considerations, is emitted in a direction collinear with the LO. Following the sample, a third 90º off-axis parabolic mirror collimates both the LO and signal fields reflected or transmitted by the sample. These fields are then passed through an iris to remove the upconversion and WL fields, followed by a spectral filter (UG11, SCHOTT) to remove any scattered upconversion or WL photons that travel collinearly with the two ESFG fields. Prior to being focused onto the entrance slit of a spectrometer (Acton Spectra Pro SP2500), the ESFG signal and LO fields were passed through a polarizer to select either their P or S components and a waveplate that rotates the polarization of these fields back to S-polarization due to the increased sensitivity of our spectrometer to S-polarized light. The spectrometer used a 600 grove/mm grating blazed at 300 nm (Richardson Gratings) to spectrally disperse the signal onto a liquid nitrogen cooled CCD camera (PyLoN 2KBUV, Princeton Instruments).

Typical pulse energies for the filtered WL and upconversion pulses were 2 μJ and 1 μJ, respectively. To determine if sample damage occurs during ESFG measurements, we performed a control experiment wherein ESFG spectra of a C1-PDI film were continuously

measured for a fixed time delay between the WL and upconversion fields using direct detection over the course of 30 minutes. For these measurements, the pulse energies of the WL and upconversion fields were fixed at the values quoted in the main text, 2 and 1 μJ respectively. We observe that the amplitude of the ESFG signal shows no signatures of systematic decay (Figure 7-4 A), suggesting that the film does not experience laser-induced damage under these illumination conditions.

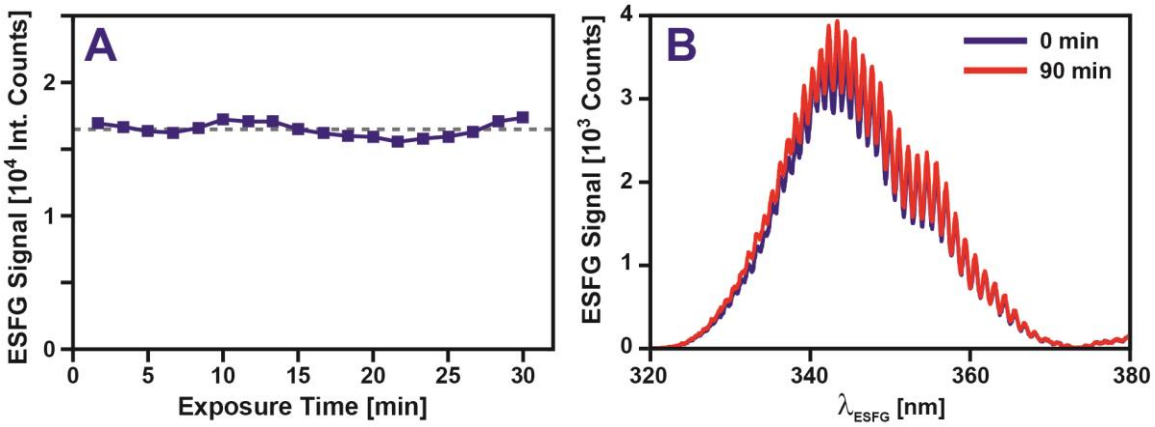


**Figure 7-4:** (A) ESFG signal intensity of a C1-PDI film continuously measured over 30 minutes. (B) Two HD-ESFG spectra of a C1-PDI film for a WL/upconversion pulse time delay of $\Delta t = 0$ fs.

To examine how additional illumination by the LO affects the stability of C1-PDI films, in Figure 7-4 B we plot two HD-ESFG spectra of a 52 nm C1-PDI film. These spectra were recorded 90 minutes apart from one another. During this time interval, the same focal spot within the film experienced illumination by the WL, upconversion, and LO fields produced by a 20 μm z-cut quartz substrate. As can be seen from the data, there are no apparent changes in the amplitude of the HD-ESFG signal nor the spectral position of its fringes. This indicates that continuous illumination of a C1-PDI sample for HD-ESFG measurements at the power we quote does not damage the sample film. In addition, these results highlight the interferometric stability of our HD-ESFG spectrometer.

We note that for the experimental results reported here, the 804 nm upconversion beam is non-resonant with respect to the C1-PDI film, which enables relatively high photon fluxes to be employed for this beam without inducing film damage. Likewise, the 2 μJ power of the white light pulse is spectrally integrated across its entire bandwidth, but only a fraction of this bandwidth is directly resonant with the C1-PDI film. The excitation densities induced by this beam are not significantly different than those commonly employed in femtosecond transient absorption measurements of PDI films wherein sample damage is not found to occur.[15,16]

Each HD-ESFG spectrum reported here was collected for PPP polarization. To collect direct ESFG spectra for comparison to HD-ESFG data, the LO field was removed by placing a small beam block following the delay plate but ahead of the sample. Analogously, the spectrum of the LO was recorded by using an iris to block the WL and upconversion fields before they reached the sample. A background was collected for each scan by delaying the upconversion field by 100 ps with respect to the WL field and collecting a spectrum for the same integration time used to measure ESFG spectra.

As the WL field passes through a significant amount of dispersive material following its generation, it is chirped in time with approximately a 1.4 ps separation between its reddest and bluest frequency components. This time separation is roughly an order of magnitude longer than the pulse width of the upconversion field, ~100 fs. As ESFG is only generated when the upconversion and WL beams interact with a sample at the same time, to ensure the upconversion field has the opportunity to mix with each frequency component of the WL pulse, ESFG spectra were collected by scanning the time delay between the WL and upconversion fields using a computer-controlled delay stage (Newport XMS50). Unless otherwise noted, each ESFG spectrum in this report represents

the sum of a set of measurements wherein the time delay between the WL and upconversion fields was scanned over a range of 1.5 ps in 100 fs steps.

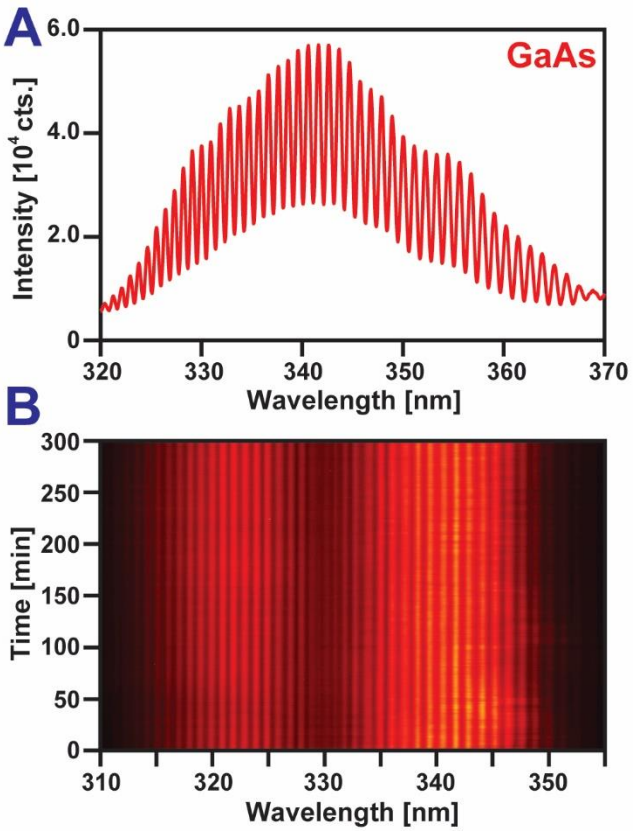


**Figure 7-5:** (A) HD-ESFG signal recorded for a GaAs(110) wafer. (B) HD-ESFG spectra of a z-cut quartz plate placed in the sample position, measured every 30 s for 5 hours. Spectral fringes show minimal evidence of motion, highlighting the phase stability of our experimental layout.

Figure 7-5 A displays the HD-ESFG spectrum of a GaAs(110) wafer recorded using the methodology outlined above. Similar to z-cut quartz, GaAs is a non-centrosymmetric material and hence generates an intense reflected ESFG signal whose spectral lineshape largely follows that of the WL pulse.[7,25] Due to interference between the ESFG fields emitted by the quartz and GaAs pieces, spectral fringes can be observed in the collected HD-ESFG spectrum. The spacing between these fringes reflects the phase difference

between the LO and GaAs signal fields, which can be adjusted by controlling the time separation between these fields via the thickness (and effective thickness via tilt) of the delay plate. As the amplitude of the GaAs ESFG field is comparable to that of the quartz-generated LO, the oscillations that result from the interference between these fields approach the theoretical limit of 50% for two equal amplitude fields.

One concern when constructing a spectrometer for optical heterodyne measurements is minimizing path-length fluctuations between the LO and signal fields, which can randomize the phase of the heterodyne signal produced by their interference. Such fluctuations are of particular concern when detecting interferograms in the ultraviolet spectral range as a path-length shift on the order of half the wavelength of the signal field will cause the sign of the detected interferogram to flip. Thus, for the signals reported here, path-length fluctuations of ~170 nm between the signal and LO during data collection will cause the HD-ESFG signal produced by their interference to average to zero.

To ensure that the distance separating the LO and ESFG signal fields generated by our HD-ESFG setup remain fixed throughout an experiment, we have used common-path optics to propagate the LO, WL, upconversion, and signal fields after generating and filtering the WL (Figure 7-3). Thus, any fluctuations in the optical path of our spectrometer will be transferred to each of these beams, holding fixed the relative phase of the signal and LO. As an illustration of this point, in Figure 7-5B we plot HD-ESFG spectra of a z-cut quartz piece placed at the sample position that were taken every 30 seconds over the course of 5 hours. Over this time span, we see that interference fringes produced between the LO and ESFG signal fields display almost no discernable drift. Comparing the first recorded spectrum to that measured after 5 hours indicates a change in phase of 0.43 radians, which corresponds to a path-length change of only ~24 nm (~$\lambda$/15) in the relative path traveled by the LO and ESFG fields over this time. Such long-term phase stability is

required for measurements that aim to detect changes in the ESFG signal intensity of a sample in response to an external stimulus, such as a time-delayed excitation pulse in transient ESFG measurements.[8,26–29]

### 7.4: Results

Phase-sensitive detection of ESFG fields produced using WL continua was previously implemented by Yamaguchi and Tahara.[7] In their setup, the WL and upconversion fields were first focused onto a sample in a reflection geometry, generating ESFG. The reflected WL, upconversion, and ESFG fields were then captured using a spherical mirror and refocused onto a GaAs(110) wafer to produce a LO field emitted in a direction collinear with the ESFG field. While this setup has been effectively used to study the structure of liquid interfaces[30–32] and monolayer films,[7] thin OSC films present significant challenges. First, as discussed in Chapters 3, thin films are known to produce signals from each of their surfaces that interfere with one another. The signal from a specific interface of interest can be isolated by measuring spectra of films of different thicknesses or by varying the angle of incidence of the WL and upconversion fields.[1–4] However, as many OSCs are highly absorbing, they can strongly modify the spectrum of the reflected WL field used to generate a LO in Yamaguchi and Tahara's scheme. This creates a complication when altering either OSC film thickness or sample tilt with respect to the WL and upconversion fields as this can modify the spectrum of the LO used for HD-ESFG detection. Secondly, producing the LO using fields reflected from a sample's surface creates a practical issue as the sample itself acts as a mirror. Slight changes in the tilt of a sample when exchanging one for another can alter beam steering onto a GaAs wafer placed after the sample, affecting the efficiency of LO generation. Lastly, GaAs itself is highly absorbing in the ultraviolet spectral range. As the signal emitted by a sample needs to be

reflected off a GaAs surface in Tahara and Yamaguchi's scheme, absorption of the signal by GaAs can negate some of the signal-to-noise gains expected from heterodyne detection.

To address the issues noted above, our experimental layout for HD-ESFG generates the LO using a transmissive z-cut quartz piece placed ahead of the sample. This layout is similar to that recently implemented by Inoue et. al.[10] and Vanselous and Petersen[11] for measuring heterodyne-detected vibrational sum frequency generation, but to our knowledge this is the first time it has been adapted to measurement of broadband HD-ESFG spectra employing a WL continuum. Generating the LO prior to the ESFG signal from a sample carries the distinct advantage that the LO's spectral profile is no longer tied to the sample film's reflectivity, ensuring each sample investigated in our layout experiences an identical LO field. Moreover, by using a transmissive geometry for generating the LO, we simplify the alignment of our HD-ESFG spectrometer as the substrate that produces the LO is no longer used as a mirror. This geometry allows us to easily change between detecting ESFG signals reflected or transmitted from a sample without the need to re-optimize LO generation.

Figure 7-6A plots the spectrum of the LO field produced by overlapping the WL and upconversion fields in a 20 μm z-cut quartz crystal alongside the spectrum of the ESFG field created by focusing these beams reflectively onto a GaAs substrate. The spectrum of the signal produced by GaAs largely follows that of the WL field and its spectral extent is ultimately limited in our setup by a bandpass filter placed after the sample that removes residual scattered light from the WL field. As the LO produced by z-cut quartz is created nonresonantly, it too should display a spectrum that tracks the WL's line shape.

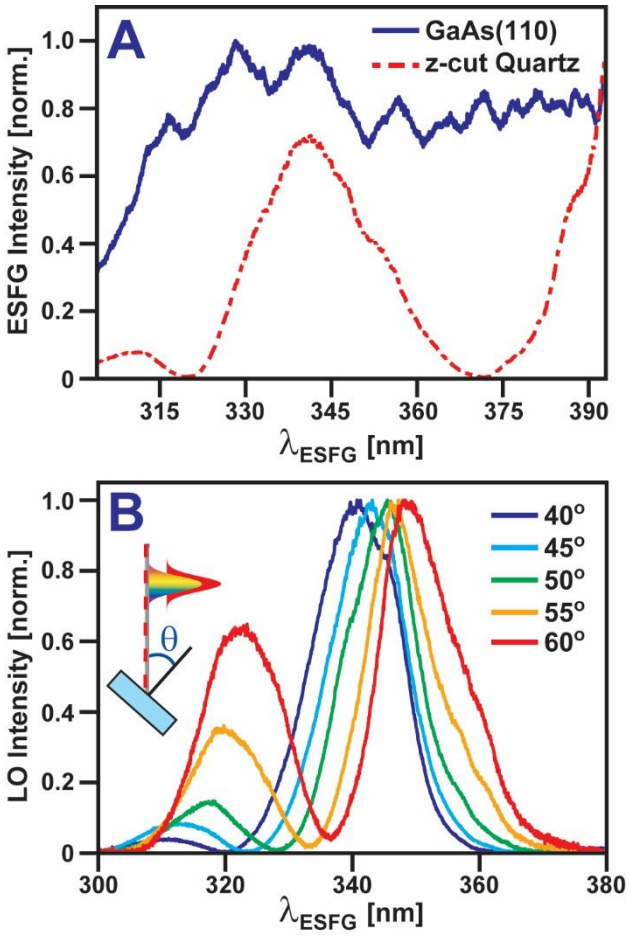


**Figure 7-6:** (A) Comparison of the spectrum of the transmitted LO field from 20 μm z-cut quartz and the direct ESFG of a GaAs(110) wafer. (B) Spectrum of the LO field as a function of the angle of incidence using 35 μm z-cut quartz.

However, the LO's spectrum is instead highly structured, showing a series of narrower peaks that resemble the WL spectrum convolved with a $sinh^2(\omega)$ function. This narrowed spectrum represents one disadvantage of using a transmissive geometry to produce the LO as the dispersion of the z-cut quartz crystal leads to temporal walk off between the ESFG field and the WL and upconversion fields as they propagate through the crystal. This leads to a phase shift between ESFG signal created at different points within the crystal that can interfere for certain wavelengths.[33] The bandwidth of the LO can be

maximized by minimizing the thickness of the crystal used to produce it[10,12] and the position of peaks within the LO spectrum can be tuned by altering the angle between it and the incident WL and upconversion fields (Figure 7-6B). Nevertheless, for the 20 μm z-cut crystal we employ here, we find that our LO has a bandwidth of ~2200 $cm^{-1}$ (FWHM of central peak), which is broad enough to span the lowest energy electronic transition of C1-PDI.

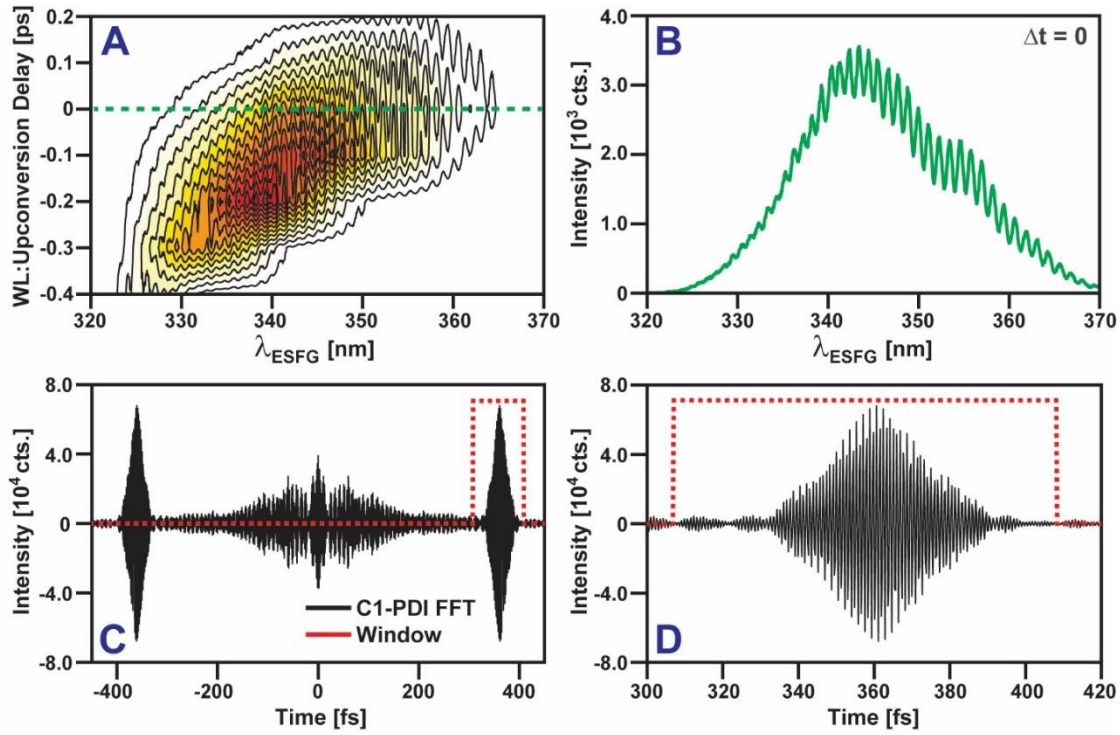


**Figure 7-7:** (A) HD-ESFG of a 52 nm C1-PDI film on $SiO_2$ as a function of the time delay between generation fields. (B) Spectral slice of the data in (A). (C) Fast Fourier Transform of (B) (black) and the window used to extract cross term (red). (D) Zoomed view of (C).

Figure 7-7A displays a contour plot showing HD-ESFG spectra measured for a 52 nm C1-PDI film as a function of the time delay between the WL and upconversion fields. As the delay between these fields is scanned, the envelope of the response undergoes a

pronounced frequency shift due to the chirp in the WL field. Oscillations are apparent in the spectrum at each time delay due to interference between the LO and ESFG field emitted by the C1-PDI film. These oscillations are highlighted in Figure 7-7B, which shows a slice through the dataset in Figure 7-7A indicated by the dashed green line. As with any heterodyne detection scheme, care must be taken in setting the intensity of the LO relative to that of the signal emitted by a sample to ensure that the measured spectrum is not dominated by the background $|\vec{E}_{LO}|^2$ contribution. In our setup, the amplitude of the LO can be tuned via in-plane rotation of the z-cut quartz crystal. Such tunability is important as the direct ESFG signal, $|\vec{E}_{Samp}|^2$, produced by a C1-PDI film is 275× **weaker** than that of a GaAs wafer. For the data in Figure 7-7, the LO intensity was maximally attenuated by rotation of the z-cut quartz, yielding an intensity ratio of 89 for $|\vec{E}_{LO}|^2/|\vec{E}_{Samp}|^2$. Decreasing this ratio further by replacing the delay plate used to temporally separate the LO and signal with similarly thin neutral density filter could in principle improve the fringe depth achieved in Figure 7-7B. Nevertheless, as constructed, our setup has enough flexibility to detect heterodyne signals from both strong (GaAs) and weak (C1-PDI) emitters.

Figure 7-7C plots the real portion of the Fourier transform of the HD-ESFG signal, which displays two intense peaks at time delays of ±360 fs as well as a broad band centered at t = 0. Looking at Equation 7-2, it is apparent that the features at ±360 fs represent the cross terms that contain the product $|\vec{E}_{Samp}||\vec{E}_{LO}|$, while the band centered at t = 0 denotes the central contributions $|\vec{E}_{LO}|^2$ and $|\vec{E}_{Samp}|^2$. We can isolate the cross term by applying a window function to the Fourier transform that selects one of the peaks at ±360 fs and subsequently performing an inverse Fourier transform.[7,13,14] We note the thickness of the glass plate used to introduce a time delay between the LO and signal fields is critical to the success of this analysis scheme. If the plate is too thin, it will not sufficiently separate the

cross term from the central signal contributions. Conversely, if the plate is too thick, it will minimize the interference between the LO and signal fields at the detector. In our implementation, we have employed a 145 μm thick glass plate that creates a delay of 360 fs between the LO and signal fields at the detector. This delay can be fine-tuned by slight alteration of the tilt of the glass plate or by replacing the plate with a pair of variable thickness wedges.[34,35]

Fourier transform filtering of the data in Figure 7-7A was used to isolate the cross term**,** whose spectrum is plotted in Figure 7-8A (black line). Plotted alongside this data is a direct ESFG spectrum of the same C1-PDI sample film recorded without the use of a LO, $|\vec{E}_{Samp}|^2$ (red line). Both sets of data were measured using a 120 s integration time and we have processed the data in a manner such that the amplitudes of the cross term and direct ESFG signal should be comparable. As expected, the HD-ESFG spectrum is more intense than the direct signal due to the additional contribution from the LO. As the LO is not spectrally flat, this contribution skews the HD-ESFG spectrum, causing it to peak at a shorter wavelength than the direct signal. This can be corrected by dividing the cross term by the amplitude of the LO. In practice, this division is achieved by normalizing the Fourier transformed HD-ESFG spectrum of the C1-PDI film by the spectrum resulting from a similar set of measurements performed on a GaAs(110) wafer. In so doing, we not only correct for the spectral contribution from the LO but also the spectral dependence of the WL field. Figure 7-8B compares the values of $|\vec{E}_{Samp}|^2$ determined by applying this normalization procedure to the HD-ESFG data to that measured by direct ESFG without the use of a LO. Similar to the HD-ESFG spectrum, the spectrum of the WL field has been deconvoluted from the direct ESFG signal by normalization with a similar measurement performed on GaAs.

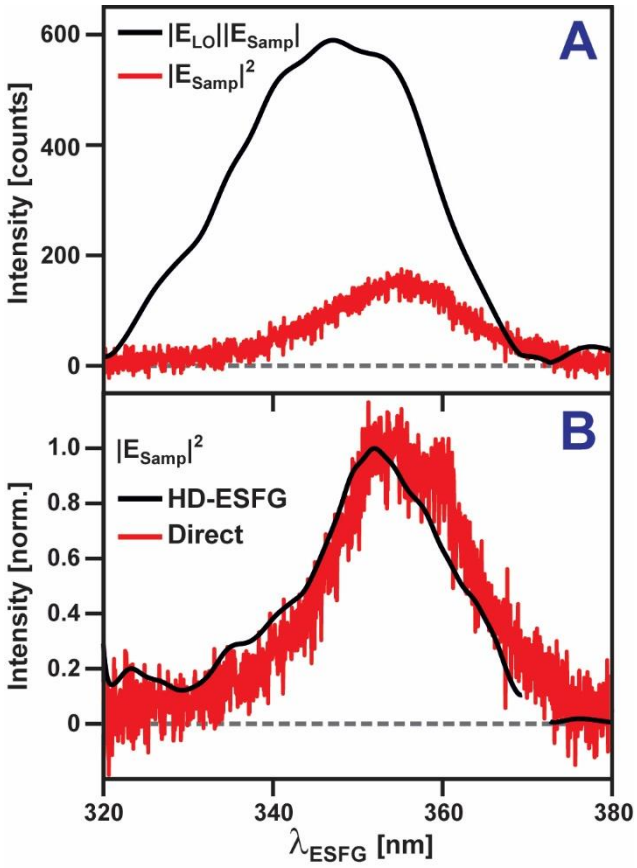


**Figure 7-8:** (A) Comparison of extracted cross term from HD-ESFG of a 52 nm C1-PDI film to directly detected ESFG spectrum or the same film (red). (B) Spectra of $|\vec{E}_{Samp}|^2$ extracted from HD-ESFG (black) and direct ESFG measurements (red) shown in panel (A).

Overall, there is quite good agreement between both sets of spectra, both in terms of the position and relative amplitude of peaks. Importantly, while both spectra display a prominent peak near 352 nm, some of the smaller bands that appear at 325, 335, and 340 nm in the HD-ESFG spectrum are obscured by detector noise in the direct ESFG spectrum. Here we see one of the advantages offered by HD-ESFG detection. In a direct ESFG measurement, two sources of noise can commonly obscure a signal: electronic noise associated with the readout of signals from a detector and shot noise due to fluctuations in the intensity of the laser source. For samples that generate strong ESFG fields, electronic

noise in a direct ESFG measurement can be small relative to the strength of the ESFG signal. For such signals, laser shot noise acts as the dominant noise source and optical heterodyne detection offers no significant signal-to-noise advantage over direct detection as the shot noise of the signal field is simply amplified by the LO.[14,36] However, for ESFG spectral components that are comparable to or weaker than the electronic noise level of the detector, heterodyne detection can boost the signal amplitude above the detector's noise floor. As such, weak bands that appear at short wavelengths in the direct ESFG spectrum in Figure 7-8B are much more pronounced in the HD-ESFG spectrum.

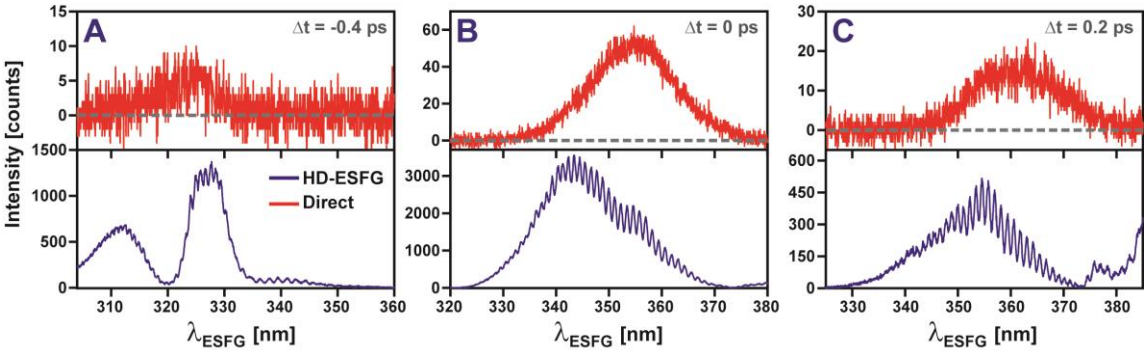


**Figure 7-9:** Comparison of direct (red) and HD-ESFG (blue) signals measured for a 52 nm C1-PDI film at different time delays between the white light and upconversion fields.

As proof of the increased sensitivity of HD-ESFG to weak signals, in Figure 7-9 we compare HD-ESFG and direct ESFG spectra measured for the 52 nm C1-PDI film for different time delays between the WL and upconversion fields**.** As the delay is scanned, the signal envelope shifts from short to long wavelengths, due to the chirp of the WL field. Panels A, B, and C in Figure 7-9 show direct and HD-ESFG signals measured at the peak of the temporal overlap between the WL and upconversion fields (panel B: $\Delta t = 0$ ps) and the edges of this overlap (panel A: $\Delta t = -0.4$ ps & panel C: $\Delta t = 0.2$ ps). While the directly detected ESFG signal measured at $\Delta t = 0$ ps is strong enough that its amplitude rises above

the background noise of the detector (Figure 7-9B, top), for time delays closer to the edge of temporal overlap between the WL and upconversion fields, the signal intensity is much lower. In particular, the direct signal measured at $\Delta t$ = -0.4 ps (Figure 7-9A, top) barely rises above the detector's noise floor at 6 counts for the 120 s acquisition time giving just 0.05 cts/s.

In contrast, the HD-ESFG signal measured at $\Delta t$ = -0.4 ps (Figure 7-9A, bottom) shows clear oscillations that extend from 310 to 350 nm, indicating the presence of an ESFG field emanated by the C1-PDI sample film whose existence is obscured by detector noise in a direct ESFG measurement. At the HD-ESFG spectrum's peak, the interference fringes display a max-to-min spacing of 225 counts corresponding to 1.87 cts/s for the 120 s acquisition time, or roughly 37.5× stronger than that of the direct ESFG measurement. For the CCD we employ, background counts primarily arise from the read noise associated with the CCD rather than dark current, and as such will largely be independent of data acquisition time. In principle, a comparable signal-to-noise ratio could be achieved in the direct ESFG measurement by lengthening the acquisition time, but given the difference in count rate, this would require lengthening the measurement time for a single time step from 2 minutes to 1.25 hours (37.5× longer). Examining the data in panels 7-9B and 7-9C, oscillations in the HD-ESFG signal can be observed to extend beyond the points where the direct ESFG signal returns to baseline. These results show that heterodyne detection can lift weak signal features that are not shot-noise limited above the limit of detection of an optical system, thereby allowing for more accurate determination of a sample's ESFG line shape.

While both the HD-ESFG and direct ESFG spectra in Figure 7-8B should overlap following the deconvolution steps above, there is a notable 2 nm shift between the peak of these spectra. One possible explanation for this shift is that it results from improved

sensitivity to low amplitude features in the HD-ESFG measurement that are obscured in direct ESFG measurements. Alternatively, this shift could result from imperfect deconvolution of the LO from the HD-ESFG spectrum. Temporal walk off within the quartz crystal used to generate the LO limits its bandwidth and causes its amplitude to drop substantially near 373 nm. While this signal drop can in principle be corrected by normalizing the HD-ESFG spectrum by the LO's spectral amplitude, as is done in Figure 7-8B, this deconvolution assumes perfect spectral overlap between the LO and signal fields, which likely breaks down when the LO displays a complicated temporal shape, as would be expected near 373 nm. Using a thinner piece of z-cut quartz to produce the LO can extend its spectral bandwidth and mitigate windowing effects imposed on HD-ESFG spectra.

In Figure 7-10 we compare the linear absorption spectrum of the C1-PDI film (blue dashed) with the amplitude of the ESFG field emitted by it, $|\vec{E}_{Samp}|$, as determined by HD-ESFG (red solid). To aid in comparing these two spectra, we have plotted the ESFG data both as a function of the wavelength of the emitted ESFG field, $\lambda_{ESFG}$, and the wavelength of the WL field that drives its emission, $\lambda_{WL}$. Examining the data, it is clear the film's ESFG spectrum distinctly differs from its linear absorption spectrum. While the film's lowest energy absorption band peaks at 568 nm, the ESFG spectrum is shifted to lower energy, peaking instead at $\lambda_{WL}$ = 627 nm with a broad tail that extends to nearly 700 nm. Additionally, the measured C1-PDI spectrum here differs from that of those measured in Chapter 6, being further red shifted and having a different structure. We attribute these to the higher energy of the upconversion beam at 804 nm pushing the ESFG spectra into a region where there are in fact multiple photon resonances that contribute to the ESFG signal, which we avoid with an upconversion wavelength of 885 nm in Chapter 6. We are working to fully separate these contributions.

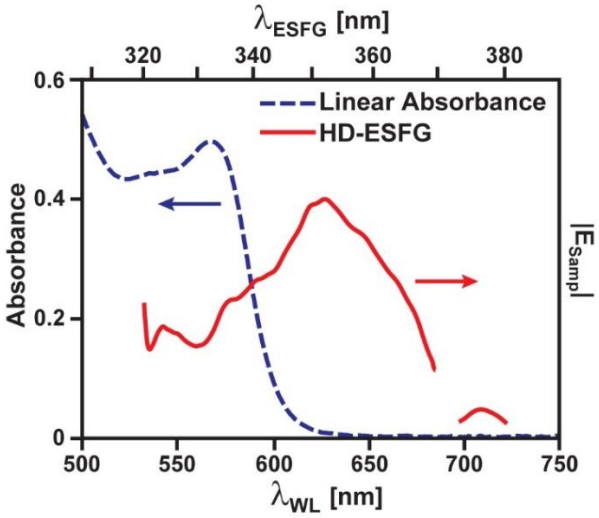


**Figure 7-10:** Comparison of the linear absorption spectrum of a C1-PDI film and its HD-ESFG field amplitude, $|\vec{E}_{Samp}|$ (red line).

One potential explanation for the prominent red-shift of the ESFG spectrum is that its emission from the C1-film is not driven by resonance between spectral components of the WL field and C1-PDI's valence electronic transitions, but rather by resonance between the frequencies produced by summing the WL and upconversion fields and higher lying C1-PDI electronic states. However, in this scenario the strength of the emitted ESFG field would be proportional to the product of C1-PDI's one-photon and two-photon absorption cross-sections at $\lambda_{ESFG}$.[37,38] As the film only shows minimal absorption in the UV spectral range (Figure 7-2), this scenario seems unlikely. A second hypothesis for the observed red-shift of the ESFG spectrum is that molecules in the vicinity of the $SiO_2$ interface experience some degree of solvatochromic stabilization.[39] However, the static dielectric constant of $SiO_2$ is only marginally larger than that of bulk C1-PDI, which suggests this hypothesis may not fully explain the magnitude of the red-shift we observe. A third explanation that seems most likely is that the presence of the $SiO_2$ layer imparts strain to C1-PDI crystallites at the junction between these materials as discussed previously.

Differentiating between these scenarios and others requires that the HD-ESFG spectrum measured for C1-PDI accurately reports on the electronic DoS of the buried C1-PDI:$SiO_2$ interface. In Chapter 5 and 6 we have shown that sum-frequency spectra of OSC thin films contain contributions from both their air-exposed and buried interfaces. Therefore, extracting information from an ESFG spectrum necessitates first fitting the data using a thin-film interference model that can separate signal contributions that originate from each interface of an OSC film.[1,2] As we show below, HD-ESFG spectra allow for a more accurate retrieval of the $\chi^{(2)}$ of a buried OSC surface than direct ESFG measurements as HD-ESFG measurements provide the spectral phase of the ESFG signal field. This information delivers an additional constraint that can differentiate between distinct trial $\chi^{(2)}$ lineshapes that produce similar fits to direct ESFG spectra.

### 7.5: Improved Interference Modeling Using Heterodyne-Detected ESFG

To test how the inclusion of the spectral phase of ESFG signals influences our ability to extract the $\chi^{(2)}$ of a buried OSC interface, we performed a set of model calculations where we considered a thin film of a PDI molecule related to C1-PDI, N−N′-dioctyl-3,4,9,10-perylenedicarboximide (C8-PDI), that had been deposited on an amorphous $SiO_2$ substrate. Each interface of the C8-PDI layer was assumed to be ESFG active, with a $\chi^{(2)}$ containing a pair of Lorentzian oscillators (see Chapter 3). Using this information and known optical constants of both $SiO_2$[40] and C8-PDI,[5] we employed an approach developed by O'Brien and Massari[2] and discussed in Chapter 3 to calculate how the ESFG field reflected by the film varies with the thickness of the C8-PDI layer. This calculation assumes an angle of incidence of 45º for each beam and a polarization combination of SPS for the ESFG, WL, and upconversion fields respectively. For this polarization condition, only the $\chi^{(2)}_{yzy}$ component of the total $\chi^{(2)}$ tensor contributes to the

ESFG response.[41,42] We then add Gaussian-distributed noise to this signal to make it more representative of experimental data. The result of this calculation is shown in the top panel of Figure 7-11, which plots the square modulus of the ESFG field, $|\vec{E}_{Samp}|^2$, as a function of film thickness. This corresponds to the signal detected in a direct ESFG experiment. As the thickness of the sample film increases, the ESFG signal is observed to oscillate in amplitude due to interference between signals emitted from the air-exposed and buried C8-PDI interfaces.

To assess the importance of spectral phase for retrieving $\boldsymbol{\chi}^{(2)}$, we use this data as the target input for a series of calculations whose goal is to reproduce this data set starting from a randomly generated $\chi^{(2)}_{yzy}$ for each C8-PDI film interface. In one set of these calculations, which we label as "Direct Fit," only the intensity of the target ESFG signal, $|\vec{E}_{Samp}|^2$, is considered when fitting. In another, which we label as "HD-ESFG Fit," both the amplitude and phase of the target ESFG field are accounted for when fitting. The middle and bottom panels of Figure 7-11 display representative fits to the target data set using both methodologies, employing the same initial guess for the $\chi^{(2)}_{yzy}$ response of each C8-PDI film interface. Following optimization, both methodologies converge to fits that well reproduce the intensity of the ESFG field as a function of film thickness. We generally find this result to be independent of the starting guess used for the $\chi^{(2)}_{yzy}$ response of each interface.

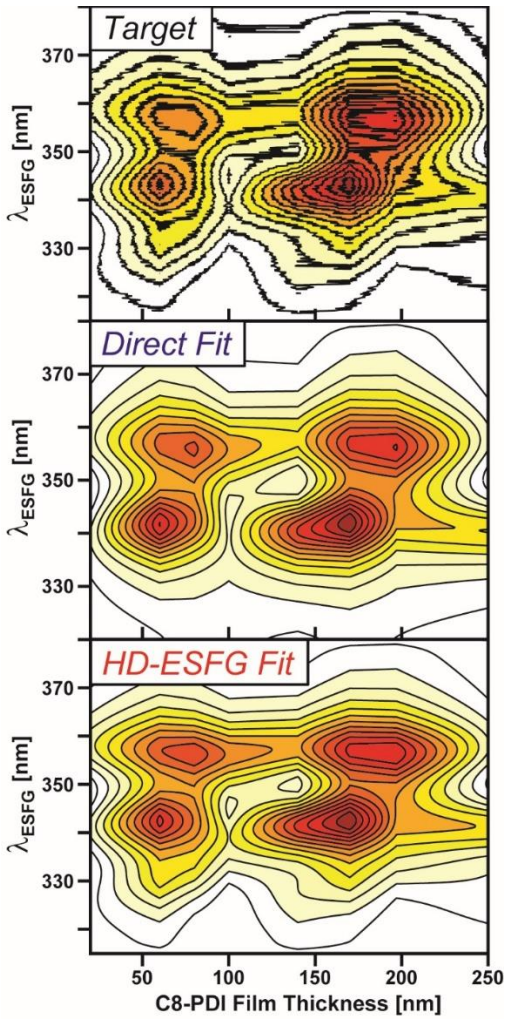


**Figure 7-11:** (Top) Target data set determining $\chi^{(2)}_{yzy}$. Fits to this data set without spectral phase of the signal field (Middle) and with (Bottom).

However, we find the optimized $\chi^{(2)}_{yzy}$ response used for the buried interface strongly differs between the Direct and HD-ESFG fits. Figure 7-12 compares the imaginary components of the optimized $\chi^{(2)}_{yzy}$ response found by each fitting routine. While both fits accurately reproduce the target $\chi^{(2)}_{yzy}$ of the air-exposed C8-PDI interface, the optimized response determined by direct fitting is unable to reproduce the $\chi^{(2)}_{yzy}$ of the buried surface, predicting that this lineshape is composed of only a single Lorentzian resonance rather than

a pair of peaks. In contrast, the HD-ESFG fit accurately reproduces the spectral position and amplitude of both peaks in the $\chi^{(2)}_{yzy}$ response of the buried C8-PDI interface, suggesting the inclusion of spectral phase in our interference model improves the accuracy of the line shapes for the $\boldsymbol{\chi}^{(2)}$ tensor components recovered from it. While the calculation we highlight in Figure 7-12 is somewhat of an extreme case in that it yields completely different line shapes for the $\chi^{(2)}_{yzy}$ of the buried C8-PDI:$SiO_2$ interface, the improvement in the accuracy of recovering the buried $\chi^{(2)}_{yzy}$ lineshape upon the inclusion of spectral phase holds across a range of different initial guesses for the $\chi^{(2)}_{yzy}$ of each interface and is somewhat insensitive to the algorithm used to optimize the fit.

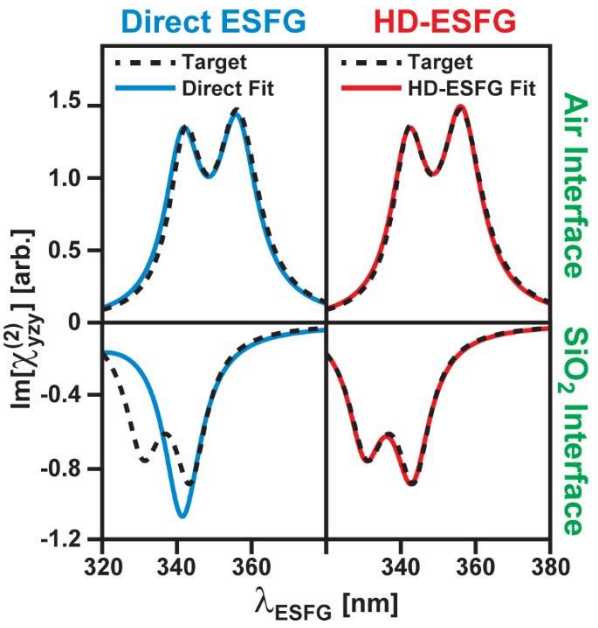


**Figure 7-12:** $\chi^{(2)}_{yzy}$ of the air-exposed and C8-PDI:$SiO_2$ interface used to generate the target data in Figure 7-12 and the reconstructions of this response with two fitting methods.

We conclude that with the phase information we gain from HD-ESFG measurements, we can better determine the electronic DoS of C1-PDI molecules at buried

interfaces. Our model calculations indicate that without accounting for the phase of the ESFG signal during interference modeling, we are in danger of retrieving an incorrect line shape for the $\chi^{(2)}$ of the buried C1-PDI interface from these measurements. This can skew the interpretation of ESFG signals measured from these and other OSC films.

### 7.6: Conclusions

In this Chapter, we have demonstrated a simple method for incorporating heterodyne detection into a broadband ESFG spectrometer and described some of the benefits that HD-ESFG detection holds over the direct detection of ESFG signals, particularly for OSC thin films. HD-ESFG's sensitivity to low amplitude signals can highlight weak features that appear in a spectrum. For samples such as OSC thin films that contain multiple ESFG-active layers, the phase information provided by HD-ESFG measurements can constrain optical models that seek to separate the various interfacial electronic DoS within a sample. Without accounting for this phase, such interference models can be more prone to reporting spectra that do not accurately reflect the DoS of a buried interface. In addition, as the phase of an ESFG signal depends strongly on the thickness of a sample film, we believe HD-ESFG measurements will be of great utility in the study of buried interfaces where the gain of sign for the extracted $\chi^{(2)}$ will help for orientational interpretation. The advantages mentioned above will be critical to both the implementation and interpretation of time-resolved ESFG studies as they provide enhanced sensitivity to the electronic structure of buried interfaces while simultaneously reducing data collection times needed to record ESFG spectra.

## 7.7: Chapter References


(1) Pandey, R.; Moon, A. P.; Bender, J. A.; Roberts, S. T. Extracting the Density of States of Copper Phthalocyanine at the SiO2 Interface with Electronic Sum Frequency Generation. *J. Phys. Chem. Lett.* **2016**, *7* (6), 1060–1066.

(2) O'Brien, D. B.; Massari, A. M. Modeling Multilayer Thin Film Interference Effects in Interface-Specific Coherent Nonlinear Optical Spectroscopies. *J. Opt. Soc. Am. B* **2013**, *30* (6), 1503–1503.

(3) O'Brien, D. B.; Massari, A. M. Experimental Evidence for an Optical Interference Model for Vibrational Sum Frequency Generation on Multilayer Organic Thin Film Systems I: Electric Dipole Approximation. *J. Chem. Phys.* **2015**, *142*, 024703–024703.

(4) O'Brien, D. B.; Massari, A. M. Experimental Evidence for an Optical Interference Model for Vibrational Sum Frequency Generation on Multilayer Organic Thin Film Systems II: Consideration for Higher Order Terms. *J. Chem. Phys.* **2015**, *142*, 024704–024704.

(5) O'Brien, D. B.; Massari, A. M. Simulated Vibrational Sum Frequency Generation from a Multilayer Thin Film System with Two Active Interfaces. *J. Chem. Phys.* **2013**, *138* (15), 154708–154708.

(6) Kemnitz, K.; Bhattacharyya, K.; Hicks, J. M.; Pinto, G. R.; Eisenthal, K. B.; Heinz, T. F. The Phase of Second-Harmonic Light Generated at an Interface and Its Relation to Absolute Molecular Orientation. *Chem. Phys. Lett.* **1985**, *131* (4,5), 285–290.

(7) Yamaguchi, S.; Tahara, T. Heterodyne-Detected Electronic Sum Frequency Generation: "Up" versus "down" Alignment of Interfacial Molecules. *J. Chem. Phys.* **2008**, *129*, 101102–101102.

(8) Nelson, C. A.; Luo, J.; Laghumavarapu, R. B.; Huffaker, D. L.; Zhu, X.-Y. Time-, Energy-, and Phase-Resolved Second-Harmonic Generation at Semiconductor Interfaces. *J. Phys. Chem. C* **2014**, *118* (48), 27981–27988.

(9) Park, H.; Gutierrez, M.; Wu, X.; Kim, W.; Zhu, X. Y. Optical Probe of Charge Separation at Organic/Inorganic Semiconductor Interfaces. *J. Phys. Chem. C* **2013**, *117*, 10974–10979.

(10) Inoue, K.; Nihonyanagi, S.; Singh, P. C.; Yamaguchi, S.; Tahara, T. 2D Heterodyne-Detected Sum Frequency Generation Study on the Ultrafast Vibrational Dynamics of H2O and HOD Water at Charged Interfaces. *J. Chem. Phys.* **2015**, *142* (21), 212431–212431.

(11) Vanselous, H.; Petersen, P. B. Extending the Capabilities of Heterdoyne-Detected Sum-Frequency Generatino Spectroscopy: Probing Any Interface in Any Polarization Combination. *J. Phys. Chem. C* **2016**, *120* (15), 8175–8184.

(12) Wilson, P. T.; Jiang, Y.; Aktsipetrov, O. A.; Mishina, E. D.; Downer, M. C. Frequency-Domain Interferometric Second-Harmonic Spectroscopy. *Opt. Lett. 24* (7), 496–498.

(13) Stiopkin, I. V.; Jayathilake, H. D.; Bordenyuk, A. N.; Benderskii, A. V. Heterodyne-Detected Vibrational Sum Frequency Generation Spectroscopy. *J. Am. Chem. Soc.* **2008**, *130*, 2271–2275.

(14) Pool, R. E.; Versluis, J.; Backus, E. H. G.; Bonn, M. Comparative Study of Direct and Phase-Specific Vibrational Sum-Frequency Generation Spectroscopy: Advantages and Limitations. *J. Phys. Chem. B* **2011**, *115* (51), 15362–15369.

(15) Ostroverkhov, V.; Waychunas, G. A.; Shen, Y. R. New Information on Water Interfacial Structure Revelaed by Phase-Sensitive Surface Spectroscopy. *Phys. Rev. Lett.* **2005**, *94* (9), 046102:1-4.

(16) Chang, R. K.; Ducuing, J.; Bloembergen, N. Relative Phase Measurement between Fundamental and Second-Harmonic Spectroscopy. *Phys Rev Lett* **1965**, *15*, 6.

(17) Wilcox, D. E.; Sykes, M. E.; Niedringhaus, A.; Shtein, M.; Ogilvie, J. P. Heterodyne-Detected and Ultrafast Time-Resolved Second-Harmonic Generation for Sensitive Measurements of Charge Transfer. *Opt. Lett.* **2014**, *39* (14), 4274–4274.

(18) Li Fu, S.-L. C.; Wang, H.-F. Validation of Spectra and Phase in Sub-1 Cm-1 Resolution Sum-Frequency Generatino Vibrational Spectroscopy through Internal Heterodyne PHase-Resolved Measurement. *J. Phys. Chem. B* **2016**, *120* (8), 1579–1589.

(19) Veenstra, K. J.; Petukhov, A. V.; De Boer, A. P.; Rasing, T. Phase-Sensitive Detection Technique for Surface Nonlinear Optics. *Phys Rev B* **1998**, *58*, R16020.

(20) Eaton, S. W.; Shoer, L. E.; Karlen, S. D.; Dyar, S. M.; Margulies, E. a; Veldkamp, B. S.; Ramanan, C.; Hartzler, D. a; Savikhin, S.; Marks, T. J.; et al. Singlet Exciton Fission in Polycrystalline Thin Films of a Slip-Stacked Perylenediimide. *J. Am. Chem. Soc.* **2013**, *135* (39), 14701–14712.

(21) Le, A. K.; Bender, J. A.; Roberts, S. T. Slow Singlet Fission Observed in a Polycrystaline Perylenediimide Thin Film. *J Phys Chem Lett* **2016**, *7*, 4922–4928.

(22) Renaud, N.; Sherratt, P. A.; Ratner, M. A. Mapping the Relation between Stacking Geometries and Singlet Fission Yield in a Class of Organic Crystals. *J. Phys. Chem. Lett.* **2013**, *4* (7), 1065–1069.

(23) Renaud, N.; Ferdinand C. Grozema. Intermolecular Vibration Modes Speed Up Singlet Fission in Perylenediimide Crystals. *J. Phys. Chem. Lett.* **2015**.

(24) Hadicke, E.; Graser, F. Structures of Eleven Perylene-3,4:9,10-Bis(Dicarboximide) Pigments. *Acta Crystallogr.* **1986**, *C42*, 189–195.

(25) Foglia, L.; Wolf, M.; Stahler, J. Ultrafast Dynamics in Solids Probed by Femtosecond Time-Resolved Broadband Elkectronic Sum Frequency Generation. *Appl. Phys. Lett.* **2016**, *109*, 202106.

(26) Wilcox, D. E.; Lee, M. H.; Sykes, M. E.; Niedringhaus, A.; Geva, E.; Dunietz, B. D.; Shtein, M.; Ogilvie, J. P. Ultrafast Charge-Transfer Dynamics at the Boron Subphthalocyanine Chloride/C60 Heterojunction: Comparison between Experiment and Theory. *J. Phys. Chem. Lett.* **2015**, *6* (3), 569–575.

(27) Xiong, W.; Laaser, J. E.; Mehlenbacher, R. D.; Zanni, M. T. Adding a Dimension to the Infrared Spectra of Interfaces Using Heterodyne Detected 2D Sum-Frequency Generation ( HD 2D SFG ) Spectroscopy. *Proc. Natl. Acad. Sci.* **2011**, *108* (52), 20902–20907.

(28) Zhang, Z.; Piatkowski, L.; Bakker, H. J.; Bonn, M. Ultrafast Vibratinal Energy Transfer at the Water / Air Interface Revealed by Two-Dimensional. *Nat. Chem.* **2011**, *3* (11), 888–893.

(29) Inoue, K.; Ishiyama, T.; Nihonyanagi, S.; Yamaguchi, S.; Morita, A.; Tahara, T. Efficient Spectral Diffusion at the Air/Water Interface Revealed by Femtosecond Time-Resolved Heterodyne-Detected Vibrational Sum Frequency Generation Spectroscopy. *J Phys Chem Lett* **2016**, *7*, 1811.

(30) Mondal, S. K.; Yamaguchi, S.; Tahara, T. Molecules at the Air/Water Interface Experience a More Inhomogeneous Solvation Environment than in Bulk Solvents: A Quantitative Band Shape Analysis of Interfacial Electronic Spectra Obtained by HD-ESFG. *J. Phys. Chem. C* **2011**, *115* (7), 3083–3089.

(31) Kundu, A.; Yamaguchi, S.; Tahara, T. Evaluation of PH at Charged Lipid/Water Interfaces by Heterodyne-Detected Electronic Sum Frequency Generation. *J Phys Chem Lett* **2014**, *5*, 762.

(32) Yamaguchi, S.; Bhattacharyya, K.; Tahara, T. Acid-Base Equilibrium at an Aqueous Interface: PH Spectrometry by Heterodyne-Detected Electronic Sum Frequency Generation. *J Phys Chem C* **2011**, *115*, 4168.

(33) Boyd, R. W. *Nonlinear Optics*; Academic Press: Boston, 1992.

(34) Brixner, T.; Mancal, T.; Stiopkin, I. V.; Fleming, G. R. Phase-Stabilized Two-Dimensional Electronic Spectroscopy. *J Chem Phys* **2004**, *121*, 4221–4236.

(35) Rivera, C. A.; Bradforth, S. E.; Tempea, G. Gires-Tournois Interferometer Type Negative Dispersion MIrrors for Deep Ultraviolet Pulse Compression. *Opt Express* **2010**, *18*, 18615.

(36) Dadap, J. I.; Shan, J.; Weling, A. S.; Heinz, T. F. Homodyne Detection of Second-Harmonic Generation as a Probe of Electric Fields. *Appl Phys B* **1999**, *68*, 333.

(37) Moad, A. J.; Simpson, G. J. A Unified Treatment of Selection Rules and Symmetry Relations for Sum-Frequency and Second Harmonic Spectroscopies. *J. Phys. Chem. B* **2004**, *108* (11), 3548–3562.

(38) Lin, C. K.; Hayashi, M.; Lin, S. H. Theoretical Formulation and Simulation of Electronic Sum-Frequency Generation Spectroscopy. *J. Phys. Chem. C* **2013**, *117* (45), 23797–23805.

(39) Yost, S. R.; Voorhis, T. V. Electrostatic Effects at Organic Semiconductor Interfaces: A Mechanism for "Cold" Exciton Breakup. *J. Phys. Chem. C* **2013**, *117* (11), 5617–5625.

(40) Schott AG. Optical Glass Data Sheets. 2015.

(41) Zhuang, X.; Miranda, P.; Kim, D.; Shen, Y. Mapping Molecular Orientation and Conformation at Interfaces by Surface Nonlinear Optics. *Phys. Rev. B* **1999**, *59* (19), 12632–12640.

(42) Wang, H.-F.; Gan, W.; Lu, R.; Rao, Y.; Wu, B.-H. Quantitative Spectral and Orientational Analysis in Surface Sum Frequency Generation Vibrational Spectroscopy (SFG-VS). *Int Rev Phys Chem* **2005**, *24*, 191.

# References


(1) Gabriel, M. M.; Kirschbrown, J. R.; Christesen, J. D.; Pinion, C. W.; Zigler, D. F.; Grumstrup, E. M.; Mehl, B. P.; Cating, E. E. M.; Cahoon, J. F.; Papanikolas, J. M. Direct Imaging of Free Carrier and Trap Carrier Motion in Silicon Nanowires by Spatially-Separated Femtosecond Pump–Probe Microscopy. *Nano Letters* **2013**, *13* (3), 1336–1340.

(2) Abbas, M. A.; Basit, M. A.; Yoon, S. J.; Lee, G. J.; Lee, M. D.; Park, T. J.; Kamat, P. V.; Bang, J. H. Revival of Solar Paint Concept: Air-Processable Solar Paints for the Fabrication of Quantum Dot-Sensitized Solar Cells. *The Journal of Physical Chemistry C* **2017**, *121* (33), 17658–17670.

(3) Alharbi, F. H.; Kais, S. Theoretical Limits of Photovoltaics Efficiency and Possible Improvements by Intuitive Approaches Learned from Photosynthesis and Quantum Coherence. *Renewable and Sustainable Energy Reviews* **2015**, *43*, 1073–1089.

(4) Briseno, A. L.; Mannsfeld, S. C. B.; Reese, C.; Hancock, J. M.; Xiong, Y.; Jenekhe, S. A.; Bao, Z.; Xia, Y. Perylenediimide Nanowires and Their Use in Fabricating Field-Effect Transistors and Complementary Inverters. *Nano Letters* **2007**, *7* (9), 2847–2853.

(5) Chistyakov, A. A.; Zvaigzne, M. A.; Nikitenko, V. R.; Tameev, A. R.; Martynov, I. L.; Prezhdo, O. V. Optoelectronic Properties of Semiconductor Quantum Dot Solids for Photovoltaic Applications. *The Journal of Physical Chemistry Letters* **2017**, *8* (17), 4129–4139.

(6) Song, L.; Guo, X.; Hu, Y.; Lv, Y.; Lin, J.; Liu, Z.; Fan, Y.; Liu, X. Efficient Inorganic Perovskite Light-Emitting Diodes with Polyethylene Glycol Passivated Ultrathin $CsPbBr_3$ Films. *The Journal of Physical Chemistry Letters* **2017**, *8* (17), 4148–4154.

(7) Schlesinger, R.; Bianchi, F.; Blumstengel, S.; Christodoulou, C.; Ovsyannikov, R.; Kobin, B.; Moudgil, K.; Barlow, S.; Hecht, S.; Marder, S. R.; et al. Efficient Light Emission from Inorganic and Organic Semiconductor Hybrid Structures by Energy-Level Tuning. *Nature Communications* **2015**, *6*, 6754.

(8) Sirringhaus, H. 25th Anniversary Article: Organic Field-Effect Transistors: The Path Beyond Amorphous Silicon. *Advanced Materials* **2014**, *26* (9), 1319–1335.

(9) Hedley, G. J.; Ruseckas, A.; Samuel, I. D. W. Light Harvesting for Organic Photovoltaics. *Chemical Reviews* **2017**, *117* (2), 796–837.

(10) Guo, F.; Karl, A.; Xue, Q.-F.; Tam, K. C.; Forberich, K.; Brabec, C. J. The Fabrication of Color-Tunable Organic Light-Emitting Diode Displays via Solution Processing. *Light: Science & Applications* **2017**, *6* (11), e17094.

(11) Futscher, M. H.; Rao, A.; Ehrler, B. The Potential of Singlet Fission Photon Multipliers as an Alternative to Silicon-Based Tandem Solar Cells. *ACS Energy Letters* **2018**, *3* (10), 2587–2592.

(12) Tabernig, S. W.; Daiber, B.; Wang, T.; Ehrler, B. Enhancing Silicon Solar Cells with Singlet Fission: The Case for Förster Resonant Energy Transfer Using a Quantum Dot Intermediate. *Journal of Photonics for Energy* **2018**, *8* (02), 1.

(13) Schwerin, A. F.; Johnson, J. C.; Smith, M. B.; Sreearunothai, P.; Popović, D.; Černý, J.; Havlas, Z.; Paci, I.; Akdag, A.; MacLeod, M. K.; et al. Toward Designed Singlet Fission: Electronic States and Photophysics of 1,3-Diphenylisobenzofuran †. *The Journal of Physical Chemistry A* **2010**, *114* (3), 1457–1473.

(14) Agranovich, V. M.; Gartstein, Y. N.; Litinskaya, M. Hybrid Resonant Organic–Inorganic Nanostructures for Optoelectronic Applications. *Chemical Reviews* **2011**, *111* (9), 5179–5214.

(15) Kymakis, E. Interfacial Engineering of Perovskite Solar Cells for Improved Performance and Stability. *Advanced Materials Interfaces* **2018**, *5* (22), 1801595.

(16) Rajagopal, A.; Yao, K.; Jen, A. K.-Y. Toward Perovskite Solar Cell Commercialization: A Perspective and Research Roadmap Based on Interfacial Engineering. *Advanced Materials* **2018**, *30* (32), 1800455.

(17) Wang, Y.; Duan, J.; Duan, Y.; Zhao, Y.; Pang, Z.; He, B.; Tang, Q. Interfacial Engineering of Hybridized Solar Cells for Simultaneously Harvesting Solar and Rain Energies. *Journal of Materials Chemistry A* **2017**, *5* (35), 18551–18560.

(18) Ju, H.; Knesting, K. M.; Zhang, W.; Pan, X.; Wang, C.-H.; Yang, Y.-W.; Ginger, D. S.; Zhu, J. Interplay between Interfacial Structures and Device Performance in Organic Solar Cells: A Case Study with the Low Work Function Metal, Calcium. *ACS Applied Materials & Interfaces* **2016**, *8* (3), 2125–2131.

(19) Samadi Khoshkhoo, M.; Peisert, H.; Chassé, T.; Scheele, M. The Role of the Density of Interface States in Interfacial Energy Level Alignment of PTCDA. *Organic Electronics* **2017**, *49*, 249–254.

(20) Zimmerman, J. D.; Xiao, X.; Renshaw, C. K.; Wang, S.; Diev, V. V.; Thompson, M. E.; Forrest, S. R. Independent Control of Bulk and Interfacial Morphologies of Small Molecular Weight Organic Heterojunction Solar Cells. *Nano Letters* **2012**, *12* (8), 4366–4371.

(21) MacQueen, R.; Liebhaber, M.; Niederhausen, J.; Mews, M.; Gersmann, C.; Jäckle, S.; Jäger, K.; Tayebjee, M. J. Y.; Schmidt, T. W.; Rech, B.; et al. Crystalline Silicon Solar Cells with Tetracene Interlayers: The Path to Silicon-Singlet Fission Heterojunction Devices. *Mater. Horiz.* **2018**.

(22) Burdett, J. J.; Bardeen, C. J. The Dynamics of Singlet Fission in Crystalline Tetracene and Covalent Analogs. *Accounts of Chemical Research* **2013**, *46* (6), 1312–1320.

(23) Brawand, N. P.; Goldey, M. B.; Vörös, M.; Galli, G. Defect States and Charge Transport in Quantum Dot Solids. *Chemistry of Materials* **2017**, *29* (3), 1255–1262.

(24) Amsalem, P.; Heimel, G.; Oehzelt, M.; Koch, N. The Interface Electronic Properties of Organic Photovoltaic Cells. *Journal of Electron Spectroscopy and Related Phenomena* **2015**, *204*, 177–185.

(25) Akaike, K.; Kumai, T.; Nakano, K.; Abdullah, S.; Ouchi, S.; Uemura, Y.; Ito, Y.; Onishi, A.; Yoshida, H.; Tajima, K.; et al. Effects of Molecular Orientation of Fullerene Derivative at Donor/Acceptor Interface on Device Performance of Organic Photovoltaics. *Chemistry of Materials* **2018**.

(26) Gregg, B. A.; Hanna, M. C. Comparing Organic to Inorganic Photovoltaic Cells: Theory, Experiment, and Simulation. *Journal of Applied Physics* **2003**, *93* (6), 3605–3614.

(27) Goldey, M. B.; Reid, D.; de Pablo, J.; Galli, G. Planarity and Multiple Components Promote Organic Photovoltaic Efficiency by Improving Electronic Transport. *Physical Chemistry Chemical Physics* **2016**, *18* (46), 31388–31399.

(28) Coropceanu, V.; Cornil, J.; da Silva Filho, D. A.; Olivier, Y.; Silbey, R.; Brédas, J.-L. Charge Transport in Organic Semiconductors. *Chemical Reviews* **2007**, *107* (4), 926–952.

(29) Delgado, M. C. R.; Kim, E.-G.; Filho, D. A. da S.; Bredas, J.-L. Tuning the Charge-Transport Parameters of Perylene Diimide Single Crystals via End and/or Core Functionalization: A Density Functional Theory Investigation. *Journal of the American Chemical Society* **2010**, *132* (10), 3375–3387.

(30) Hestand, N. J.; Tempelaar, R.; Knoester, J.; Jansen, T. L. C.; Spano, F. C. Exciton Mobility Control through Sub − Å Packing Modifications in Molecular Crystals. *Physical Review B* **2015**, *91* (19).

(31) Hestand, N. J.; Spano, F. C. Expanded Theory of H- and J-Molecular Aggregates: The Effects of Vibronic Coupling and Intermolecular Charge Transfer. *Chemical Reviews* **2018**.

(32) Hestand, N. J.; Spano, F. C. Molecular Aggregate Photophysics beyond the Kasha Model: Novel Design Principles for Organic Materials. *Accounts of Chemical Research* **2017**, *50* (2), 341–350.

(33) Spano, F. C. The Spectral Signatures of Frenkel Polarons in H- and J-Aggregates. *Accounts of Chemical Research* **2010**, *43* (3), 429–439.

(34) Beljonne, D.; Yamagata, H.; Brédas, J. L.; Spano, F. C.; Olivier, Y. Charge-Transfer Excitations Steer the Davydov Splitting and Mediate Singlet Exciton Fission in Pentacene. *Physical Review Letters* **2013**, *110* (22).

(35) Austin, A.; Hestand, N. J.; McKendry, I. G.; Zhong, C.; Zhu, X.; Zdilla, M. J.; Spano, F. C.; Szarko, J. M. Enhanced Davydov Splitting in Crystals of a Perylene Diimide Derivative. *The Journal of Physical Chemistry Letters* **2017**, *8* (6), 1118–1123.

(36) Li, Y.; Wang, J.; Xiong, W. Probing Electronic Structures of Organic Semiconductors at Buried Interfaces by Electronic Sum Frequency Generation Spectroscopy. *The Journal of Physical Chemistry C* **2015**, *119* (50), 28083–28089.

(37) Muntwiler, M.; Yang, Q.; Zhu, X.-Y. Exciton Dynamics at Interfaces of Organic Semiconductors. *Journal of Electron Spectroscopy and Related Phenomena* **2009**, *174* (1–3), 116–124.

(38) Chen, Y.; Tamblyn, I.; Quek, S. Y. Energy Level Alignment at Hybridized Organic?Metal Interfaces: The Role of Many-Electron Effects. *The Journal of Physical Chemistry C* **2017**.

(39) Galbraith, M. C. E.; Marks, M.; Tonner, R.; Höfer, U. Formation of an Organic/Metal Interface State from a Shockley Resonance. *The Journal of Physical Chemistry Letters* **2014**, *5* (1), 50–55.

(40) Moon, A. P.; Pandey, R.; Bender, J. A.; Cotton, D. E.; Renard, B. A.; Roberts, S. T. Using Heterodyne-Detected Electronic Sum Frequency Generation To Probe the Electronic Structure of Buried Interfaces. *The Journal of Physical Chemistry C* **2017**, *121* (34), 18653–18664.

(41) Pandey, R.; Moon, A. P.; Bender, J. A.; Roberts, S. T. Extracting the Density of States of Copper Phthalocyanine at the $SiO_2$ Interface with Electronic Sum Frequency Generation. *The Journal of Physical Chemistry Letters* **2016**, *7* (6), 1060–1066.

(42) Humbert, C.; Dreesen, L.; Nihonyanagi, S.; Masuda, T.; Kondo, T.; Mani, A. A.; Uosaki, K.; Thiry, P. A.; Peremans, A. Probing a Molecular Electronic Transition by Two-Colour Sum-Frequency Generation Spectroscopy. *Applied Surface Science* **2003**, *212–213*, 797–803.

(43) Yamaguchi, S.; Tahara, T. Determining Electronic Spectra at Interfaces by Electronic Sum Frequency Generation: One- and Two-Photon Double Resonant Oxazine 750 at the Air/Water Interface. *The Journal of Chemical Physics* **2006**, *125* (19), 194711.

(44) Shen, Y. R. Basic Theory of Surface Sum-Frequency Generation. *The Journal of Physical Chemistry C* **2012**, *116* (29), 15505–15509.

(45) Yamaguchi, S.; Tahara, T. Development of Electronic Sum Frequency Generation Spectroscopies and Their Application to Liquid Interfaces. *The Journal of Physical Chemistry C* **2015**, *119* (27), 14815–14828.

(46) Aprile, A.; Ciuchi, F.; Pinalli, R.; Dalcanale, E.; Pagliusi, P. Probing Molecular Recognition at the Solid–Gas Interface by Sum-Frequency Vibrational Spectroscopy. *The Journal of Physical Chemistry Letters* **2016**, *7* (15), 3022–3026.

(47) Eisenthal, K. B. Liquid Interfaces Probed by Second-Harmonic and Sum-Frequency Spectroscopy. *Chemical Reviews* **1996**, *96* (4), 1343–1360.

(48) Matsuzaki, K.; Nihonyanagi, S.; Yamaguchi, S.; Nagata, T.; Tahara, T. Vibrational Sum Frequency Generation by the Quadrupolar Mechanism at the Nonpolar Benzene/Air Interface. *The Journal of Physical Chemistry Letters* **2013**, *4* (10), 1654–1658.

(49) Myalitsin, A.; Urashima, S.; Nihonyanagi, S.; Yamaguchi, S.; Tahara, T. Water Structure at the Buried Silica/Aqueous Interface Studied by Heterodyne-Detected Vibrational Sum-Frequency Generation. *The Journal of Physical Chemistry C* **2016**, *120* (17), 9357–9363.

(50) Yamaguchi, S.; Watanabe, H.; Mondal, S. K.; Kundu, A.; Tahara, T. "Up" versus "down" Alignment and Hydration Structures of Solutes at the Air/water Interface Revealed by Heterodyne-Detected Electronic Sum Frequency Generation with Classical Molecular Dynamics Simulation. *The Journal of Chemical Physics* **2011**, *135* (19), 194705.

(51) Simpson, G. J.; Perry, J. M.; Ashmore-Good, C. L. Molecular and Surface Hyperpolarizability of Oriented Chromophores of Low Symmetry. *Physical Review B* **2002**, *66* (16).

(52) Davis, R. P.; Moad, A. J.; Goeken, G. S.; Wampler, R. D.; Simpson, G. J. Selection Rules and Symmetry Relations for Four-Wave Mixing Measurements of Uniaxial Assemblies. *The Journal of Physical Chemistry B* **2008**, *112* (18), 5834–5848.

(53) Deng, F.; Ulcickas, J. R. W.; Simpson, G. J. Theoretical Foundation for Electric-Dipole-Allowed Chiral-Specific Fluorescence Optical Rotary Dispersion (F-ORD) from Interfacial Assemblies. *The Journal of Physical Chemistry Letters* **2016**, *7* (21), 4248–4252.

(54) Dailey, C. A.; Burke, B. J.; Simpson, G. J. The General Failure of Kleinman Symmetry in Practical Nonlinear Optical Applications. *Chemical Physics Letters* **2004**, *390* (1–3), 8–13.

(55) Dow, X. Y.; DeWalt, E. L.; Newman, J. A.; Dettmar, C. M.; Simpson, G. J. Unified Theory for Polarization Analysis in Second Harmonic and Sum Frequency Microscopy. *Biophysical Journal* **2016**, *111* (7), 1553–1568.

(56) Moad, A. J.; Simpson, G. J. A Unified Treatment of Selection Rules and Symmetry Relations for Sum-Frequency and Second Harmonic Spectroscopies. *The Journal of Physical Chemistry B* **2004**, *108* (11), 3548–3562.

(57) Yamaguchi, S.; Shiratori, K.; Morita, A.; Tahara, T. Electric Quadrupole Contribution to the Nonresonant Background of Sum Frequency Generation at Air/liquid Interfaces. *The Journal of Chemical Physics* **2011**, *134* (18), 184705.

(58) O'Brien, D. B.; Massari, A. M. Experimental Evidence for an Optical Interference Model for Vibrational Sum Frequency Generation on Multilayer Organic Thin Film Systems I. Electric Dipole Approximation. *The Journal of Chemical Physics* **2015**, *142* (2), 024703.

(59) O'Brien, D. B.; Massari, A. M. Experimental Evidence for an Optical Interference Model for Vibrational Sum Frequency Generation on Multilayer Organic Thin Film System II. Consideration for Higher Order Terms. *The Journal of Chemical Physics* **2015**, *142* (2), 024704.

(60) O'Brien, D. B.; Massari, A. M. Modeling Multilayer Thin Film Interference Effects in Interface-Specific Coherent Nonlinear Optical Spectroscopies. *Journal of the Optical Society of America B* **2013**, *30* (6), 1503.

(61) Boyd, R. W. *Nonlinear Optics, Third Edition*, 3rd ed.; Academic Press, 2008.

(62) Shen, Y. R. *The Principles of Nonlinear Optics*; Wiley, 1984.

(63) Yamaguchi, S.; Tahara, T. Precise Electronic $\chi^{(2)}$ Spectra of Molecules Adsorbed at an Interface Measured by Multiplex Sum Frequency Generation. *J. Phys. Chem. B* **2004**, *108* (50), 19079–19082.

(64) Shen, Y. R. Optical Second Harmonic Generation at Interfaces. *Annu Rev Phys Chem* **1989**, *40*, 327–327.

(65) O'Brien, D. B.; Massari, A. M. Simulated Vibrational Sum Frequency Generation from a Multilayer Thin Film System with Two Active Interfaces. *J. Chem. Phys.* **2013**, *138* (15), 154708–154708.

(66) Knittl, Z. *Optics of Thin Films*; John Wiley & Sons: London, 1976.

(67) Inoue, K.; Ishiyama, T.; Nihonyanagi, S.; Yamaguchi, S.; Morita, A.; Tahara, T. Efficient Spectral Diffusion at the Air/Water Interface Revealed by Femtosecond Time-Resolved Heterodyne-Detected Vibrational Sum Frequency Generation Spectroscopy. *J Phys Chem Lett* **2016**, *7*, 1811.

(68) Wang, J.; Chen, X.; Clarke, M. L.; Chen, Z. Detection of Chiral Sum Frequency Generation Vibrational Spectra of Proteins and Peptides at Interfaces in Situ. *PNAS* **2005**, *102* (14), 4978–4983.

(69) Vanselous, H.; Petersen, P. B. Extending the Capabilities of Heterdoyne-Detected Sum-Frequency Generatino Spectroscopy: Probing Any Interface in Any Polarization Combination. *J. Phys. Chem. C* **2016**, *120* (15), 8175–8184.

(70) Li Fu, S.-L. C.; Wang, H.-F. Validation of Spectra and Phase in Sub-1 Cm-1 Resolution Sum-Frequency Generatino Vibrational Spectroscopy through Internal Heterodyne PHase-Resolved Measurement. *J. Phys. Chem. B* **2016**, *120* (8), 1579–1589.

(71) Mondal, S. K.; Yamaguchi, S.; Tahara, T. Molecules at the Air/Water Interface Experience a More Inhomogeneous Solvation Environment than in Bulk Solvents: A Quantitative Band Shape Analysis of Interfacial Electronic Spectra Obtained by HD-ESFG. *J. Phys. Chem. C* **2011**, *115* (7), 3083–3089.

(72) Yamaguchi, S.; Bhattacharyya, K.; Tahara, T. Acid-Base Equilibrium at an Aqueous Interface: PH Spectrometry by Heterodyne-Detected Electronic Sum Frequency Generation. *J Phys Chem C* **2011**, *115*, 4168.

(73) Yamaguchi, S.; Tahara, T. Heterodyne-Detected Electronic Sum Frequency Generation: "Up" versus "down" Alignment of Interfacial Molecules. *J. Chem. Phys.* **2008**, *129*, 101102–101102.

(74) Wilcox, D. E.; Sykes, M. E.; Niedringhaus, A.; Shtein, M.; Ogilvie, J. P. Heterodyne-Detected and Ultrafast Time-Resolved Second-Harmonic Generation for Sensitive Measurements of Charge Transfer. *Opt. Lett.* **2014**, *39* (14), 4274–4274.

(75) Tang, C. W. Two-Layer Organic Photovoltaic Cell. *Appl. Phys. Lett.* **1986**, *48*, 183–185.

(76) Stillman, M. J.; Nyokong, T. Absorption and Magnetic Circular Dichrosim Spectral Properties of Phthalocyanines Part 1: Complexes of the Dianion Pc(-2). In *Phthalocyanines: Properties and Applications*; VCH: New York, 1989; Vol. 1, pp 133–290.

(77) Ashida, M.; Uyeda, N.; Suito, E. Unit Cell Metastable-Form Constants of Various Phthalocyanines. *Bull. Chem. Soc. Jpn.* **1966**, *39* (12), 2616–2624.

(78) Hoshino, A.; Takenaka, Y.; Miyaji, H. Redetermination of the Crystal Structure of A-Copper Phthalocyanine Grown on KCl. *Acta Crystallogr.* **2003**, *B59*, 393–403.

(79) Cruickshank, A. C.; Dotzler, C. J.; Din, S.; Heutz, S.; Toney, M. F.; Ryan, M. P. The Crystalline Structure of Copper Phthalocyanine Films on ZnO(1$\bar{1}$00). *J. Am. Chem. Soc.* **2012**, *134* (35), 14302–14305.

(80) Sato, M.; Takeuchi, A.; Yamada, T.; Hoshi, H.; Ishikawa, K.; Mori, T.; Takezoe, H. Intermolecular Transitions Observed by Electric-Quadrupole-Resonant Second-Harmonic Generation in a Discotic Liquid Crystal of Phthalocyanine. *Phys. Rev. E* **1997**, *56* (6), R6264–R6266.

(81) Yamada, T.; Hoshi, H.; Manaka, T.; Ishikawa, K.; Takezoe, H.; Fukuda, A. Resonant Enhancement of Second-Harmonic Generation of Electric Quadrupole Origin in Phthalocyanine Films. *Phys. Rev. B* **1996**, *53* (20), R13314–R13317.

(82) Yamada, T.; Manaka, T.; Hoshi, H.; Ishikawa, K.; Takezoe, H. Optical Second Harmonic Generation Spectra in Vacuum-deposited Thin Films of Various Phthalocyanines. *J. Porphyr. Phthalocyanines* **1998**, *2* (2), 133–137.

(83) Hoshi, H.; Yamada, T.; Ishikawa, K.; Takezoe, H.; Fukuda, A. Second-Harmonic Generation in Centrosymmetric Molecular Films: Analysis under Anisotropic Conditions. *Phys. Rev. B* **1995**, *52* (16), 12355–12365.

(84) Chollet, P.-A.; Kajzar, F.; Moigne, J. L. Structure and Nonlinear Optical Properties of Copper Phthalocyanine Thin Films. *Mol. Eng.* **1991**, *1* (1), 35–47.

(85) Li, C. Q.; Manaka, T.; Cheng, X. M.; Iwamoto, M. Second Harmonic Generation from Copper-Tetratert-Butyl-Phthalocyanine Langmuir-Blodgett Film/Metal Interface: Electric Quadrupole or Electric Field Induced Second Harmonic Generation Effect? *J. Appl. Phys.* **2002**, *92* (11), 6390–6398.

(86) Sun, S.; Tian, C.; Shen, Y. R. Surface Sum-Frequency Vibrational Spectroscopy of Nonpolar Media. *Proc. Natl. Acad. Sci.* **2015**, *112* (19), 5883–5887.

(87) Guyot-Sionnest, P.; Shen, Y. R. Bulk Contribution in Surface Second-Harmonic Generation. *Phys. Rev. B* **1988**, *38* (12), 7985–7989.

(88) Mack, J.; Stillman, M. J. Band Deconvolution Analysis of the Absorption and Magnetic Circular Dichroism Spectral Data of ZnPc (-2) Recorded at Cryogenic Temperatures. *J. Phys. Chem.* **1995**, *99* (20), 7935–7945.

(89) Mack, J.; Stillman, M. J. Electronic Structures of Metal Phthalocyanine and Porphyrin Complexes from Analysis of the UV–Visible Absorption and Magnetic Circular Dichroism Spectra and Molecular Orbital Calculations. In *The Porphyrin Handbook: Volume 16, Phthalocyanines: Spectroscopic and Electrochemical Characterization*; Academic Press: Amsterdam, 2003; Vol. 16, pp 43–116.

(90) E. A. Lucia; Verderame, F. D. Spectra of Polycrystalline Phthalocyanines in the Visible Region. *J. Chem. Phys.* **1968**, *48* (6), 2674–2681.

(91) Schechtman, B. H.; Spicer, W. E. Near Infrared to Vacuum Ultraviolet Absorption Spectra and the Optical Constants of Phthalocyanine and Porphyrin Films. *J. Mol. Spectrosc.* **1970**, *33*, 28–48.

(92) Huang, T.-H.; Rieckhoff, K. E.; Voigt, E. M. New Singlets in the Phthalocyanines. *J. Phys. Chem.* **1981**, *85* (22), 3322–3326.

(93) Van Cott, T. C.; Rose, J. L.; Misener, G. C.; Williamson, B. E.; Schrimpf, A. E.; Boyle, M. E.; Schatz, P. N. Magnetic Circular Dichroism and Absorption Spectrum of Zinc Phthalocyanine in an Argon Matrix between 14700 and 74000 Cm-1. *J. Phys. Chem.* **1989**, *93* (8), 2999–3011.

(94) Nemykin, V. N.; Hadt, R. G.; Belosludov, R. V.; Mizuseki, H.; Kawazoe, Y. Influence of Molecular Geometry, Exchange-Correlation Functional, and Solvent Effects in the Modeling of Vertical Excitation Energies in Phthalocyanines Using Time-Dependent Density Functional Theory (TDDFT) and Polarized Continuum Model TDDFT Methods: Can Modern Computational Chemistry Methods Explain Experimental Controversies? *J. Phys. Chem. A* **2007**, *111* (50), 12901–12913.

(95) Tokura, Y.; Koda, T.; Iyechika, Y.; Kuroda, H. Electro-Reflectance Spectra of Charge-Transfer Excitations in Copper Phthalocyanine Single Crystals. *Chem. Phys. Lett.* **1983**, *102* (2), 174–178.

(96) Yoshida, H.; Tokura, Y.; Koda, T. Charge-Transfer Excitation Bands in Electro-Absorption Spectra of Metal (Co, Ni, Cu, Zn)-Phthalocyanine Films. *Chem. Phys.* **1986**, *109* (2–3), 375–382.

(97) Kirichenko, N. A.; Blinov, L. M. Charge-Transfer States and Optical Spectra in the Condensed Phase. *Zhurnal Prikl. Spektrosk.* **1978**, *28* (6), 1057–1061.

(98) Knupfer, M.; Schwieger, T.; Peisert, H.; Fink, J. Mixing of Frenkel and Charge Transfer Excitons in Quasi-One-Dimensional Copper Phthalocyanine Molecular Crystals. *Phys. Rev. B* **2004**, *69* (16), 165210.

(99) Resel, R.; Ottmar, M.; Hanack, M.; Keckes, J.; Leising, G. Preferred Orientation of Copper Phthalocyanine Thin Films Evaporated on Amorphous Substrates. *J. Mater. Res.* **2000**, *15* (04), 934–939.

(100) Cheng, C. H.; Wang, J.; Du, G. T.; Shi, S. H.; Du, Z. J.; Fan, Z. Q.; Bian, J. M.; Wang, M. S. Organic Solar Cells with Remarkable Enhanced Efficiency by Using a CuI Buffer to Control the Molecular Orientation and Modify the Anode. *Appl. Phys. Lett.* **2010**, *97* (8), 083305.

(101) Peisert, H.; Schwieger, T.; Auerhammer, J. M.; Knupfer, M.; Golden, M. S.; Fink, J.; Bressler, P. R.; Mast, M. Order on Disorder: Copper Phthalocyanine Thin Films on Technical Substrates. *J. Appl. Phys.* **2001**, *90* (1), 466–469.

(102) Berger, O.; Fischer, W.-J.; Adolphi, B.; Tierbach, S.; Melev, V.; Schreiber, J. Studies on Phase Transformations of Cu-Phthalocyanine Thin Films. *J. Mater. Sci. Mater. Electron.* **2000**, *11* (4), 331–346.

(103) Brown, C. J. Crystal Structure of β-Copper Phthalocyanine. *J. Chem. Soc. Inorg. Phys. Theor.* **1968**, 2488–2493.

(104) Rand, B. P.; Cheyns, D.; Vasseur, K.; Giebink, N. C.; Mothy, S.; Yi, Y.; Coropceanu, V.; Beljonne, D.; Cornil, J.; Brédas, J.-L.; et al. The Impact of Molecular Orientation on the Photovoltaic Properties of a Phthalocyanine/Fullerene Heterojunction. *Adv. Funct. Mater.* **2012**, *22* (14), 2987–2995.

(105) Kobayashi, T.; Fujiyoshi, Y.; Uyeda, N. The Observation of Molecular Orientations in Crystal Defects and the Growth Mechanism of Thin Phthalocyanine Films. *Acta Crystallogr.* **1982**, *A38*, 356–362.

(106) Yost, S. R.; Voorhis, T. V. Electrostatic Effects at Organic Semiconductor Interfaces: A Mechanism for "Cold" Exciton Breakup. *J. Phys. Chem. C* **2013**, *117* (11), 5617–5625.

(107) Kumagai, K.; Mizutani, G.; Tsukioka, H.; Yamauchi, T.; Ushioda, S. Second-Harmonic Generation in Thin Films of Copper Phthalocyanine. *Phys. Rev. B* **1993**, *48* (19), 14488–14495.

(108) Richmond, G. L. Molecular Bonding and Interactions at Aqueous Surfaces as Probed by Vibrational Sum Frequency Spectroscopy. *Chem. Rev.* **2002**, *102* (8), 2693–2724.

(109) Lin, C.-K.; Hayashi, M.; Lin, S. H. Theoretical Formulation and Simulation of Electronic Sum-Frequency Generation Spectroscopy. *J. Phys. Chem. C* **2013**, *117* (45), 23797–23805.

(110) Ramprasad, R.; Shi, N. Polarizability of Phthalocyanine Based Molecular Systems: A First-Principles Electronic Structure Study. *Appl. Phys. Lett.* **2006**, *88* (22), 222903.

(111) Stiopkin, I. V.; Jayathilake, H. D.; Bordenyuk, A. N.; Benderskii, A. V. Heterodyne-Detected Vibrational Sum Frequency Generation Spectroscopy. *J. Am. Chem. Soc.* **2008**, *130*, 2271–2275.

(112) Lucarini, V.; Saarinen, J. J.; Peiponen, K.-E.; Vartiainen, E. *Kramers-Kronig Relations in Optical Materials Research*; Optical Sciences; Springer: Berlin, 2005.

(113) Djurisic, A. B.; Kwong, C. Y.; Lau, T. W.; Guo, W. L.; Li, E. H.; Liu, Z. T.; Kwok, H. S.; Lam, L. S. M.; Chan, W. K. Optical Properties of Copper Phthalocyanine. *Opt. Commun.* **2002**, *205*, 155–162.

(114) Barrett, M. A.; Borkowska, Z.; Humphreys, M. W.; Parsons, R. Ellipsometry of Thin Films of Copper Phthalocyanine. *Thin Solid Films* **1975**, *28* (2), 289–302.

(115) Guyot-Sionnest, P.; Shen, Y. R. Local and Nonlocal Surface Nonlinearities for Surface Optical Second-Harmonic Generation. *Phys. Rev. B* **1987**, *35* (9), 4420.

(116) Dutton, G. J.; Robey, S. W. Exciton Dynamics at CuPc/C 60 Interfaces: Energy Dependence of Exciton Dissociation. *J. Phys. Chem. C* **2012**, *116* (36), 19173–19181.

(117) Lewis, N. S. Research Opportunities to Advance Solar Energy Utilization. *Science* **2016**, *351* (6271), aad1920–aad1920.

(118) Rao, A.; Friend, R. H. Harnessing Singlet Exciton Fission to Break the Shockley–Queisser Limit. *Nat. Rev. Mater.* **2017**, *2*, 17063.

(119) Berkelbach, T. C.; Hybertsen, M. S.; Reichman, D. R. Microscopic Theory of Singlet Exciton Fission. I. General Formulation. *J. Chem. Phys.* **2013**, *138* (11), 114102.

(120) Casanova, D. Theoretical Modeling of Singlet Fission. *Chem. Rev.* **2018**, *118* (15), 7164–7207.

(121) Farag, M. H.; Krylov, A. I. Singlet Fission in Perylenediimide Dimers. *J. Phys. Chem. C* **2018**, *122* (45), 25753–25763. .

(122) Smith, M. B.; Michl, J. Singlet Fission. *Chem. Rev.* **2010**, *110* (11), 6891–6936.

(123) Gish, M. K.; Pace, N. A.; Rumbles, G.; Johnson, J. C. Emerging Design Principles for Enhanced Solar Energy Utilization with Singlet Fission. *J. Phys. Chem. C* **2019**.

(124) Dexter, D. L. Two Ideas on Energy Transfer Phenomena: Ion-Pair Effects Involving the OH Stretching Mode, and Sensitization of Photovoltaic Cells. *J. Lumin.* **1979**, *18–19*, 779–784.

(125) Piland, G. B.; Burdett, J. J.; Hung, T.-Y.; Chen, P.-H.; Lin, C.-F.; Chiu, T.-L.; Lee, J.-H.; Bardeen, C. J. Dynamics of Molecular Excitons near a Semiconductor Surface Studied by Fluorescence Quenching of Polycrystalline Tetracene on Silicon. *Chem. Phys. Lett.* **2014**, *601*, 33–38.

(126) Pazos-Outón, L. M.; Lee, J. M.; Futscher, M. H.; Kirch, A.; Tabachnyk, M.; Friend, R. H.; Ehrler, B. A Silicon–Singlet Fission Tandem Solar Cell Exceeding 100% External Quantum Efficiency with High Spectral Stability. *ACS Energy Lett.* **2017**, *2* (2), 476–480.

(127) Le, A. K.; Bender, J. A.; Arias, D. H.; Cotton, D. E.; Johnson, J. C.; Roberts, S. T. Singlet Fission Involves an Interplay between Energetic Driving Force and Electronic Coupling in Perylenediimide Films. *J. Am. Chem. Soc.* **2018**, *140* (2), 814–826.

(128) Ryno, S. M.; Fu, Y.-T.; Risko, C.; Brédas, J.-L. Polarization Energies at Organic–Organic Interfaces: Impact on the Charge Separation Barrier at Donor–Acceptor Interfaces in Organic Solar Cells. *ACS Appl. Mater. Interfaces* **2016**, *8* (24), 15524–15534.

(129) Ryno, S. M.; Risko, C.; Brédas, J.-L. Impact of Molecular Orientation and Packing Density on Electronic Polarization in the Bulk and at Surfaces of Organic Semiconductors. *ACS Appl. Mater. Interfaces* **2016**, *8* (22), 14053–14062.

(130) Vasseur, K.; Rolin, C.; Vandezande, S.; Temst, K.; Froyen, L.; Heremans, P. A Growth and Morphology Study of Organic Vapor Phase Deposited Perylene Diimide Thin Films for Transistor Applications. *J. Phys. Chem. C* **2010**, *114* (6), 2730–2737.

(131) Takahashi, Y.; Mikasa, T.; Hayakawa, K.; Yokokura, S.; Hasegawa, H.; Harada, J.; Inabe, T. Fabrication of Conducting Thin Films on the Surfaces of 7,7,8,8-

Tetracyanoquinodimethane Single-Component and Charge-Transfer Complex Single Crystals: Nucleation, Crystal Growth, Morphology, and Charge Transport. *J. Phys. Chem. C* **2016**, *120* (31), 17537–17545.

(132) Griffin, M. P.; Gearba, R.; Stevenson, K. J.; Vanden Bout, D. A.; Dolocan, A. Revealing the Chemistry and Morphology of Buried Donor/Acceptor Interfaces in Organic Photovoltaics. *J. Phys. Chem. Lett.* **2017**, 2764–2773.

(133) Lin, C.-K.; Lei, J.; Lin, Y.-D.; Lin, S. H. Electronic Sum-Frequency Generation (ESFG) Spectroscopy: Theoretical Formulation of Resonances with Symmetry-Allowed and Symmetry-Forbidden Electronic Excited States. *Mol. Phys.* **2017**, 1–10.

(134) Le, A. K.; Bender, J. A.; Roberts, S. T. Slow Singlet Fission Observed in a Polycrystalline Perylenediimide Thin Film. *J. Phys. Chem. Lett.* **2016**, *7* (23), 4922–4928.

(135) Eaton, S. W.; Shoer, L. E.; Karlen, S. D.; Dyar, S. M.; Margulies, E. A.; Veldkamp, B. S.; Ramanan, C.; Hartzler, D. A.; Savikhin, S.; Marks, T. J.; et al. Singlet Exciton Fission in Polycrystalline Thin Films of a Slip-Stacked Perylenediimide. *J. Am. Chem. Soc.* **2013**, *135* (39), 14701–14712.

(136) Kazmaier, P. M.; Hoffmann, R. A Theoretical Study of Crystallochromy. Quantum Interference Effects in the Spectra of Perylene Pigments. *J. Am. Chem. Soc.* **1994**, *116* (21), 9684–9691.

(137) Hädicke, E.; Graser, F. Structures of Eleven Perylene-3,4:9,10-Bis(Dicarboximide) Pigments. *Acta Crystallogr. C* **1986**, *42* (2), 189–195.

(138) Kemnitz, K.; Bhattacharyya, K.; Hicks, J. M.; Pinto, G. R.; Eisenthal, K. B.; Heinz, T. F. The Phase of Second-Harmonic Light Generated at an Interface and Its Relation to Absolute Molecular Orientation. *Chem. Phys. Lett.* **1985**, *131* (4,5), 285–290.

(139) Nelson, C. A.; Luo, J.; Laghumavarapu, R. B.; Huffaker, D. L.; Zhu, X.-Y. Time-, Energy-, and Phase-Resolved Second-Harmonic Generation at Semiconductor Interfaces. *J. Phys. Chem. C* **2014**, *118* (48), 27981–27988.

(140) Park, H.; Gutierrez, M.; Wu, X.; Kim, W.; Zhu, X. Y. Optical Probe of Charge Separation at Organic/Inorganic Semiconductor Interfaces. *J. Phys. Chem. C* **2013**, *117*, 10974–10979.

(141) Inoue, K.; Nihonyanagi, S.; Singh, P. C.; Yamaguchi, S.; Tahara, T. 2D Heterodyne-Detected Sum Frequency Generation Study on the Ultrafast Vibrational Dynamics of H2O and HOD Water at Charged Interfaces. *J. Chem. Phys.* **2015**, *142* (21), 212431–212431.

(142) Wilson, P. T.; Jiang, Y.; Aktsipetrov, O. A.; Mishina, E. D.; Downer, M. C. Frequency-Domain Interferometric Second-Harmonic Spectroscopy. *Opt. Lett. 24* (7), 496–498.

(143) Pool, R. E.; Versluis, J.; Backus, E. H. G.; Bonn, M. Comparative Study of Direct and Phase-Specific Vibrational Sum-Frequency Generation Spectroscopy: Advantages and Limitations. *J. Phys. Chem. B* **2011**, *115* (51), 15362–15369.

(144) Ostroverkhov, V.; Waychunas, G. A.; Shen, Y. R. New Information on Water Interfacial Structure Revelaed by Phase-Sensitive Surface Spectroscopy. *Phys. Rev. Lett.* **2005**, *94* (9), 046102:1-4.

(145) Chang, R. K.; Ducuing, J.; Bloembergen, N. Relative Phase Measurement between Fundamental and Second-Harmonic Spectroscopy. *Phys Rev Lett* **1965**, *15*, 6.

(146) Veenstra, K. J.; Petukhov, A. V.; De Boer, A. P.; Rasing, T. Phase-Sensitive Detection Technique for Surface Nonlinear Optics. *Phys Rev B* **1998**, *58*, R16020.

(147) Renaud, N.; Sherratt, P. A.; Ratner, M. A. Mapping the Relation between Stacking Geometries and Singlet Fission Yield in a Class of Organic Crystals. *J. Phys. Chem. Lett.* **2013**, *4* (7), 1065–1069.

(148) Renaud, N.; Ferdinand C. Grozema. Intermolecular Vibration Modes Speed Up Singlet Fission in Perylenediimide Crystals. *J. Phys. Chem. Lett.* **2015**.

(149) Foglia, L.; Wolf, M.; Stahler, J. Ultrafast Dynamics in Solids Probed by Femtosecond Time-Resolved Broadband Elkectronic Sum Frequency Generation. *Appl. Phys. Lett.* **2016**, *109*, 202106.

(150) Wilcox, D. E.; Lee, M. H.; Sykes, M. E.; Niedringhaus, A.; Geva, E.; Dunietz, B. D.; Shtein, M.; Ogilvie, J. P. Ultrafast Charge-Transfer Dynamics at the Boron Subphthalocyanine Chloride/C60 Heterojunction: Comparison between Experiment and Theory. *J. Phys. Chem. Lett.* **2015**, *6* (3), 569–575.

(151) Xiong, W.; Laaser, J. E.; Mehlenbacher, R. D.; Zanni, M. T. Adding a Dimension to the Infrared Spectra of Interfaces Using Heterodyne Detected 2D Sum-Frequency Generation ( HD 2D SFG ) Spectroscopy. *Proc. Natl. Acad. Sci.* **2011**, *108* (52), 20902–20907.

(152) Zhang, Z.; Piatkowski, L.; Bakker, H. J.; Bonn, M. Ultrafast Vibratinal Energy Transfer at the Water / Air Interface Revealed by Two-Dimensional. *Nat. Chem.* **2011**, *3* (11), 888–893.

(153) Kundu, A.; Yamaguchi, S.; Tahara, T. Evaluation of PH at Charged Lipid/Water Interfaces by Heterodyne-Detected Electronic Sum Frequency Generation. *J Phys Chem Lett* **2014**, *5*, 762.

(154) Brixner, T.; Mancal, T.; Stiopkin, I. V.; Fleming, G. R. Phase-Stabilized Two-Dimensional Electronic Spectroscopy. *J Chem Phys* **2004**, *121*, 4221–4236.

(155) Rivera, C. A.; Bradforth, S. E.; Tempea, G. Gires-Tournois Interferometer Type Negative Dispersion MIrrors for Deep Ultraviolet Pulse Compression. *Opt Express* **2010**, *18*, 18615.

(156) Dadap, J. I.; Shan, J.; Weling, A. S.; Heinz, T. F. Homodyne Detection of Second-Harmonic Generation as a Probe of Electric Fields. *Appl Phys B* **1999**, *68*, 333.

(157) Schott AG. Optical Glass Data Sheets. 2015.

(158) Zhuang, X.; Miranda, P.; Kim, D.; Shen, Y. Mapping Molecular Orientation and Conformation at Interfaces by Surface Nonlinear Optics. *Phys. Rev. B* **1999**, *59* (19), 12632–12640.

(159) Wang, H.-F.; Gan, W.; Lu, R.; Rao, Y.; Wu, B.-H. Quantitative Spectral and Orientational Analysis in Surface Sum Frequency Generation Vibrational Spectroscopy (SFG-VS). *Int Rev Phys Chem* **2005**, *24*, 191.